eXPRESS Polymer Letters Vol.2, No.7 (2008) 460
Available online at www.expresspolymlett.com
DOI: 10.3144/expresspolymlett.2008.55

Editorial corner – a personal view

Nanodielectrics: an emerging sector of polymer nanocomposites

G. C. Psarras[*]

Department of Materials Science, University of Patras, Patras 26504, Hellas (Greece)

In our days the scientific and technological importance of nanostructured materials is worldwide understood and recognized, giving rise to expectations for materials with superior or unique performance and properties. The term nanodielectrics is rather new and refers to dielectric materials, which comprise entities with dimensions (at least one) at the nanometric scale. Two are the basic categories of nanodielectrics: (a) polycrystalline semiconducting or insulating materials, with grain diameter at the nanoscale level and (b) polymer composites incorporating nanoinclusions. The second category displays a number of advantages, e.g. easy processing and thermo-mechanical stability. Moreover the dielectric behaviour can be tailored by simply controlling the type and the amount of the nanofiller. Under this point of view, polymer matrix nanocomposites are expected to replace conventional insulating materials in a variety of applications.

Capacitance the fundamental quantity in dielectrics, in contrary with other physical quantities, is increasing as the dimension of width in nanoinclusions is decreasing. This fact gives the possibility to exploit nanoinclusions as an inherent system of nanocapacitors. The charging and discharging of nanocapacitors defines an energy storing process, at the nanoscale level, introducing a new type of nanodevices. Nanofillers are frequently used as structural elements in nanocomposite systems. In some cases, the same elements could be able to act as nanocapacitors or ‘structural batteries’. Furthermore, the presence of ‘active dielectrics’ (i.e. piezo/ferroelectric or polar oxides nanoparticles) within the polymer matrix could provide functionality to the nanocomposite, through the conditionally variable electrical polarization. Combining mechanical and electrical reinforcement with energy storing procedure and functionality leads to a significant approach to the concept of ‘smart materials’, where structural elements should also play the roles of sensing, actuating and energy storing subsystems.

Finally, the importance of studying conduction mechanisms in polymer matrix – conductive nanoinclusions composites should be noted. The insulator to conductor transition is expected to occur at a low content of the conductive phase, while the temperature and field dependence of conductivity can be exploited for the development of self-current regulators, self-heating systems, memory switches and other applications.

Definitely a lot should be expected from this field in the near future.

Prof. Dr. Georgios C. Psarras
Member of International Advisory Board

---

[*] Corresponding author, e-mail: G.C.Psarras@upatras.gr

eXPRESS Polymer Letters Vol.2, No.7 (2008) 461–473
Available online at www.expresspolymlett.com
DOI: 10.3144/expresspolymlett.2008.56

Multiple shape-memory behavior and thermal-mechanical properties of peroxide cross-linked blends of linear and short-chain branched polyethylenes

I. S. Kolesov, H.-J. Radusch*

Martin Luther University Halle-Wittenberg, Center of Engineering Sciences, Chair Polymer Technology, D-06099 Halle (Saale), Germany

Received 12 March 2008; accepted in revised form 29 April 2008

Abstract. Thermally induced shape-memory effect (SME) in tensile mode was investigated in binary and ternary blends of two ethylene-1-octene copolymers with a degree of branching of 30 and 60 CH_3/1000C and/or nearly linear polyethylene cross-linked after melt mixing with 2 wt% of liquid peroxide 2,5-dimethyl-2,5-di-(tert.butylperoxy)-hexane at 190°C. The average cross-link density estimated by means of the *Mooney-Rivlin* equation on the basis of tensile test data was characterized between 130 and 170 $mol \cdot m^{-3}$ depending on the blend composition. Thermal analysis points out *multiple* crystallization and melting behavior of blends caused by the existence of several polyethylene crystal populations with different perfection, size and correspondingly different melting temperature of crystallites. That agrees well with the diversity of blends phase morphology characterized by atomic force microscopy. However, *triple*- and *quadruple*-SME could be observed only after two- and accordingly three-step programming of binary and tertiary blends, respectively, at suitable temperatures and strains. Compared to performances obtained for the same blend after single-step programming above the maximal melting temperature the significantly poorer characteristics of SME like strain fixity and strain recovery ratio as well as recovery strain rate occurred after multi-step programming.

Keywords: *smart polymers, shape-memory effect, polymer blends, polyolefins*

1. Introduction

Shape-memory (SM) polymers represent a specific class of smart polymers which can be advantageously used in several fields of application, e.g. cable and packaging industry [1, 2], medicine and automotive [3–6]. Preconditions for proper appearance of the thermally induced SM effect are the existence of a stable physical or covalent molecular network and glass or phase transition (melting), respectively, at convenient temperatures T_{trans} [4–6]. For covalent (e.g. peroxidic) cross-linked semicrystalline polymers a SM behavior with high performance can be achieved, if *firstly* the polymeric material shows sufficiently high strain at break as well as preferably lowest residual strain after unloading, and produces sufficiently high visco-elastic forces under load at programming temperature $T_{pr} > T_{trans}$. *Secondly*, its crystalline phase formed during cooling of the programmed (*loaded*) sample is able to fix efficiently the strain and visco-elastic forces stored in the network. The SM behavior is characterized by the response temperature, strain fixity and strain recovery ratios. The response temperature (T_{res}) corresponds to maximum of recovery strain rate $-d\varepsilon_r/dt$ in a linear heating run of a programmed and at low temperature (e.g. room temperature) unloaded specimen.

---

*Corresponding author, e-mail: igor.kolesov@iw.uni-halle.de

Strain fixity (R_f) and strain recovery ratios (R_r) are defined according to [4] by Equations (1):

$$R_f = \frac{\varepsilon_v}{\varepsilon_p}, \qquad R_r = \frac{\varepsilon_p - \varepsilon_{rec,m}}{\varepsilon_p} \tag{1}$$

where ε_p is the strain caused by programming, ε_v is the strain that remains after programming, cooling and unloading of specimen and $\varepsilon_{rec,m}$ is the residual strain that resides after thermal induced recovery (shrinkage) at maximum temperature of experiment.

The investigation of the SM effect of covalent cross-linked semicrystalline polymers and in particular of peroxidic cross-linked ethylene copolymers [7–10] showed a strong correlation between the melting temperature $T_m \equiv T_{trans}$ of the crystalline phase and the response temperature T_{res}, namely $T_{res} \approx T_m$. Thus, it may be assumed that the existence of several '*n*' crystalline phases or/and crystal populations with different perfection, size and correspondingly with distinctly different melting temperatures $T_{m.i}$ in one polymeric material results presumably in a *multiple* SM behavior, i.e. in the appearance of the same or lower number of recovery strain $\varepsilon_{rec}(T)$ steps and accordingly $d\varepsilon_{rec}(T)/dt$ maxima with response temperatures $T_{res.i} \approx T_{m.i}$ where $1 \le i \le n$ (*i* is an even number).

The *triple*-shape memory behavior for two different complex polymer network systems which were prepared by photoinduced copolymerization of a methacrylate-monomer and poly(ε-caprolactone) dimethacrylate was already recently described by Bellin *et al.* [11]. These polymer network systems are formed from two types of chain sections/domains of different chemical constitution which connect network nodes and exhibit either melting process for both section/domain types or melting and glass transition, respectively, at two different temperatures. However, *triple*-shape memory effect appears only after programming in two-step process, i.e., at two temperatures agreeing with temperatures of melting or glass transition, whereas the suitable programming strains must be adjusted [11, 12]. Such polymeric materials with *multiple* SM behavior (*m*SMP) could certainly offer new interesting applications for SM polymers, e.g. intelligent fasteners, removable stents [11, 12], etc.

As is known (see e.g. [13]) the crystallinity, melting and crystallization temperature of polyethylenes and in particular of short-chain branched polyethylenes, e.g. ethylene-1-octene copolymers (EOC) decreases with increasing degree of branching. By means of blending of nearly linear high density polyethylene (HDPE) and EOCs with different 1-octene content and consequently different degree of branching the materials containing several crystalline phases with different $T_{m.i}$ and $T_{res.i}$ can be created. The multiple crystal populations can be created in polymer owing to multistep crystallization as it was shown by Varga *et al.* [14] for long-chain branched low-density polyethylene. The significant difference between the systems presented in this work and the network systems described by Bellin *et al.* [11, 12] are *firstly* the relatively chemical homogeneity of the links between network nodes which are predominantly ethylene sequences by reason that tertiary carbon atoms connected with branches are extra susceptible by peroxidic cross-linking [15] and *secondly* the low costs of polyethylenes and their processing. For above mentioned reasons, the objectives of the presented work were the production of peroxidic cross-linked binary and ternary blends on the basis of HDPE and two EOCs with medium and high degree of branching as well as the investigation on their SM behavior and their characterization by the relevant thermal and mechanical properties.

2. Experimental

2.1 Materials and processing

The polyethylenes used in this study are commercially available products (Dow Chemical, Schkopau, Germany), namely HDPE (KS 10100 UE) and metallocene-catalyzed homogeneous EOCs (AFFINITY™ PL 1280G and ENGAGE 8200) with approx. 30 and 60 hexyl branches per 1000 C (EOC30 and EOC60), respectively. In Table 1 few relevant parameters of these materials are given.

As cross-linking agent 2,5-dimethyl-2,5-di-(tert.butylperoxy)-hexane (DHBP) (Degussa Initiators GmbH & Co KG, Pullach, Germany) was employed. The use of DHBP resulted in a high efficiency and a good processability of the chosen systems due to the availability of two peroxy groups and the high thermal stability (up to 145°C) of DHBP as well as its fluidity at room temperature. The DHBP shows a better processability by cross-linking of EOCs compared to dicumyl peroxide

Table 1. Designations as well as some physical and molecular parameters of the used polyethylenes

Designation	Melt index (MI)* [dg/min]			Tm [°C]	Density [kg/m³]	Mass-average molecular mass $\overline{M}_w$ [kg/mol]	Polydispersity $\overline{M}_w/\overline{M}_n$	Degree of branching [CH_3 /1000C]
	190°C/ 2.16 kg	190°C/ 5.0 kg	130°C/ 5.0 kg					
HDPE	3.0	10.1	2.5	132	955	–	–	–
EOC30	5.0	17.7	4.2	96	900	64	2.3	~30
EOC60	4.4	15.9	3.4	59	870	87	2.5	~60

*detected by means of melt index test apparatus MI 21,6 (Göttfert Werkstoff-Prüfmaschinen GmbH, Buchen, Germany)

which entails gas release by cross-linking [9, 10]. Before blending the polymers were impregnated with DHBP. For these purposes the pellets of polymer were wetted with 2 wt% of DHBP and the fluid cross-linking agent was allowed to diffuse into these pellets placed in hermetic plastic flask for 3 days.

The mechanical mix of with DHBP impregnated polymer pellets in desired ratio (see Table 2) was then blended using a single-screw extruder (Brabender® GmbH & Co. KG, Duisburg, Germany) with the barrel temperature of 130°C whereby the distribution of DHBP was homogenized. As reference object a cross-linked HDPE was prepared and investigated in the same manner. It seems that homogenization of the peroxide in the melt-mixing process is essential for subsequent cross-linking. The processing experiments show that the applied cross-linking method is suitable for polyethylenes with the chosen melt index MI (see Table 1). At the same time, it should be noted that DHBP as a low-molecular substance can act as a lubricant at the processing temperature of 130°C in the extruder. Therefore the effective MI values of the DHBP impregnated polyethylenes are evidently higher and the viscosities are lower than that of pure materials. This effect supports the mixing process at 130°C. At higher temperatures immediately after the onset of the cross-linking process, the viscosity increases and the MI decreases dramatically with increasing temperature and duration of mixing. The extrudate was further processed to films with a thickness of 1 and 2 mm at 140°C and immediately cross-linked at a temperature of 190°C. The cross-linking time and temperature were optimized using a vulcameter Elastograph (Göttfert Werkstoff-Prüfmaschinen GmbH, Buchen, Germany).

2.2. Instrumentation

The *tensile tests* in the temperature range of SM tests programming (120 and 140°C) has been carried out using a testing machine Zwick 1425 (Zwick GmbH & Co. KG, Ulm, Germany) with heating chamber and a load cell 10 N at a crosshead speed of 50 mm/min after DIN EN ISO 527-1 (1996) standard. As specimens shouldered test bars were used with the cross-section area 2.0×2.0 mm² (test bar 5B according to DIN EN ISO 3167). The initial clamps distance was 20 mm.

Thermal analysis was performed with a heat-flux differential scanning calorimeter DSC 820 (Mettler-Toledo GmbH, Giessen, Germany) equipped with a ceramic sensor FRS5 and a liquid nitrogen cooling accessory. The heating and cooling scans were performed with 20 and 10 K/min, respectively.

Morphological investigations were carried out by an atomic force microscope Q-Scope 250 (Quesant

Table 2. Designations and composition of the extruded binary and ternary blends of polyethylenes used

Designation	Content of		
	HDPE [%]	EOC30 [%]	EOC60 [%]
100**HDPE**	100	–	–
50**HDPE**/50**EOC**30	50	50	–
33**HDPE**/33**EOC**30/34**EOC**60	33	33	34
10H**DPE**/45**EOC**30/45**EOC**60	10	45	45
10H**DPE**/25**EOC**30/65**EOC**60	10	25	65
50**EOC**30/50**EOC**60	–	50	50
30**EOC**30/70**EOC**60	–	30	70

Instrument Corporation, California, USA) operated in intermittent mode. Cantilever used are NSC 16 with resonance frequency f_R of 190 kHz and spring constant F of 48 N·m^{-1} (Nano and More GmbH, Wetzlar, Germany). Samples were produced by cutting in a cryo-chamber CN 30 (Microm-International-GmbH, Walldorf, Germany) with a diamond knife at –90°C.

For the characterization of the *shape memory behavior* the samples came at first under a specific temperature-deformation program. The samples were programmed by a stretching strain of $\varepsilon_{p1} \leq 100\%$ during a dwell period of 120 s at the programming temperature T_{p1}, and cooled down to T_{p2} with an average cooling rate of approx. 11 K/min in a constant deformed state. Before loading of the next programming strain ε_{pi} the sample temperature was kept constant for 10 min. After last programming step the specimen was cooled down to 10°C at the summary programming strain of 100%, thermal equilibrated for 10 min and unloaded. The recovery strain was measured first after a delay of 10 min at 25°C (ε_v) and than in the course of a heating run with a rate of 2 K/min and 'zero' stress of 70 Pa ($\varepsilon_{rec}(T)$). Complete SM investigations were carried out in tensile mode using a mechanical spectrometer measuring head Mark III (Rheometric Scientific Inc., New Jersey, USA).

3. Results and discussion

3.1. Uniaxial tension measurements. Cross-linking properties

The stress-strain diagrams of the investigated materials and their evaluation are depicted in Figure 1. The *Mooney-Rivlin* equation (2) for uniaxial tension (see [16, 17] and their references) was used for fitting the experimental results:

$$\sigma_{el} = 2C_1\left(\lambda - \frac{1}{\lambda^2}\right) + \frac{2C_2}{\lambda}\left(\lambda - \frac{1}{\lambda^2}\right) \qquad (2)$$

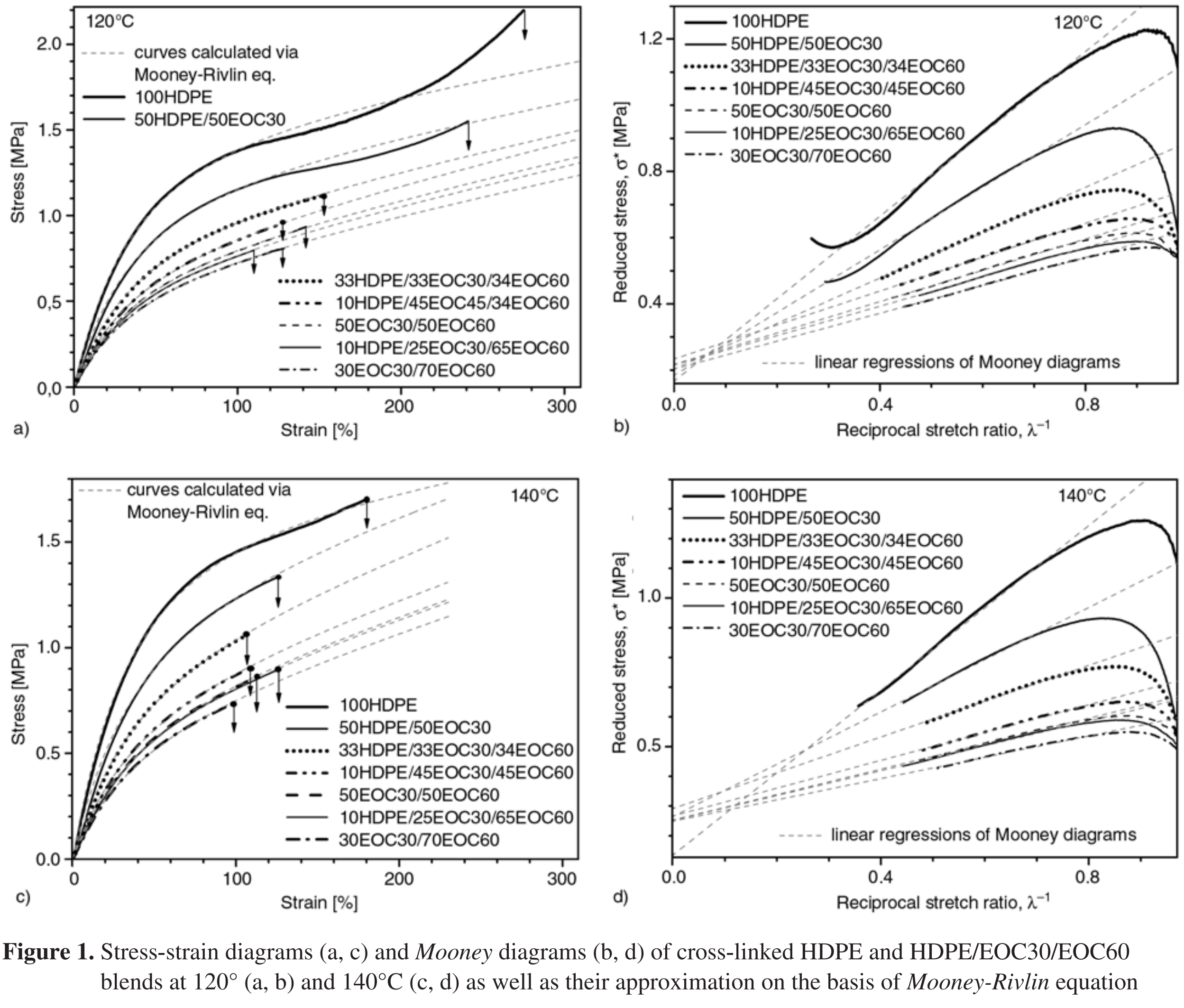

Figure 1. Stress-strain diagrams (a, c) and *Mooney* diagrams (b, d) of cross-linked HDPE and HDPE/EOC30/EOC60 blends at 120° (a, b) and 140°C (c, d) as well as their approximation on the basis of *Mooney-Rivlin* equation

where $2C_1$ is connected with shear *modulus G* and tensile *modulus E* as follows $2C_1 \equiv G = E/3$. The term $2C_1$ is responsible for the description of the influence of covalent network, the coefficient $2C_2$ takes into account entanglements, distribution of chain length, short-range order states and free chain tails.

Converting the *Mooney-Rivlin* equation (Equation (2)) a linear relationship between reduced stress $\sigma^* = \sigma_{el}/(\lambda - \lambda^{-2})$ and reciprocal stretch ratio λ^{-1} (Equation (3)) will be obtained:

$$\sigma^* = 2C_1 + \frac{2C_2}{\lambda} \tag{3}$$

In this connection the coefficients $2C_1$ and $2C_2$ of the *Mooney-Rivlin* equation were determined by means of linear regression of the corresponding legs of the *Mooney* diagram $\sigma^* = f(\lambda^{-1})$ as it is demonstrated in Figures 1b and 1d. The stress-strain diagrams which were generated on the basis of the obtained $2C_1$ and $2C_2$ coefficients agree quite well with the experimental results obtained for HDPE and HDPE/EOC30/EOC60 blends in the strain range till approx. 160% (see Figures 1a and 1c). However, HDPE and 50HDPE/50EOC30 blend at 120°C are exceptions in consequence of the still existing crystallites of HDPE.

According to the rubber elasticity theory [18] for a covalent network with a functionality of network nodes $f = 4$. Equation (4) follows for the *modulus E*:

$$E = \frac{3}{2}\nu_c \cdot R \cdot T = \frac{3\rho \cdot R \cdot T}{2\overline{M}_c} \tag{4}$$

where ν_c is the cross-link density, $R = 8.31\ \mathrm{kJ\cdot(mol\cdot K)^{-1}}$ is the gas constant, T is the absolute temperature, $\overline{M}_c$ is the average molar mass of the polymer chains between two neighboring network nodes and ρ is the density of polyethylene which amounts to 806 and 795 $\mathrm{kg\cdot m^{-3}}$ [15, 19] at 120 and 140°C, respectively.

Thus, on the basis of Equations (2–4) the cross-link density and average molar mass of the polymer chains between two neighboring network nodes can be calculated by Equations (5):

$$\nu_c = \frac{2\cdot(2C_1)}{RT} \quad \text{and} \quad \overline{M}_c = \frac{\rho}{\nu_c} \tag{5}$$

The fitted values of the *Mooney-Rivlin* equation coefficients C_1 and C_2 as well as the calculated values of ν_c and $\overline{M}_c$ in combination with the experimentally determined values of strain at break ε_B and stress at break σ_B and stress at strain of 100% $\sigma_{100\%}$ of cross-linked HDPE and HDPE/EOC30/EOC60 blends are given in Table 3.

All investigated materials with the exception of HDPE (see Table 3) evidence a certain small increase of ν_c and consequently decrease of $\overline{M}_c$ values at higher temperature. The different behavior of HDPE is caused evidently by the above mentioned incomplete fusing of the crystalline HDPE

Table 3. Network parameters ν_c and $\overline{M}_c$ estimated from stress-strain diagrams on the basis of *Mooney-Rivlin* equation coefficients C_1 and C_2 as well as break strain ε_B and stress σ_B and stress at strain of 100% $\sigma_{100\%}$ of cross-linked HDPE and HDPE/EOC30/EOC60 blends

Blend composition	**$2C_1$ [MPa]**	**$2C_2$ [MPa]**	**T [°C]**	**ν_c [mol/m³]**	**$\overline{M}_W$ [kg/mol]**	**ε_B [%]**	**σ_B [MPa]**	**$\sigma_{100\%}$ [MPa]**
100**HDPE**	0.168	1.244	120	103	7.860	275	2.20	1.38
	0.135	1.386	140	79	10.093	180	1.70	1.45
50**HDPE**/50**EOC**30	0.185	0.946	120	114	7.077	241	1.55	1.15
	0.266	0.879	140	155	5.140	126	1.33	1.23
33**HDPE**/33**EOC**30/34**EOC**60	0.204	0.685	120	125	6.456	125	1.12	0.96
	0.292	0.602	140	170	4.682	107	1.06	1.03
10**HDPE**/45**EOC**30/45**EOC**60	0.234	0.512	120	143	5.632	127	0.95	0.86
	0.267	0.468	140	155	5.119	109	0.91	0.87
50**EOC**30/50**EOC**60	0.218	0.473	120	133	6.049	142	0.93	0.79
	0.253	0.428	140	148	5.391	113	0.86	0.81
10**HDPE**/25**EOC**30/65**EOC**60	0.216	0.443	120	132	6.103	110	0.80	0.76
	0.252	0.418	140	147	5.419	126	0.90	0.81
30**EOC**30/70**EOC**60	0.203	0.421	120	125	6.455	128	0.81	0.72
	0.249	0.359	140	145	5.480	99	0.74	0.75

phase at 120°C. The ν_c values change insignificantly and vary approximately from 110 to 140 mol/m^3 at 120°C and from 80 mol/m^3 for HDPE as well as 150 to 170 mol/m^3 for blends at 140°C, respectively. Hereby the strain and stress at break as well as the stress at 100% strain (*E modulus* at high strain) increase with increasing HDPE content and as expected (see Equation (4)) with increasing temperature. Surprisingly, this increase does not correlate with the changes in cross-link density at least for HDPE and blends with high content of HDPE (50HDPE/50EOC30 and 33HDPE/33EOC30/34EOC60). For the explanation of this apparent discrepancy it should be mentioned that HDPE and blends with high HDPE content have explicitly higher crystallinity compared to blends with high content of branched polyethylenes (PE) whereas only the amorphous phase can be cross-linked as per definition. Correspondingly, if in high branched/low crystalline PEs the relatively homogenous distribution of network nodes may be expected, in high crystalline PEs the experimental determined (average) value of cross-link density differs dramatically from local cross-link density in presumably continuous amorphous phase. That entails a changed mechanical behavior of high crystalline PE materials in comparison with low crystalline PEs or PE blends at temperatures above melting temperature of blend components.

The values of strain at break from Table 3 point to the possibility of using a standard programming strain of 100% for investigation of shape memory behavior in present materials since the ε_B values of almost all investigated materials higher than or nearly equal to100%.

3.2. Melting and crystallization behavior

The melting and crystallization behavior of HDPE and HDPE/EOC30/EOC60 blends is displayed in Figure 2. First heating runs for all examined blends exhibit a minimum followed by a maximum in the temperature range between approx. 0 and 70°C caused by annealing at room temperature during storage of prepared samples, as it was shown for uncross-linked EOCs especially with high degree of branching [20]. Since, this phenomenon complicates melting thermograms which are already complex enough, only second heating runs were used for detailed analysis of melting behavior. Second

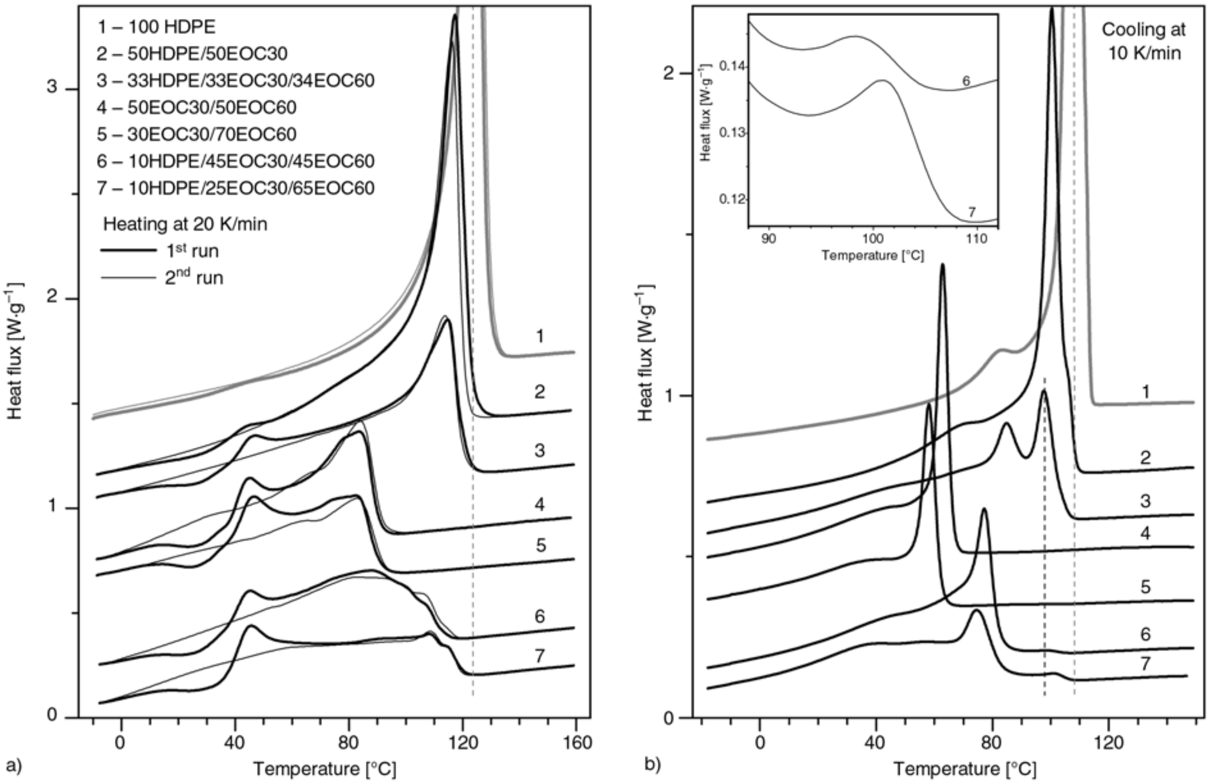

Figure 2. Melting (a) and crystallization (b) DSC thermograms of cross-linked HDPE and HDPE/EOC30/EOC60 blends. The 1st and 2nd heating runs (a) show a melting behavior of specimens stored after preparation for a long time at room temperature and after crystallization at cooling rate of 10 K/min, respectively

Table 4. Melting ($T_{m\mathrm{HDPE}}$, $T_{m\mathrm{EOC30}}$ and $T_{m\mathrm{EOC60}}$) and crystallization temperatures ($T_{c\mathrm{HDPE}}$, $T_{c\mathrm{EOC30}}$ and $T_{m\mathrm{EOC60}}$) of HDPE, EOC30 and EOC60 phases and total melting ($\Delta H_{m\Sigma}$) and crystallization enthalpy ($\Delta H_{c\Sigma}$) of HDPE/EOC30/EOC60 blends, respectively, as well as crystallization enthalpy of HDPE phase ($\Delta H_{c\mathrm{HDPE}}$) depending on blend composition

Blend composition	Melting				Crystallization				
	T_{mHDPE} [°C]	T_{mEOC30} [°C]	T_{mEOC60} [°C]	$\Delta H_{\mathrm{m}\Sigma}$ [kJ/kg]	T_{cHDPE} [°C]	T_{cEOC30} [°C]	T_{cEOC60} [°C]	$\Delta H_{\mathrm{c}\Sigma}$ [kJ/kg]	$\Delta H_{\mathrm{cHDPE}}$ [kJ/kg]
100**HDPE**	124.3	–	–	139	108.0	–	–	139	139
50**HDPE**/ 50**EOC**30	116.1	[1]	[1]	108	100.3	~71	–	109	~75
33**HDPE**/ 33**EOC**30/ 34**EOC**30	114.0	[1]	[1]	86	97.7	84.7	~20[2]	89	~20
50**EOC**30/ 50**EOC**60	–	85.0	~68[2] ~35[2]	68	–	62.8	~46[3]	68	–
30**EOC**30/ 70**EOC**60	–	82.7	64.7 ~35[2]	64	–	58.2	~39[3]	63	–
10**HDPE**/ 45**EOC**30/ 45**EOC**60	~114[2] ~105[3]	~91[3] 82.9	~53[2]	74	97.7	77.2	~45[3]	73	~0.7
10**HDPE**/ 25**EOC**30/ 65**EOC**60	~115[3] 108.3	~94[2] ~79[2]	~61[3] ~30[2]	65	100.3	74.3	55.7 40.3	68	~1.5

[1] the peaks or shoulder which are assignable to EOC30 or EOC60 phase were not found in the thermogram;
[2] weak and flat shoulder;
[3] distinct shoulder

heating runs are recorded after crystallization at a cooling rate of 10 K/min and with short dwell time at lowest temperature of the experiment what agrees well with measuring conditions in SM experiments described beneath.

Generally, as illustrated in Figure 2 and Table 4 all blends, especially ternary blends demonstrate *multiple* behavior for both melting and crystallization. In 10HDPE/45EOC30/45EOC60 and 10HDPE/25EOC30/65EOC60 blends the HDPE phase crystallizes not only at 97.7 and 100.3°C, respectively, because the crystallization enthalpy estimated on the basis of these small peaks, which are depicted with high resolution in insert of Figure 2a, amounts to just approx. 5 and 10% of the expected value, respectively, (see Table 4; cp. with ΔH_c value of 'bulk' cross-linked HDPE). The $\Delta H_{c\mathrm{HDPE}}$ value of 33HDPE/33EOC30/34EOC60 blend is at least two times lower than expected. These differences between real and expected $\Delta H_{c\mathrm{HDPE}}$ values cannot be satisfactory explained on the basis of the difference in cross-link density between HDPE and blends (see Table 3) due to the fact that at 'pure' EOC30 the doubling of cross-link density results in a crystallinity decrease of only 1 to 3% at 25°C depending on the thermal history of specimen [10]. Moreover, the local cross-link density in the HDPE phase is by all means lower than the average cross-link density of the blend as a whole as given in Table 3. Obviously, the described behavior of blends suggests the crystallization of the main part of HDPE phase together with the EOC30 phase (or some part of it) at significantly lower temperature. Interestingly, the melting of the HDPE phase in 10HDPE/45EOC30/ 45EOC60 and 10HDPE/25EOC30/65EOC60 blends occurs also stepwise in two stages (see Figure 2a, curves 6 and 7).

The melting (T_m) and crystallization temperature (T_c) of the HDPE phase decrease markedly with decreasing HDPE content in the blend compared to the values for 'bulk' cross-linked HDPE. At the same time, T_m and T_c values of the EOC30 phase can increase in blends containing HDPE or decrease in binary blends with high branched EOC60 (see Table 4; cp. with T_m values of approx. 91 and 57°C for 'pure' EOC30 and EOC60, respectively, having a similar cross-link density).

If the increase of $T_{c\mathrm{EOC30}}$ and correspondingly $T_{m\mathrm{EOC30}}$ values can be explained as a result of the nucleating effect of existing HDPE crystallites in the cooling run, both the decrease of T_c and T_m values of HDPE and EOC30 phases as well as a *multi-*

ple melting and fractionated crystallization behavior points indirectly at significant molecular interaction of blend components in molten state but solely in regions where the molecular level of mixing before cross-linking was achieved. In blends both the nucleating effect of HDPE crystallites and molecular interaction are available only in *un*cross-linked crystalline domains which consist of ethylene sequences of blend components with suitable length. The cross-linking fixes partly the content, number and size of these domains but their perfection and structure can be changed depending on thermal history.

Due to the existence of several populations of PE crystallites of different stability and correspondingly with different melting temperatures in the described blends the thermograms in Figure 2a show nearly continuous melting that stretches across a very wide temperature range by what the macroscopic thermal-mechanical and in particular SM behavior of these blends (see section 3.4) is affected.

It should be noted that the total melting and crystallization enthalpy of blends decrease as expected with decreasing content of components with higher ability to crystallization (HDPE and EOC30).

3.3. Phase morphology

Mode and mechanism of phase morphology formation in present blends differ considerably from the behavior that demonstrate conventional polymer blends *firstly* due to high affinity of components which all are basically polyethylenes with degree of branching of approx. 0, 30 and 60 CH_3/1000C and with close-by values of MI/melt viscosity and *secondly* in consequence of melt structure and its fixation and of crystallization restrictions caused by cross-linking.

The lamellae or some part of them can be a part of chain sections which serve as links between network nodes. Alternatively, the crystallites (e.g. lamellae or their agglomerates) may be bound by links, namely unordered chain sections which form covalent network nodes on the crystallite surface. Obviously, both mechanisms take place but within the framework of present work it is not possible to establish which kind of links dominates and is more related to shape-memory properties.

Phase separation in amorphous regions takes definitely place already in molten state before the start of cross-linking and is evidently caused by the different average degree of branching of the blend partners [21] and the inhomogeneous distribution of branches between and along the molecular chains. According to [21] the linear HDPE and EOC30 should be miscible on the molecular level at temperatures ≥150°C. In contrast, the blend of HDPE and EOC60 cannot exhibit miscibility at processing temperatures. In branchless domains of sufficiently wide meshed network the molecular chains can be ordered in the course of cooling, but the crystallization must be pronounced restricted due to the melt structure and its fixation as a result of cross-linking. Thus, some part of crystallites can arise due to *co*-crystallization of suitable ethylene sequences of HDPE and EOCs whereon the crystallization behavior indirectly points (see section 3.2). At the same time, each blend component can also crystallize separately. Consequently the formation of multiple crystal populations of different size/stability and perfection may be expected.

In this connection the AFM images (Figure 3) demonstrate such a wide variety of morphology elements. In addition to certain number of dispersed particles the AFM images show a tendency to the formation of continuous phases which are however inhomogeneous, i.e., they include both amorphous and crystalline parts. The phase morphology of 50HDPE/50EOC30 and 33HDPE/33EOC30/34EOC60 blends (see Figure 3a and 3b), in which multiple shape-memory effect appears most pronounced (see section 3.4), exhibits distinct trend to the formation of nearby continuous extended macro domains integrated into the matrix that consists presumably of crystallites as e.g. lamellae and 'small' amorphous regions with a size of less than 100 nm. It seems that 'big' amorphous domains of approximately 150 and 500 nm in size for 50HDPE/50EOC30 and 33HDPE/33EOC30/34EOC60 blends, respectively, are enclosed into the 'crystalline' matrix. Lower differences in the degree of branching between the components and the smaller average degree of branching of 50HDPE/50EOC30 compared to other blends result in explicitly finer phase morphology with more pronounced separation of crystalline and amorphous phases. Here, it should be noted that enclosed 'big'

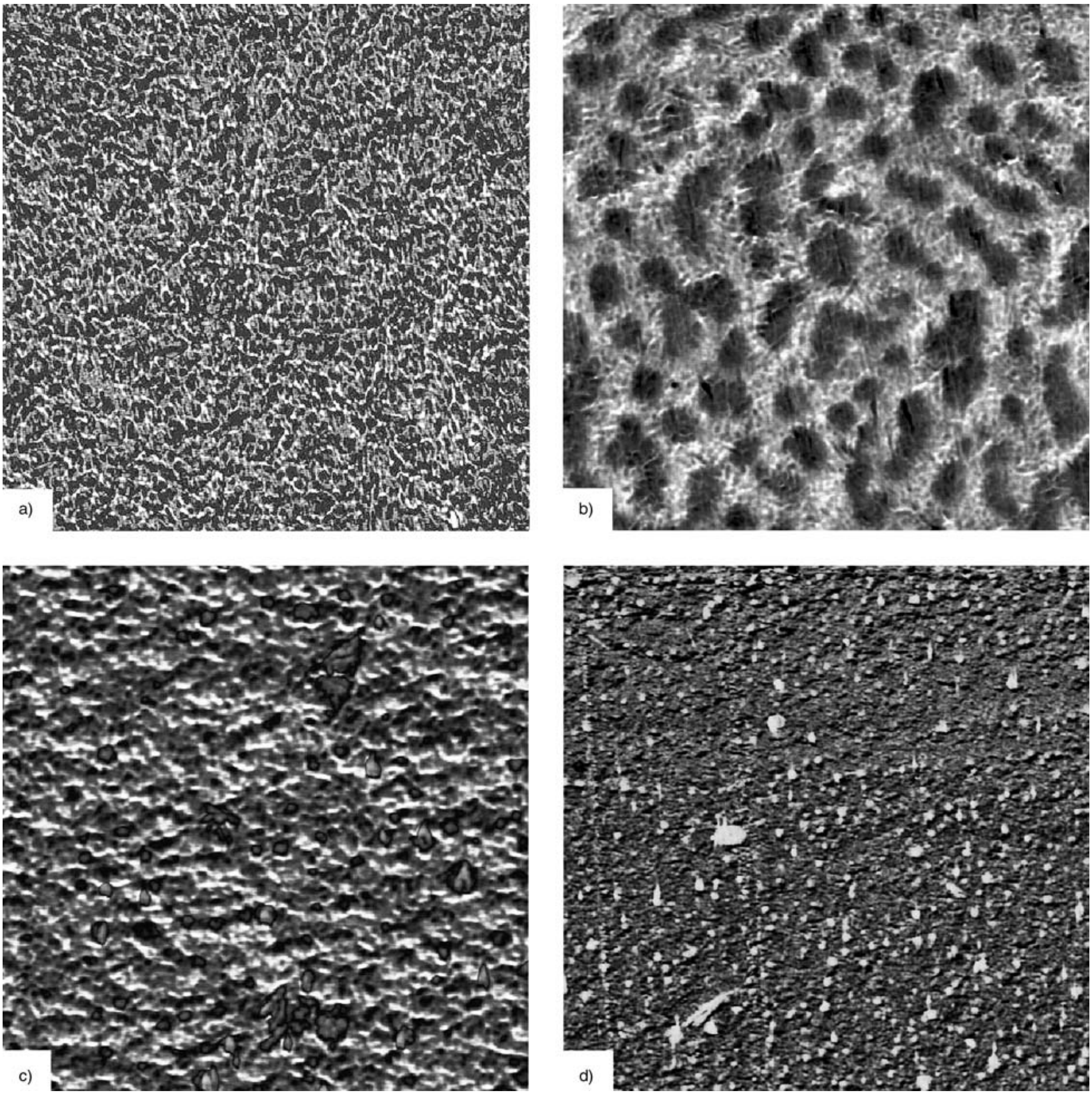

Figure 3. AFM phase images of 50HDPE/50EOC30 (a), 33HDPE/33EOC30/34EOC60 (b) and 10HDPE/25EOC30/65EOC60 blends (c and d) with size of 5×5 μm^2

amorphous domains in the 33HDPE/33EOC30/34EOC60 blend appear some softer in harder regions which are accordingly less or more ordered. In other blends, e.g. in 10HDPE/25EOC30/65EOC60, significant differences in the phase morphology of various regions exist that can be caused by an insufficient mixing quality in the single screw extruder and/or by the decomposition following processing before cross-linking. Two representative images in Figure 3c and 3d demonstrate the relatively fine smooth phase structure with a size of approx. 50 to 150 nm and sharp segregated nearly spherical hard particles assumedly of HDPE with a size of approx. 30 to 300 nm (Figure 3d), respectively.

3.4. Shape-memory behavior

The temperature dependence of SM recovery strain and recovery strain rate of HDPE and HDPE/EOC30/EOC60 blends and their components having a network with similar cross-link density are demonstrated in Figure 4. Here, the findings of the first cycle of SM tests are demonstrated. The results evaluating these curves are presented in Table 5.

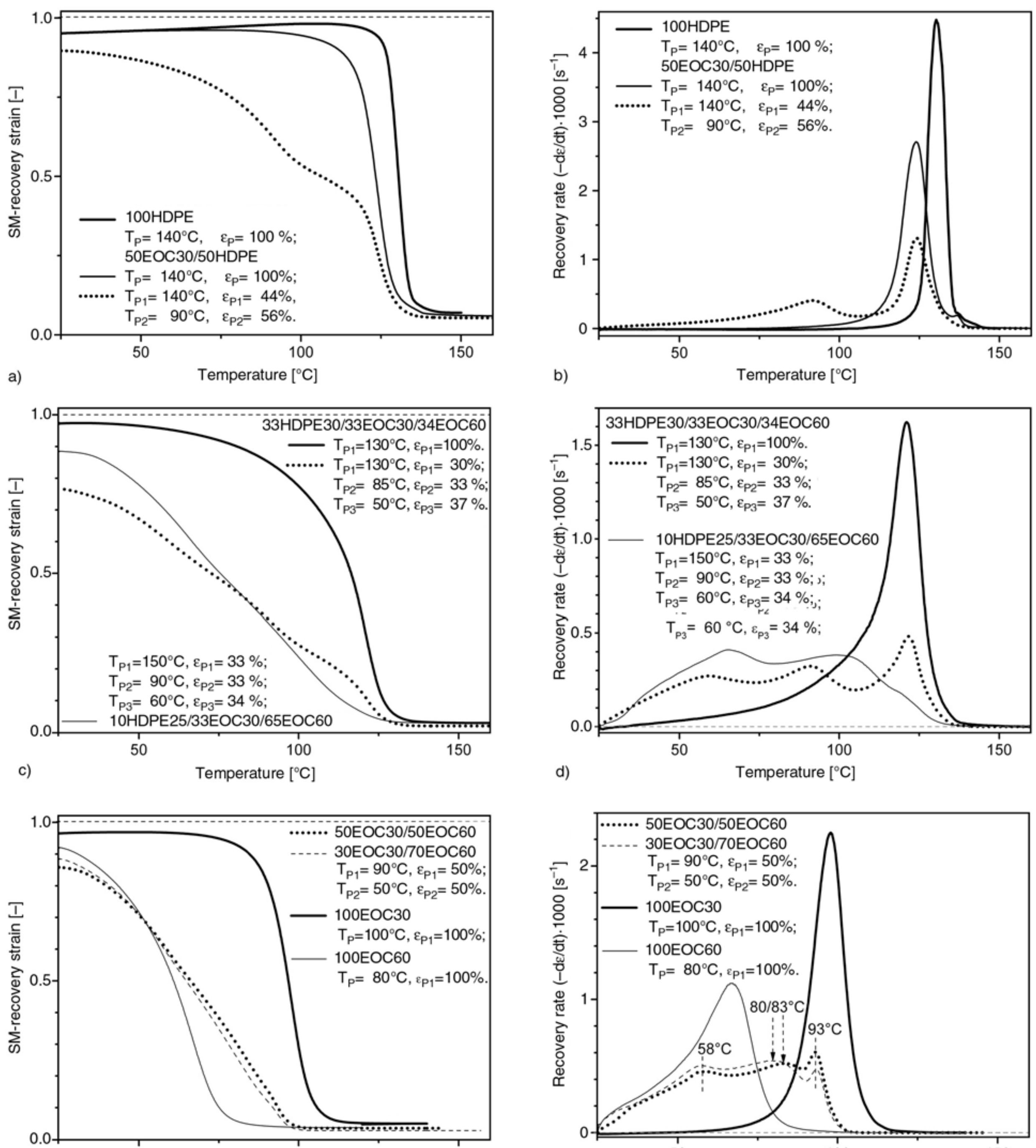

Figure 4. Effect of composition and programming conditions on the temperature dependence of SM recovery strain (a, c and e) and recovery strain rate (b, d and f) of HDPE and HDPE/EOC30/EOC60 blends

The sharp step of SM recovery strain and high, well separated peaks of SM recovery rate can be generated only by melting of a phase with sufficient crystallinity and relatively perfect crystallites which produce strong and well separated DSC peaks. For the explicit appearance of SME the availability of stored sufficiently high visco-elastic forces is important no less than suitable melting behavior. These visco-elastic forces caused by network deformation during programming must be efficiently stored by the crystalline structure formed in the actual temperature range, i.e. the crystalline structure must hold the reached deformation after unloading.

As expected, the blends having a higher average crystallinity which exhibit the distinct well

Table 5. Shape memory characteristics of HDPE, EOC30 and EOC60 phases and their blends including strain fixing (R_f) and strain recovery ratios (R_r), response temperature T_{res} as well as peak value of SM recovery rate $[-d\varepsilon/dt]_{max}$

Composition	R_f [%]	R_r [%]	T_{res} [°C]			$[-d\varepsilon/dt]_{max} \cdot 10^3$ [s^{-1}]		
			1	2	3	1	2	3
100**HDPE**	95.0	93.0	130.3	x	x	4.47	x	x
50**HDPE**/ 50**EOC**30	95.0	94.0	124.1	x	x	2.71	x	x
	90.0	95.0	124.1	91.8	x	1.32	0.41	x
33**HDPE**/ 33**EOC**30/ 34**EOC**30	97.0	97.0	121.1	x	x	1.62	x	x
	76.7	98.0	121.7	91.0	59.2	0.48	0.33	0.27
10**HDPE**/ 25**EOC**30/ 65**EOC**60	88.5	97.0	~120*	98.8	65.6	0.17	0.38	0.41
100**EOC**30	96.8	95.0	97.6	x	x	2.25	x	x
50**EOC**30/ 50**EOC**60	85.8	96.0	58.3	83.0	93.1	0.46	0.52	0.60
30**EOC**30/ 70**EOC**60	85.8	97.0	57.5	80.0	93.3	0.51	0.54	0.47
100**EOC**60	108.3	96.0	66.9	x	x	1.12	x	x

*shoulder which is assignable to the HDPE phase was not found in the DSC thermogram

resolved melting peaks exhibit the high strain fixity ratio R_f and SM recovery rate $-d\varepsilon_{rec}/dt$. Correspondingly, these parameters increase with increasing HDPE (and partly EOC30) content in the blends. The *single*-step programming of all blend types results in appearance of only one step and accordingly one peak in the temperature dependences of the SM recovery strain and SM recovery rate, respectively, i.e. in *dual*-shape behavior. It should be noted that these programming experiments were carried out at a temperature higher than the melting temperature of HDPE or EOC30 (depending on blend composition), i.e. at temperature at which entire blend is kept in molten state. Compared to the specimens arranged by means of *single*-step programming the same blends after *two*- or *three*-step programming show significantly lower R_f and $-d\varepsilon_{rec}/dt$ values and particularly $[-d\varepsilon_{rec}/dt]_{max}$ values at melting temperatures of the components (see Figure 4 and Table 5). The decrease of R_f values as a result of multi-step programming is caused by the partial deformation of already crystallized (fixed) phase/phases by each next programming step at lower temperature. These strain components are not fixed due to subsequent crystallization at lower programming temperature and are predominantly reversible at low temperature. The temperatures for *two*- or *three*-step programming were chosen allowing for the temperatures of a quiescent crystallization of present crystal populations obtained by means of DSC. Obviously, however a potential strain-induced crystallization should be taken into account. Perhaps the multi-shape behavior can be improved on the basis of further optimization of both programming temperatures and dwell periods. For this purpose, due to the possibility of partly strain-induced crystallization by programming [11, 12] the crystallization temperatures of blend components must be stated more precisely under load. The long-term stress relaxation experiments at programming temperatures and then subsequently SM recovery tests are necessary in order to reduce as much as possible the non-stored component of visco-elastic forces by means of suitable increasing of programming period, respectively. The last declaration hypothesizes that in already crystallized phase/crystal populations the structure changes connected with partial transformation of elastic and visco-elastic deformation of network to plastic deformation of existing crystalline phase can take place and are in need of more time as dwell period used in present work (120 s). Furthermore, with decreasing programming temperature the decrease of diffusion velocity of yet moveable chains is due. In this connection the better fixing of intermediate shape due to more completed isothermal and strain induced crystallization and presumptive creep of existing crystalline formations at longer programming dwell can be expected.

All investigated blends and their components independent from programming mode demonstrate relatively high values of strain recovery ratio (R_r) that amounts approx. 93 to 98%.

Presumably, the *multi*-shape behavior by *single*-step programming may be carried out only in a heterogeneous polymer material having hypothetical phase morphology with preferred orientation of planar phase layers perpendicularly to load direction. However, if the same heterogeneous polymer material will be loaded parallel to planar phase layers the *multi*-shape behavior would be basically impossible because the specimen length in recovery stage can substantial change only after melting in layer with highest melting temperature starts. Thus, the important disadvantage of such hypothetical heterogeneous polymer material would be total anisotropy and as a consequence the inability to *multi*-shape behavior by programming load in two perpendicular directions what is important for some applications [11, 12].

4. Conclusions

Tensile test at 120 and 140°C *firstly* has permitted the evaluation of average cross-link density of blends that amounts approx. 110÷170 $\mathrm{mol \cdot m^{-3}}$ depending on content and temperature, *secondly* has shown that by default used programming strain of 100% is acceptable for all blends, *thirdly* pointed at an increase of programming stress at strain of 100% and correspondingly of stored visco-elastic forces with increasing in blend part of components with higher crystallinity (EOC30 and predominantly HDPE).

The finding of the investigation of EOC/HDPE blends show that multiple SM behavior appears only at consequent stepwise application of convenient programming strains and temperatures. However, only for 50HDPE/50EOC30 blend which shows especially fine disperse and distinctly segregated phase morphology the temperature dependence of SM recovery strain demonstrates two pronounced steps. All other binary and tertiary EOC/HDPE blends exhibit the *triple*- and *quadruple*-shape-memory effect, respectively, only as very diffuse steps in SM recovery strain curves and as small, superimposed peaks of SM recovery rate vs. temperature. Obviously, that is caused by multiple melting behavior of these blends with many poorly separated peaks.

In spite of described problems the present blends have a good potential for further development and successful application. It should be also noted that some applications could be in need of gradual changes of sample geometry with low thermal-induced recovery strain rate. In the investigations the blends will be prepared with different degree of component dispersion as well as blends having a uncross-linked crystallizable disperse phase/phases.

Acknowledgements

The authors gratefully acknowledge the financial support by Deutsche Forschungsgemeinschaft (DFG). Samples of DHBP peroxide were kindly provided by Degussa Peroxygen Chemicals, Degussa Initiators GmbH & Co KG (Germany).

References

[1] Ota S.: Current status of irradiated heat-shrinkable tubing in Japan. Radiation Physics and Chemistry, **18**, 81–87 (1981).

[2] Kleinheins G., Starkl W., Nuffer K.: Besonderheiten bei der Qualitätssicherung strahlungsvernetzter Wärmeschrumpferzeugnisse. Kunststoffe, **74**, 445–449 (1984).

[3] Lendlein A., Langer R.: Biodegradable, elastic shape-memory polymers for potential biomedical applications. Science, **296**, 1673–1676 (2002).

[4] Lendlein A., Kelch S.: Shape-memory polymers. Angewandte Chemie, International Edition, **41**, 2034–2057 (2002).

[5] Behl M., Lendlein A.: Actively moving polymers. Soft Matter, **3**, 58–67 (2007).

[6] Ratna D., Karger-Kocsis J.: Recent advances in shape memory polymers and composites: A review. Journal of Materials Science, **43**, 254–269 (2008).

[7] Li F., Chen Y., Zhu W., Zhang X., Xu M.: Shape memory effect of polyethylene/nylon 6 graft copolymers. Polymer, **39**, 6929–6934 (1998).

[8] Li F., Zhu W., Zhang X., Zhao C., Xu M.: Shape memory effect of ethylene-vinyl acetate copolymers. Journal of Applied Polymer Science, **71**, 1063–1070 (1999).

[9] Kolesov I. S., Radusch H.-J.: Formgedächtnis in vernetzten Ethylen-1-Octen-Copolymeren. in: 'Proceedings of '11. International Conference Polymeric Materials 2004. Halle/Saale, Germany' PII–50 (2004).

[10] Kolesov I. S., Androsch R., Radusch H.-J.: Thermal-mechanical stability of covalent network and shape memory effect in ethylene-1-octene copolymers cross-linked by peroxides. in 'CD Proceeding of PPS-23 – The Polymer Processing Society 23rd Annual Meeting 2007. San Salvador, Brazil' P11-005, 1–6 (2007).

[11] Bellin I., Kelch S., Langer R., Lendlein A.: Polymeric triple-shape materials. Proceedings of the National Academy of Science of the USA, **103**, 18043–18047 (2007).

[12] Bellin I., Kelch S., Lendlein A.: Dual-shape properties of triple-shape polymer networks with crystallisable network segments and grafted side chains. Journal of Materials Chemistry, **17**, 2885–2891 (2007).

[13] Bensason S., Minick J., Moet A., Chum S., Hiltner A., Baer E.: Classification of homogeneous ethylene-octene copolymers based on comonomer content. Journal of Polymer Science: Part B, Polymer Physics, **34**, 1301–1315 (1996).

[14] Varga J., Menczel J., Solti A.: Memory effect of low-density polyethylene crystallized in a stepwise manner. Journal of Thermal Analysis and Calorymetry, **10**, 433–440 (1976).

[15] Sajkiewicz P., Phillips P. J.: Peroxide crosslinking of linear low-density Polyethylenes with homogeneous distribution of short chain branching. Journal of Polymer Science, Part A: Polymer Chemistry, **33**, 853–862 (1995).

[16] Hoffmann M.: Der Einfluß von Verhakungen auf das Dehnungsverhalten von vernetzten Polymeren. Kolloid-Zeitschrift und Zeitschrift für Polymere, **250**, 197–206 (1972).

[17] Heinrich G., Straube E., Helmis G.: Molekularstatistische Theorien polymerer Netzwerke. Fortschrittsbericht. Acta Polymerica, **31**, 275–286 (1980).

[18] Treloar L. R. G.: The physics of rubber elasticity. Oxford University Press, New York (2005).

[19] Smedberg A., Hjertberg T., Gustafsson B.: Effect of molecular structure and topology on network formation in peroxide crosslinked polyethylene. Polymer, **44**, 3395–3405 (2003).

[20] Androsch R., Wunderlich B.: A study of annealing of poly(ethylene-co-octene) by temperature-modulated and standard differential scanning calorimetry. Macromolecules, **32**, 7238–7246 (1999).

[21] Shin K., Nam B. U., Bang J., Jho J. Y.: Melt-state miscibility of poly(ethylene-co-1-octene) and linear polyethylene. Journal of Applied Polymer Science, **107**, 2584–2587 (2008).

eXPRESS Polymer Letters Vol.2, No.7 (2008) 474–484
Available online at www.expresspolymlett.com
DOI: 10.3144/expresspolymlett.2008.57

Effect of temperature on tensile properties of injection moulded short glass fibre and glass bead filled ABS hybrids

*S. Hashemi**

London Metropolitan Polymer Centre, London Metropolitan University, UK

Received 24 March 2008; accepted in revised form 30 April 2008

Abstract. The present study investigated the effect of temperature on tensile strength and modulus of injection moulded ABS polymer reinforced with both short fibres (GF) and spherical glass beads (GB) over the temperature range 25 to 100°C. Tensile strength, σ_h and modulus, E_h, of ABS/GF/GB hybrids increased as volume fraction of the total glass in the hybrids increased. A linear increase in σ_h and E_h was found with increasing the hybrid ratio of the glass fibre, χ_f, over the entire temperature range studied. Results indicated that the tensile properties of the ABS/GF/GB hybrid composites at any temperature, T, can be estimated from the rule-of-hybrid-mixtures of the form $P_h = P_{cf}\chi_f + P_{cb}(1 - \chi_f)$ where P_{cf} and P_{cb} are the tensile properties of the ABS/GF and ABS/GB composites at temperature T, respectively. It was found also that σ_h and E_h both decrease with increasing temperature in a linear manner. The rate at which σ_h and E_h decreased with temperature was dependent upon the hybrid ratio of the glass fibre, χ_f, and the total concentration of the glass in the hybrids.

***Keywords:** polymer composites, hybrids, mechanical properties, temperature*

---

1. Introduction

It is well recognised that the mechanical properties of polymer composites such as strength and modulus are derived from a combination of the filler and matrix properties and the ability to transfer stresses across the interface between the two constituents. These properties, however, are affected by a number of parameters, such as the concentration of the filler, geometrical shape and the aspect ratio of filler and the degree of interfacial adhesion between the filler and the matrix [1–9]. For example, whist addition of short fibres to polymers matrices enhances strength, addition of spherical shaped particles (e.g. glass beads) cause deterioration. On the other hand, spherical particles with aspect ratio of unity provide isotropic mouldings whereas short fibres having aspect ratio much greater than unity provide anisotropic mouldings. Fibre composites although are strong and stiff when loaded longitudinally (along the length of the fibres) they are quite weak and less stiff when loaded transversely (normal to the fibres).

Hybridisation provides other dimensions to the potential versatility of composite materials. For example, by incorporating glass fibres and glass beads in the same matrix, one may obtain a moulding which may not be as stiff as the fibre reinforced system but stronger than the glass bead system [10, 11].

The study by Philips [12] raised the issue surrounding the possible synergistic hybrid effects, in which the properties of the hybrid composite might not follow from a direct consideration of the independent properties of the individual components. A positive or negative hybrid effect was then defined as a positive or negative deviation of a certain mechanical property from the rule-of-mixtures behaviour. In general, tensile strength and modulus of hybrid

---

*Corresponding author, e-mail: s.hashemi@londonmet.ac.uk

systems do conform to rule of mixtures [10, 11]. However, the majority of hybrid studies have been conducted at room temperature. Indeed, little is known on the effect of temperature on hybrid properties such as tensile strength and modulus. To this end, this work was undertaken to study the effect of temperature on tensile strength and modulus of ABS polymer filled with short glass fibre and glass bead particles (i.e., ABS/GF/GB hybrid), over the temperature range 25 to 100°C. To examine the applicability of the rule-of-hybrid-mixtures, tensile properties of ABS/GF and ABS/GB composites were also studied under the same conditions as the hybrid composites.

2. Experimental details

2.1. Materials

Owens Corning chopped E-glass fibres (GF) of approximately 6.0 mm in length and 10 μm in diameter and Potters solid spheriglass CP-3000 spherical glass beads (GB) of approximately 12–26 μm in diameter were used as reinforcing fillers for Acrylonitrile Butadiene Styrene (ABS) copolymer received by Bayer (Novodut P2H-AT). The ABS and the reinforcing fillers were used to produce a series of ABS/GB, ABS/GF and ABS/GB/GF compounds with nominal glass contents of 10, 20 and 30% w/w.

2.2. Compounding

The materials listed in Table 1 were at first mixed to the desired glass content and then dried in an oven at 80°C for 4 hours. After drying, each formulation was passed through a Leistritz micro 18GL-7R co-rotating twin-screw extruder at an average screw speed of 60 rpm to produce a homogeneous dispersion of bead and or fibre throughout the matrix. The extruder temperature profile was 203/232/232/235°C and the die diameter was 4 mm. The extrudates emerging from the die exit were continuously cooled in a water bath and fed through a granulator to produce pellets for injection moulding process. Pellets were dried in an oven at 80°C for 4 hours before being injection moulded into test specimens.

Table 1. Formulation for composites and hybrids. (χ_f = concentration of glass fibres divided by the concentration of total glass)

	ABS/Glass Composites			
	Total glass [wt%]	**GF [wt%]**	**GB [wt%]**	**Hybrid ratio, χ_f [–]**
ABS/GB	10	0	10	0
	20	0	20	0
	30	0	30	0
ABS/GF	10	10	0	1
	20	20	0	1
	30	30	0	1
Hybrids	10	5	5	0.50
	20	5	15	0.25
	20	10	10	0.50
	20	5	5	0.75
	30	20	20	0.33
	30	15	15	0.50
	30	10	10	0.67

2.3. Specimen preparation

BS EN ISO-527 dumbbell shaped tensile bars were produced using a Negri Bossi NB60 injection-moulding machine at the processing conditions listed in Table 2. The mould used consisted of a single gate cavity producing dumbbell shaped tensile bars of dimensions shown in Figure 1.

Table 2. Injection moulding processing conditions

Processing condition	100% ABS matrix	Composites & hybrids with 10% total filler	Composites & hybrids with 20% total filler	Composites & hybrids with 30% total filler
Barrel temperature [°C]				
Zone 1	230	230	230	230
Zone 2	230	230	232	232
Zone 3	232	232	235	235
Mould temperature [°C]	70	70	80	80
Injection pressure [MPa]	8.5	8.5	9	9
Holding pressure [MPa]	3	3	3	3
Cooling time [s]	30	30	30	30
Cycle time [s]	33	33	33	33
Shot weight [g]	27	28	28	29

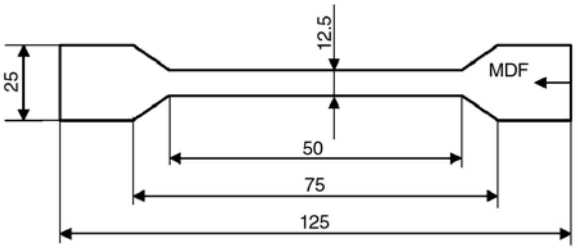

Figure 1. Dimensions of single-gated specimens in millimetres

2.4. Filler concentration measurements

The concentration of total glass in each material was determined from the glass residue remained by burning at 550°C three weighed samples that were cut from the gauge length of the moulded specimens. After cooling, the ash of glass residue was weighed and the exact weight fraction of glass (w_g) was determined. The w_g values were subsequently converted into glass volume fractions ϕ_g using Equation (1):

$$\phi_g = \left[1 + \frac{\rho_g}{\rho_m}\left(\frac{1}{w_g} - 1\right)\right]^{-1} \tag{1}$$

Taking the density of the matrix (ρ_m) as 1.12 $\mathrm{kgm^{-3}}$ and density of glass (ρ_g) as 2.54 $\mathrm{kgm^{-3}}$ gave average glass fibre concentration values of 4.4, 9.5 and 15.5% v/v in GF composites and average glass bead concentration values of 4.2, 9.1 and 14% v/v in GB composite. The volume fraction of glass fibres, ϕ_f, and glass beads, ϕ_b, in each hybrid was calculated from ϕ_g and the hybrid ratio.

2.5. Fibre length measurements

The ash of fibrous material was subsequently spread on a glass slide and placed on the observation stage of a microscope. Magnified fibre images were transmitted to a large screen, and the fibre images were then automatically digitised using Linkam Scientific RTVMS software. From the fibre length distributions, the average fibre length values (L_f) of 550, 430 and 360 µm were obtained for 4.4, 9.5 and 15.5% v/v glass fibre composites, respectively. Results show decrease in L_f with increasing ϕ_f thus indicating that the average length of the fibre in the moulded specimens was affected by the concentration level of the fibres. The increased damage to fibre length with increasing ϕ_f was attributed to a greater degree of fibre-fibre interaction and increased in melt viscosity at higher fibre loadings. The latter give rise to higher bending forces on the fibres during compounding and moulding process causing the fibres to break, as noted here.

2.6. Mechanical testing

Dumbbell specimens were tested in tension in an Instron 4466 testing machine using pneumatic clamps. Tensile tests were performed at 25, 60 and 100°C at a constant crosshead displacement rate of 50 mm/min. The load-displacement curve for each specimen was recorded using a computer data logger from which tensile modulus and strength were calculated using the initial slope and load at maximum, respectively. For each material at least six specimens were tested at a given temperature. The average tensile strength and modulus values are reported here. The standard deviation for tensile strength and modulus was no more than 2 MPa and 0.08 GPa, respectively.

3. Results and discussions

3.1. ABS/GF composites

The load-extension curves for ABS showed a clear yield point before failure. The incorporation of glass fibres into ABS reduced the overall deformation but enhanced the tensile strength and modulus of the ABS matrix. It must be said, that failure of the ABS/GF composites was brittle over the entire temperature range studied here whereas that of the ABS matrix was ductile. Close examination of the load-extension curves revealed that whilst deformation of the composites was linear at low stresses, it was nonlinear at higher stresses. This observation indicated that interfacial microfailure had occurred around the fibres in the composites during tensile loading.

The effect of fibre concentration, ϕ_f, on tensile modulus of ABS/GF composites, E_{cf}, at 25, 60 and 100°C is shown in Figure 2 where it can be seen that at a any given temperature E_{cf} increases linearly with increasing ϕ_f. The linear dependence between E_{cf} and ϕ_f is consistent with the modified 'rule-of-mixtures' given by Equation (2):

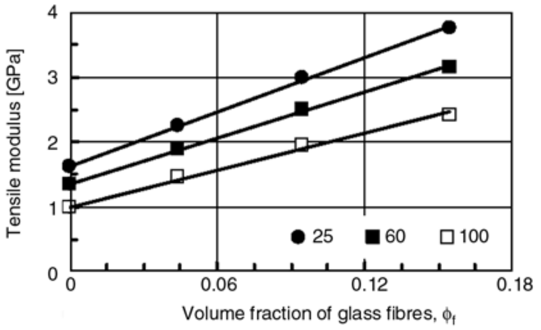

Figure 2. Tensile modulus of ABS/GF composite, E_{cf}, versus volume fraction of glass fibres, ϕ_f, at 25, 60 and 100°C

$$E_{cf} = E_m + (\lambda_1\lambda_2 E_f - E_m)\phi_f \tag{2}$$

where E_{cf} and E_m are the tensile modulus values of ABS/GF and the ABS matrix at temperature T and E_f is the modulus of the glass fibres taken in this study as 75 GPa and assumed to be independent of temperature. λ_1 and λ_2 are, respectively, the fibre length and fibre orientation factors for tensile modulus, taking into account fibre misalignment and fibre length variation in the composite. Equation (2) can alternatively be written in the form of Equation (3):

$$E_{cf} = E_m + (\lambda_E E_f - E_m)\phi_f \tag{3}$$

where $\lambda_E = \lambda_1\lambda_2$ is termed the overall fibre efficiency factor for composite modulus. According to Equation (3), value of λ_E at any given temperature can be determined from the slope of the line E_{cf} versus ϕ_f. Using the slope of the linear regression lines in Figure 2, one obtains the variation in λ_E with temperature as depicted in Figure 3. As can be seen, over the temperature range studied here, λ_E is much less than one and decreases with increasing temperature in a linear manner. The linear dependence in Figure 3 can be expressed by Equation (4):

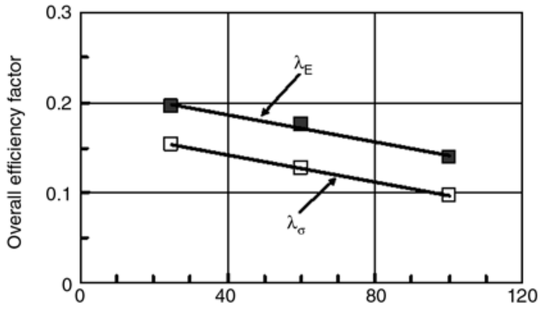

Figure 3. Overall efficiency factors for tensile modulus, λ_E, and tensile strength, λ_σ, of ABS/GF composites versus temperature, T

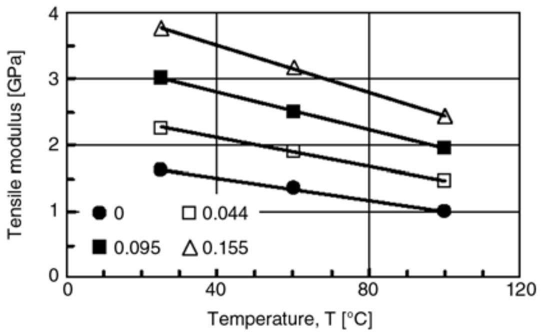

Figure 4. Tensile modulus of ABS/GF composite, E_{cf} versus temperature, T, for fibre volume fractions, ϕ_f, of 0, 0.044, 0.095 and 0.155

$$\lambda_E = 0.217 - 7.63\cdot 10^{-4}\,T \tag{4}$$

The effect of temperature on tensile modulus of ABS/GF composites is more explicitly shown in Figure 4 where it can be seen that E_{cf} decreases linearly with increasing temperature. It can be seen also that the rate of decrease as given by the slope of the lines in Figure 4 (i.e. $\mathrm{d}E_{cf}/\mathrm{d}T$) depends on the volume fraction of glass fibres in the composites. As shown in Figure 5, when $\mathrm{d}E_{cf}/\mathrm{d}T$ values are plotted against ϕ_f, one obtains a linear dependence given by Equation (5):

$$\frac{\mathrm{d}E_{cf}}{\mathrm{d}T} = -(0.0083 + 0.060\phi_f) \tag{5}$$

According to Cox shear lag model [13], fibre length efficiency factor λ_1 can be evaluated from the relationship given by Equation (6):

$$\lambda_1 = 1 - \frac{\tanh\beta}{\beta} \tag{6}$$

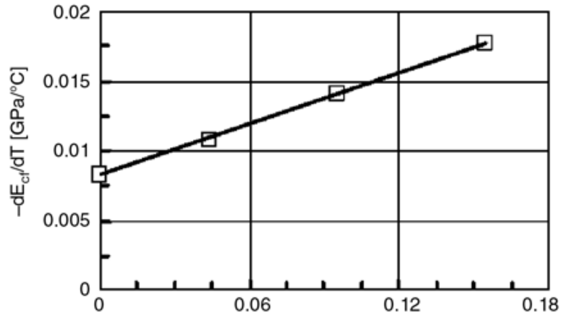

Figure 5. Effect of ϕ_f on the slope of the line E_{cf} versus temperature in Figure 4

where β is defined by Equation (7):

$$\beta = \frac{\overline{L}_f}{2}\left(\frac{4E_m}{E_f d^2 \ln\varphi}\right)^{\frac{1}{2}} \tag{7}$$

where d is the diameter of the fibres. For square packing arrangement of fibres, φ can be obtained from the relationship given by Equation (8):

$$\varphi = \sqrt{\frac{\pi}{4\phi_f}} \tag{8}$$

Values of λ_1 calculated via Equation (6) are presented in Table 3 where it can be seen that λ_1 decreases with increasing temperature but shows no significant variation with respect to ϕ_f. Also given in Table 3 are values of λ_2 obtained from the ratio λ_E/λ_1 and as can be seen λ_2 decreases with increasing temperature and increases slightly with increasing ϕ_f.

The effect of fibre volume fraction on tensile strength of ABS/GF composites, σ_{cf}, at 25, 60 and 100°C is shown in Figure 6 where it can be seen that over the entire temperature range studied here, σ_{cf} increases with increasing fibre concentration in a nonlinear manner showing tendency towards levelling off or reaching a maximum on approaching fibre concentration value of approximately 16% v/v. The levelling off effect (or reaching a maximum) which is also noted in several other injection moulded glass reinforced polymer systems [3, 4, 8, 9] is mainly attributed to the separation distance between the fibres becoming sufficiently small as to restrict the flow of the matrix material between fibres. This effect and the higher stress concentration in the matrix due to the greater number of fibre ends at high ϕ_f, reduces the gain in strength which one would expect otherwise.

The nonlinear rise in σ_{cf} with increasing ϕ_f as depicted in Figure 6 can be described by a second order polynomial function of the form given by Equation (9):

$$\sigma_c = a_0 + a_1\phi_f + a_2\phi_f^2 \tag{9}$$

However, as illustrated in Figure 7, for fibre concentration values in the range 0 to 10% v/v, variation of σ_{cf} with ϕ_f is reasonably linear with regression coefficients of greater than 0.97. Within this ϕ_f range, variation of σ_{cf} with ϕ_f can be described by the modified 'rule-of- mixtures' for tensile strengths as given by Equation (10):

$$\sigma_{cf} = \sigma_m + (\lambda_3\lambda_4\sigma_f - \sigma_m)\phi_f \tag{10}$$

where σ_f is tensile strength of the glass fibres taken in this study as 2470 MPa and σ_m is the tensile strength of the ABS matrix. λ_3 and λ_4 are respectively, the fibre length and orientation factors for

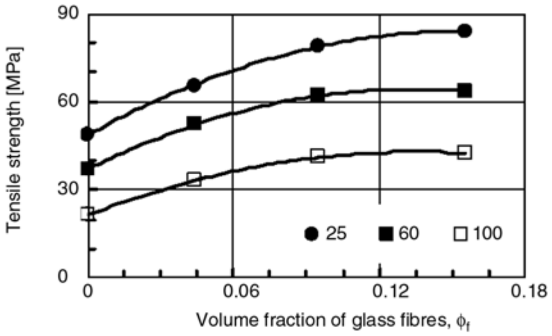

Figure 6. Tensile strength of ABS/GF composite, σ_{cf}, versus volume fraction of glass fibres, ϕ_f, at 25, 60 and 100°C

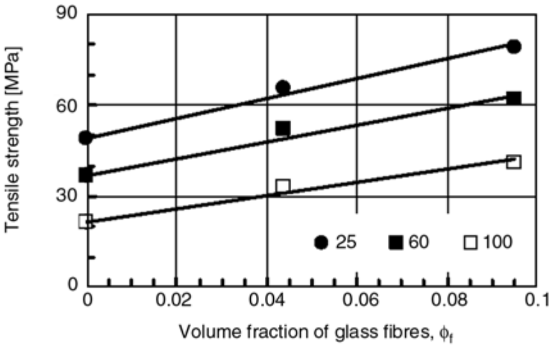

Figure 7. Tensile strength of ABS/GF composite, σ_{cf}, versus volume fraction of glass fibres, ϕ_f, at 25, 60 and 100°C for ϕ_f values in the range 0 to 10% v/v

Table 3. Fibre efficiency parameters for tensile modulus of ABS/GF composites

ϕ_f	λ_E			λ_1			λ_2		
	25°C	60°C	100°C	25°C	60°C	100°C	25°C	60°C	100°C
0.044	0.196	0.175	0.139	0.827	0.811	0.780	0.237	0.216	0178
0.095	0.196	0.175	0.139	0.811	0.793	0.760	0.242	0.221	0.183
0.155	0.196	0.175	0.139	0.802	0.783	0.748	0.244	0.223	0.186

Table 4. Fibre efficiency parameters for composite strength as a function of fibre volume fraction at 25, 60, and 100°C

ϕ_f	λ_σ			$\lambda_4 \approx \lambda_2$			λ_3		
	25°C	**60°C**	**100°C**	**25°C**	**60°C**	**100°C**	**25°C**	**60°C**	**100°C**
0.044	0.153	0.127	0.097	0.237	0.216	0178	0.646	0.588	0.545
0.095	0.153	0.127	0.097	0.242	0.221	0.183	0.632	0.575	0.530
0.155	0.153	0.127	0.097	0.244	0.223	0.186	0.627	0.570	0.522

tensile strength, which take into account fibre length variation and misalignment.

Equation (10) can alternatively be written in the form of Equation (11):

$$\sigma_{cf} = \sigma_m + (\lambda_\sigma \sigma_f - \sigma_m)\phi_f \qquad (11)$$

where $\lambda_\sigma = \lambda_3\lambda_4$ is the overall efficiency factor for tensile strength whose value at any given temperature can be determined from the slope of the line σ_{cf} versus ϕ_f in Figure 7. The effect of temperature on λ_σ is also shown in Figure 3 for comparative purposes where it can be seen that λ_σ is lower than λ_E and decreases likewise with increasing temperature. The linear dependence between λ_σ and temperature as shown in Figure 3 can be expressed by Equation (12):

$$\lambda_\sigma = 0.172 - 7.52 \cdot 10^{-4}\, T \qquad (12)$$

Assuming $\lambda_4 \approx \lambda_2$, values of λ_3 for composite strength was evaluated as a function of temperature ($\lambda 3 = \lambda_\sigma/\lambda_2$). It can be seen from Table 4, that λ_3 for composite strength like λ_1 for composite modulus decreases with increasing temperature. It is also notable that λ_4 is consistently lower than λ_1 thus indicating that tensile strength is more affected by the shortness of the fibres than tensile modulus.

Using the values λ_3 given in Table 4, the critical fibre lengths, L_c was calculated for each composite as a function of temperature using the Kelly-Tyson relationship given by Equation (13) [14]:

$$L_c = \frac{L_f}{2\lambda_3} \qquad (13)$$

Results obtained from this analysis are presented in Table 5 where it can be seen that L_c increases with increasing temperature but decreases with increasing ϕ_f mainly due to the reduction in the average length of the fibre, L_f, with increasing ϕ_f.

Table 5. Fibre critical length as a function of fibre volume fraction at 25, 60 and 100°C

ϕ_f	L_c [µm]		
	25°C	**60°C**	**100°C**
0.044	426	468	505
0.095	340	374	406
0.155	287	316	345

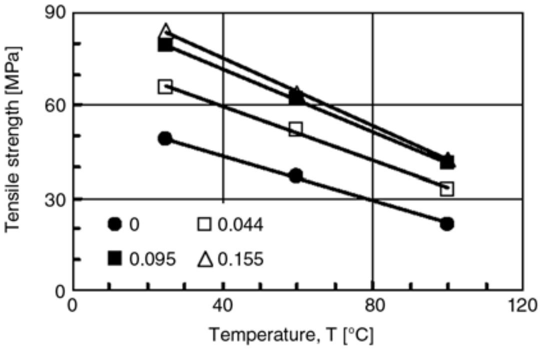

Figure 8. Tensile strength of ABS/GF composite, σ_{cf}, versus temperature, T, for fibre volume fractions, ϕ_f, of 0, 0.044, 0.095 and 0.155

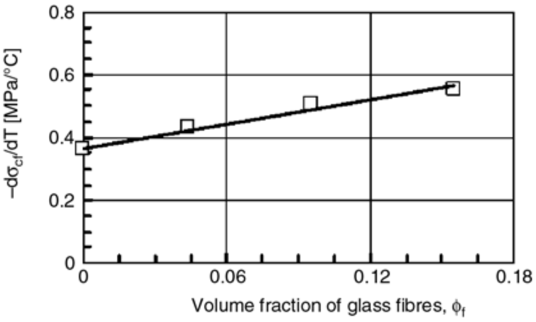

Figure 9. Effect of ϕ_f on the slope of the line, σ_{cf}, versus temperature in Figure 8

The effect of temperature on σ_{cf} is more explicitly shown in Figure 8. As can be seen, for a fixed ϕ_f, tensile strength of the composite, σ_{cf}, decreases linearly with increasing temperature. As illustrated in Figure 9, when slope of the lines in Figure 8 (i.e. $d\sigma_{cf}/dT$) are plotted versus ϕ_f, one obtains a linear dependence which can be reasonably expressed by Equation (14):

$$\frac{d\sigma_{cf}}{dT} = -(3.64 + 1.305\phi_f) \qquad (14)$$

Comparing Equation (5) and Equation (14) reveals that for the same volume fraction of fibres, composite strength is more affected by the change in temperature than composite modulus.

3.2. ABS/GB composites

The incorporation of glass beads into ABS reduced the tensile strength, but increased the tensile modulus, of the ABS matrix. Close examination of the load-extension curves once again indicated that whilst deformation of the composites was linear at low stresses, it was nonlinear at higher stresses. This observation suggested that interfacial microfailure also occurred around the glass bead particles during loading of the ABS/GB composites.

The effect of the volume fraction of glass beads, ϕ_b, on tensile modulus of ABS/GB composites, E_{cb}, at 25, 60 and 100°C is shown in Figure 10. It can be observed that E_{cb} increases with increasing ϕ_b in a linear manner. The linear dependence between E_{cb} and ϕ_b follows the Einstein [15] relationship given by Equation (15):

$$E_{cb} = E_m(1 + k_E\phi_b) \tag{15}$$

where E_m is modulus of the matrix and k_E is the Einstein coefficient having a value of 2.5 for spherical shaped fillers. The slope of the linear regression lines in Figure 10 suggests k_E values of 2.55, 2.38 and 2.31 at 25, 60 and 100°C, respectively for the ABS/GB system.

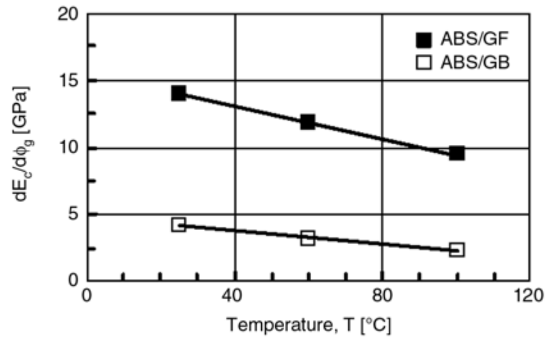

Figure 11. Effect of temperature on the slope of the lines in Figures 2 and 10

It is worth noting that at any given temperature as shown in Figure 11, gain in modulus due to addition of short glass fibres is much greater than that due to addition of glass beads. Also, the rate at which slope of the lines in Figures 2 and 10 changes with temperature, is a linear and decreasing function of temperature. The linear dependence for both composite systems can be expressed by Equations (16) and (17);

$$\frac{dE_{cf}}{d\phi_f} = 15.47 - 0.061T \tag{16}$$

$$\frac{dE_{cb}}{d\phi_b} = 4.711 - 0.024T \tag{17}$$

The above equations reveal that at any given temperature, tensile modulus of the ABS/GF composite is always greater than that of ABS/GB counterpart. Also, modulus of the composite material is more affected by the change in volume fraction of glass fibres than that of glass beads.

The effect of temperature on tensile modulus of ABS/GB composites, E_{cb}, is more explicitly shown in Figure 12 where it can be seen that E_{cb} decreases linearly with increasing temperature. It can be seen also that the rate of decrease as given by the slope of the lines in Figure 12 (i.e. dE_{cb}/dT) depends on the volume fraction of glass beads in the composite. As shown in Figure 13, when dE_{cb}/dT values are plotted against ϕ_b, a linear dependence is obtained

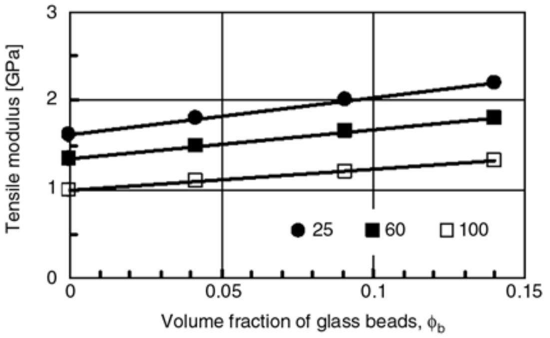

Figure 10. Tensile modulus of ABS/GB composite, E_{cb}, versus volume fraction of glass beads, ϕ_b, at 25, 60 and 100°C

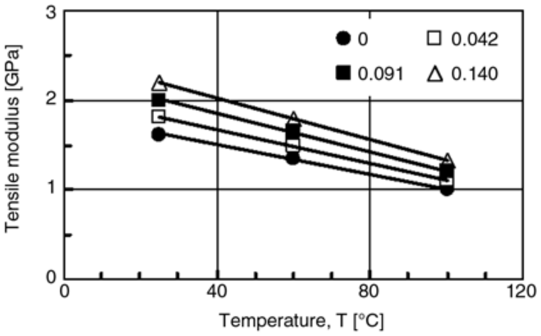

Figure 12. Tensile modulus of ABS/GB composite, E_{cb}, versus temperature, T, for glass bead volume fractions, ϕ_b, of 0, 0.042, 0.091 and 0.140

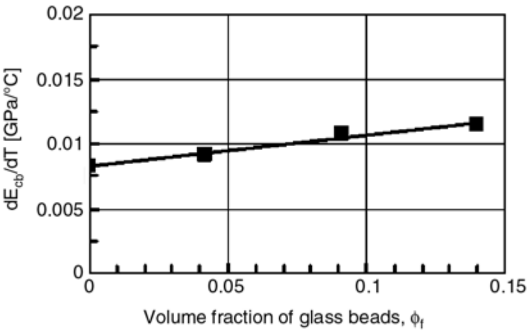

Figure 13. Effect of ϕ_b on the slope of the line, σ_{cb}, versus temperature in Figure 11

which can be reasonably expressed by Equation (18):

$$\frac{\mathrm{d}E_{cb}}{\mathrm{d}T} = -(0.0083 + 0.024\phi_b) \qquad (18)$$

The effect of ϕ_b on tensile strength of ABS/GB composites, σ_{cb}, at 25, 60 and 100°C is shown in Figure 14. As can be seen, σ_{cb} decreases linearly with increasing ϕ_b, over the entire temperature range studied here. It is worth noting that temperature has no significant influence upon the slope of the lines in Figure 14.

The linear dependence between σ_{cb} and ϕ_b as depicted in Figure 14 follows Piggott and Leidner [16] relationship given by Equation (19):

$$\sigma_{cb} = K\sigma_m - b\phi_b \qquad (19)$$

where K is a stress concentration factor and b is a constant whose value depends upon particle-matrix adhesion. Fitting the best regression lines to the data in Figure 14 gives K values of near unity (0.99) and b values in the range 32.48 to 34.01.

The effect of temperature on tensile strength of ABS/GB composites σ_{cb}, is more explicitly shown in Figure 15. It can be seen that ϕ_b has no significant effect upon the slope of the lines in Figure 15, thus indicating that the rate of change of σ_{cb} with temperature is independent of the glass bead concentration. Results suggest the rate of change follows Equation (20):

$$\frac{\mathrm{d}\sigma_{cb}}{\mathrm{d}T} = -0.364 \qquad (20)$$

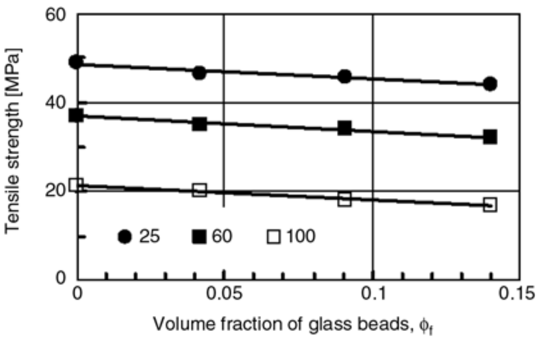

Figure 14. Tensile strength of ABS/GB composite, σ_{cb}, versus volume fraction of glass beads, ϕ_b, at 25, 60 and 100°C

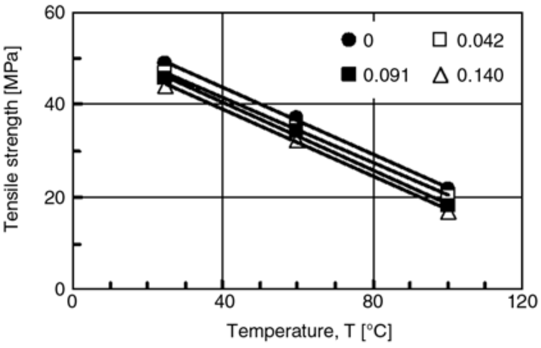

Figure 15. Tensile strength of ABS/GB composite, σ_{cb}, versus temperature, T, for glass bead volume fractions, ϕ_b, of 0, 0.042, 0.091 and 0.140

3.3. ABS/GF/GB hybrids

The effect of hybridisation on tensile modulus and strength was studied here in terms of hybrid ratio, χ_f, is defined by Equation (21):

$$\chi_f = \frac{\phi_f}{\phi_g} \qquad (21)$$

where ϕ_f is the volume fraction of the fibres and ϕ_g is the total volume fraction of glass, in the hybrid.

Figure 16 show the effect of χ_f on tensile modulus of ABS/GF/GB hybrids, E_h, at 25, 60 and 100°C for total glass concentration values of 10, 20 and 30% w/w, respectively. It can be seen that E_h increases with increasing χ_f in a linear manner. Results also reveal that at a fixed temperature, the effect of increasing ϕ_g is an upwards shift in the modulus values coupled with an increase in the slope of the lines E_h versus χ_f. The linearity of E_h with χ_f as depicted in Figure 16a–16c suggests hybrid tensile modulus conforms to the rule-of-mixtures given by Equation (22):

$$E_{h=}E_{cf}\chi_f + E_{cb}(1-\chi_f) \qquad (22)$$

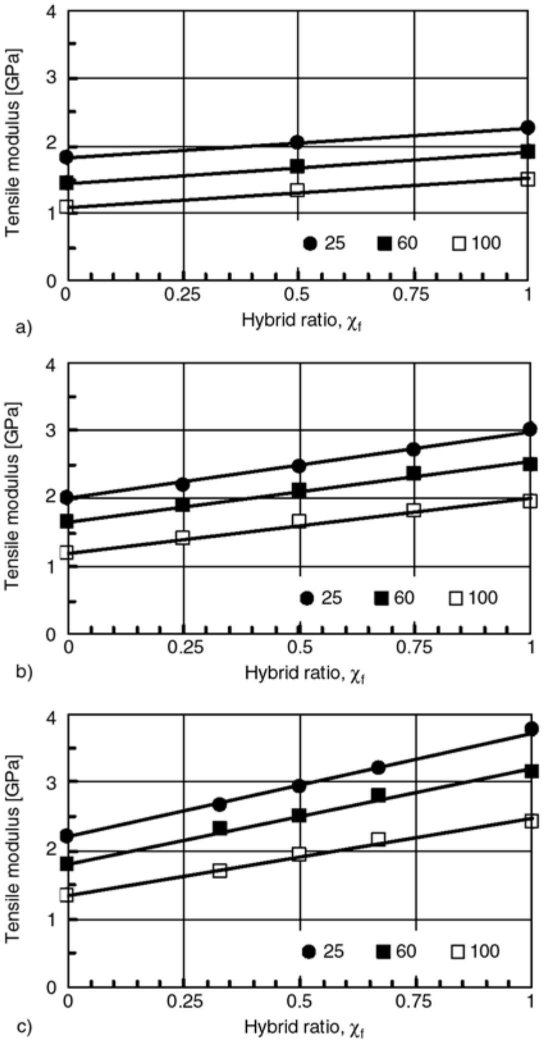

Figure 16. Tensile modulus of ABS/GF/GB hybrids, E_h, versus hybrid ratio, χ_f, at 25, 60 and 100°C for total glass concentration values of; (a) 10%, (b) 20% and (c) 30% by weight

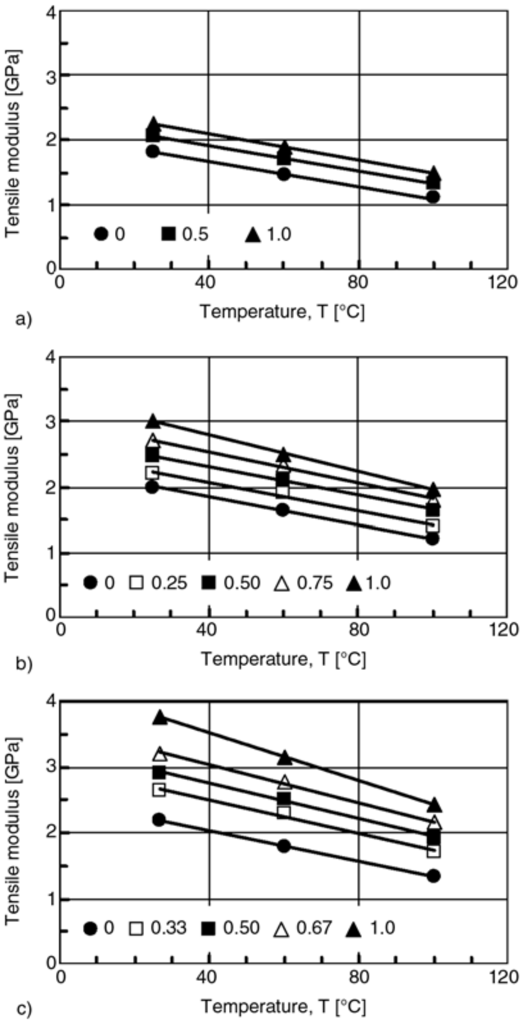

Figure 17. Tensile modulus of ABS/GF/GB hybrid, E_h, versus temperature, T, for various hybrid ratios, χ_f, and the total glass concentration values of; (a) 10%, (b) 20% and (c) 30% by weight

where E_{cf} and E_{cb} are the modulus values of ABS/GF and ABS/GB composites respectively, as defined by Equations (2) and (15). The lines fitted through the data in Figure 16 are according to Equation (22) where it can be seen that rule-of-mixtures for hybrids describes the data extremely well.

The effect of temperature on tensile modulus of ABS/GF/GB hybrids is shown in Figure 17 where it can be seen that E_h decreases with increasing temperature. However, the rate at which E_h decreases with temperature appears to be more affected by the total concentration of the glass in the hybrid than by the hybrid ratio, χ_f. The effect of increasing, χ_f, is simply an upward shift in E_h values. It is also evident that χ_f has no significant effect upon the slope of the lines in Figure 17, particularly at low glass concentration values.

The effect of χ_f on tensile strength of ABS/GF/GB hybrids, σ_h, at 25, 60 and 100°C for total glass content values of 10, 20 and 30% w/w is shown in Figure 18. Results show that σ_h increases with increasing χ_f in a linear manner thus indicating that the hybrid tensile strength like tensile modulus follows rule-of-mixtures given by Equation (23):

$$\sigma_h = \sigma_{cf}\chi_f + \sigma_{cb}(1-\chi_f) \qquad (23)$$

where σ_{cf} and σ_{cb} are the tensile strengths of ABS/GF and ABS/GB composites respectively, as defined by Equations (9) and (19). The rate at which σ_h increases with increasing χ_f (i.e., $d\sigma_h/d\chi_f$) is shown in Figure 19 as a function of temperature

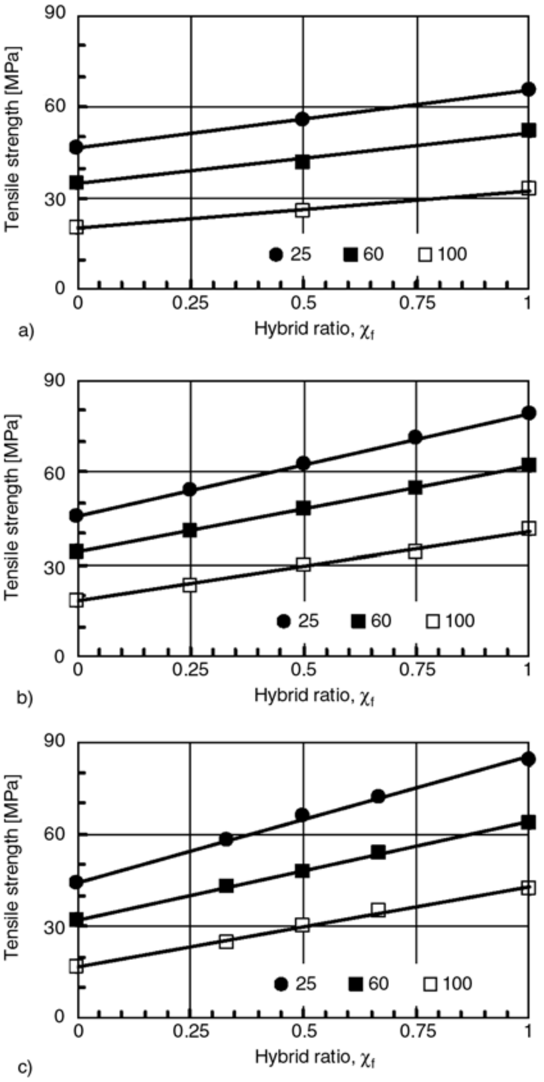

Figure 18. Tensile strength of ABS/GF/GB hybrids, σ_h, versus hybrid ratio, χ_f, at 25, 60 and 100°C for the total glass concentration values of; (a) 10%, (b) 20% and (c) 30% by weight

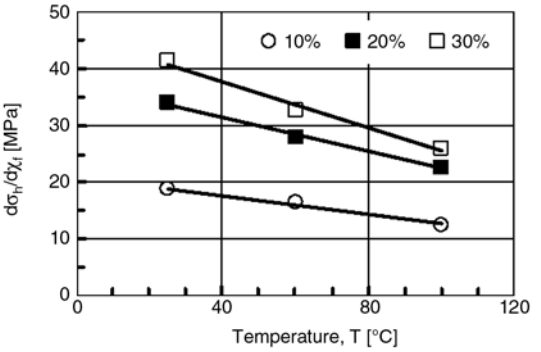

Figure 19. Effect of temperature on the slope of the line σ_h versus χ_f for total glass concentration values of 10, 20 and 30% wt

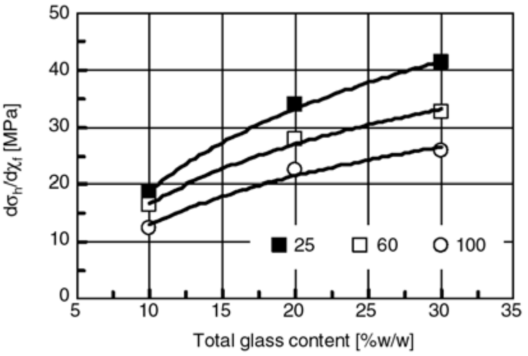

Figure 20. Effect of glass content on the slope of the line σ_h versus χ_f at 25, 60 and 100°C

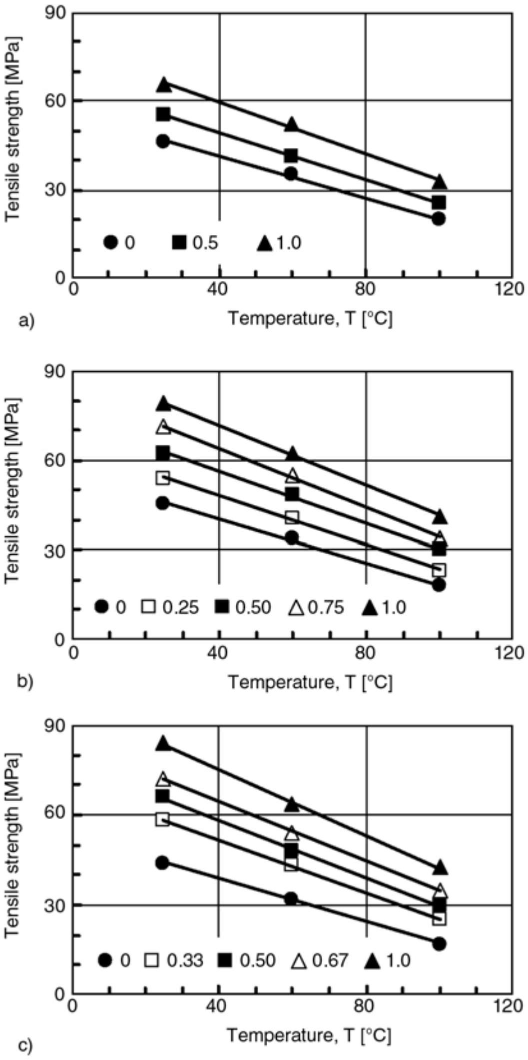

Figure 21. Tensile strength of ABS/GF/GB hybrid, σ_h, versus temperature, T, for various hybrid ratios, χ_f, and total glass concentration values of; (a) 10%, (b) 20% and (c) 30% by weight

for the total glass weight percentage values of 10, 20 and 30%. Results show that $d\sigma_h/d\chi_f$ decreases linearly with increasing temperature. However, as shown in Figure 20, the effect of temperature becomes more significant as weight percentage of the total glass in the hybrid is increased.

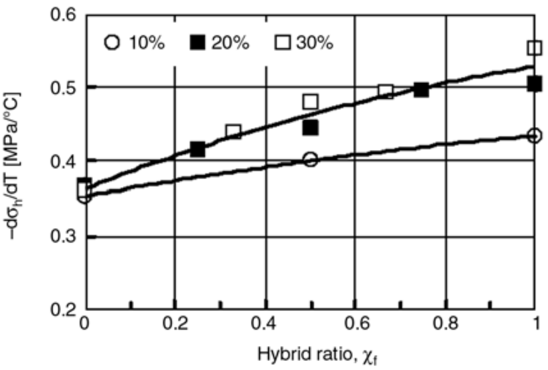

Figure 22. Effect of hybrid ratio, χ_f, on the slope of the lines σ_h versus temperature, T, in Figure 21 for total glass concentration values of; (a) 10%, (b) 20% and (c) 30% by weight

The effect of temperature on σ_h is shown more explicitly in Figure 21. Results show that σ_h decreases with increasing temperature in a linear manner. The rate at which σ_h decreases with increasing temperature (i.e. $d\sigma_h/dT$) as a function of hybrid ratio, χ_f, is shown in Figure 22 where it can be seen $d\sigma_h/dT$ increases with increasing χ_f and the total glass content in the hybrid. However, as illustrated in Figure 22, when the glass content in the hybrid is high, variation of $d\sigma_h/dT$ with χ_f becomes almost independent of the glass content.

4. Conclusions

A positive and negative hybrid effect in hybrid composites is defined as positive or negative deviation of a certain mechanical property from the rule-of-mixtures. It was found;

(i) Hybrid tensile strength, σ_h, and modulus, E_h, both increase with increasing the hybrid ratio of the glass fibre, χ_f in a linear manner. The variation of E_h and σ_h with χ_f obeys rule-of-mixtures.

(ii) Hybrid tensile strength, σ_h, and modulus, E_h, both increase with increasing the total concentration of the glass in the hybrid.

(iii) Hybrid tensile strength and modulus both decrease with increasing temperature in a linear manner.

References

[1] Hashemi S., Gilbride M. T., Hodgkinson J. M.: Mechanical property relationships in glass-filled polyoxymethylene. Journal of Materials Science, **31**, 5017–5025 (1996).

[2] Nabi Z. U., Hashemi S.: Influence of short glass fibres and weldlines on the mechanical properties of injection-moulded acrylonitrile-styrene-acrylate copolymer. Journal of Materials Science, **33**, 2985–3000 (1998).

[3] Hashemi S.: Influence of temperature on weldline strength of injection moulded short glass fibre styrene maleic anhydride polymer composites. Journal of Plastics, Rubber and Composites, **31**, 318–324 (2002).

[4] Hashemi S.: Thermal effects on weld and unweld tensile properties of injection moulded short glass fibre reinforced ABS composites. Express Polymer Letters, **1**, 688–697 (2007).

[5] Necar M., Irfan-ul-Haq M., Khan Z.: Temperature and weld-line effects on mechanical properties of CPVC. Journal of Materials Processing Technology, **142**, 247–255 (2003).

[6] Fu S-Y., Lauke B., Mäder E., Yue C-Y., Hu X.: Tensile properties of short-glass-fiber- and short-carbon-fiber-reinforced polypropylene composites. Composites, Part A: Applied Science and Manufacturing, **31**, 1117–1125 (2000).

[7] Fisa B.: Mechanical degradation of glass fibres during compounding with polypropylene. Polymer Composites, **6**, 232–241 (1985).

[8] Thomason J. L.: Micromechanical parameters from macromechanical measurements on glass reinforced polypropylene. Composites Science and Technology, **62**, 1455–1468 (2002).

[9] Thomason J. L.: Micromechanical parameters from macromechanical measurements on glass reinforced polyamide 6,6. Composites Science and Technology, **61**, 2007–2016 (2001).

[10] Yilmazer U.: Tensile, flexural and impact properties of a thermoplastic matrix reinforced by glass fiber and glass bead hybrids. Composites Science and Technology, **44**, 119–125 (1992).

[11] Hashemi S., Elmes P., Sandford S.: Hybrid effects on mechanical properties of polyoxymethylene. Polymer Engineering and Science, **37**, 45–58 (1997).

[12] Phillips L. N.: The hybrid effect – Does it exist? Composites, **7**, 7–8 (1976).

[13] Cox H. L.: The elasticity of strength of paper and other fibrous materials. British Journal of Applied Physics, **3**, 72–79 (1952).

[14] Kelly A., Tyson W. R.: Tensile properties of fibre-reinforced metals: Copper/tungsten and copper/molybdenum. Journal Mechanics Physics of Solids, **13**, 329–350 (1965).

[15] Einstein A.: Eine neue Bestimmung der Moleküldimensionen. Annalen der Physik, **19**, 289–306 (1906).

[16] Leidner J., Woodhams R. T.: The strength of polymeric composites containing spherical fillers. Journal of Applied Polymer Science, **18**, 1639–1654 (1974).

eXPRESS Polymer Letters Vol.2, No.7 (2008) 485–493
Available online at www.expresspolymlett.com
DOI: 10.3144/expresspolymlett.2008.58

Effects of nanofiller morphology and aspect ratio on the rheo-mechanical properties of polyimide nanocomposites

V. E. Yudin[1], *J. U. Otaigbe*[2*], *V. M. Svetlichnyi*[1], *E. N. Korytkova*[3], *O. V. Almjasheva*[3], *V. V. Gusarov*[3]

[1]Institute of Macromolecular Compounds, Russian Academy of Science, St.Petersburg, RUSSIA
[2]School of Polymers and High Performance Materials, The University of Southern Mississippi, Hattiesburg, MS 39406, USA
[3]Institute of Silicate Chemistry, Russian Academy of Sciences, St.Petersburg, RUSSIA

Received 19 March 2008; accepted in revised form 2 May 2008

Abstract. New polyimide nanocomposites containing organically modified montmorillonite (MMT), synthetic silicate (chrysotile) nanotubes (SNT), and zirconium dioxide (ZrO_2) were prepared to investigate the influence of the nanoparticle morphology on the nanocomposite rheology and mechanical properties under selected conditions that the materials are likely to encounter during use. The efficiency of homogeneous dispersion of the nanoparticles in the polyimide matrix was studied by measuring the rheology of model oligoimides (OI) dispersions containing the desired amounts of the nanoparticles. The OI/nanoparticles dispersions showed significant increase in complex viscosity with increasing concentration of the nanoparticles that depended strongly on the nanoparticle morphology and aspect ratio. Polyimide nanocomposite films (PI-PM) prepared from the poly(amic acid) of poly(pyromellitic dianhydride-*co*-4,4′-oxydianiline) (PM) filled with the desired concentration of the nanoparticles showed an increase in tensile modulus with increasing nanoparticle concentration in the order MMT>SNT>ZrO_2. In contrast to the PI-PM/MMT films, the PI-PM films filled with 10 vol% of SNT and ZrO_2 showed higher sample failure strains, suggesting that the SNT and ZrO_2 may be more effective in improving the ductility of the polyimide nanocomposites for applications where the relatively brittle polyimide/MMT nanocomposites films are not useable.

Keywords: *nanocomposites, polyimide, ceramic nanotubes and nanoparticles, rheology, mechanical properties*

1. Introduction

Organic polymer nanocomposites containing small amounts of various inorganic nanoparticles where the size of the inorganic phase does not exceed one hundred nanometers offer a number of desirable characteristics in a number of applications [1]. It is worthy to note that optimal combinations of organic (polymer) and inorganic (nanofiller) can lead to functional polymer nanocomposites with new polymer structures and enhanced properties including thermal, mechanical, and electrical properties.

Nanocomposites are commonly based on polymer matrices reinforced with layered silicate nanofillers such as montmorillonite clay (MMT) with layer thickness of at least 1 nm [2, 3]. Polymer/MMT nanocomposites constitute a relatively new class of reinforced plastics prepared by uniformly dispersing MMT nanoparticles in a polymer matrix. Such nanocomposites have great scientific and practical importance due to their high mechanical and barrier properties, as well as, their fire resistance [4]. But MMT nanoparticles are well known to be a mixture of several natural compounds with nonuniform

---

[*]Corresponding author, e-mail: Joshua.Otaigbe@usm.edu

composition and particle size. For example, MMT minerals from different deposits might differ considerably in composition. This variation in composition of MMT significantly complicates the task of making functional nanocomposites with prescribed properties for targeted applications. Therefore, there is a need to develop synthetic nanofillers with prescribed particle composition, shape and size for use as fillers in polymer nanocomposites with well defined properties.

In this area, synthetic nano-dimensional silicates may provide a number of opportunities in polymer nanocomposites that is relatively little studied and poorly understood relative to the well studied polymer nanocomposites filled with natural layered MMTs [5–9]. In contrast to the commonly used layered MMT compounds, it is envisaged that use of nanoparticles with different morphology (e.g., nanotubes and nanoparticles of isometric shape) might provide additional benefits in polymer nanocomposites not possible with MMT. Suitable techniques for hydrothermal synthesis of silicate nanotubes and particles of isometric form (e.g., zirconium dioxide) that gives the possibility to control the resulting nanoparticle's structure by varying the mode of hydrothermal synthesis has been reported [7–9].

Polyimide (PI)-based nanocomposites are of special interest because of the well known excellent heat resistance, chemical stability, and superior electric properties of polyimides [10]. As previously reported, PI/MMT nanocomposites can exhibit increased modulus and strength, high heat distortion temperature, decreased thermal expansion coefficient, reduced gas permeability, and increased solvent resistance compared to the pristine polymer [2, 3]. However, there are a number of significant limitations in the processing of PI/MMT nanocomposites. These limitations include (but not limited to) the relatively low thermal stability of the organically modified MMT under typical processing temperatures compared to that of the relatively elevated processing temperatures that are needed for curing PIs or melt blending PIs with nanoparticles. It is well known that it is very difficult to find thermally stable modifier to improve clay compatibility with high temperature polymers such as polyimides that must be processed at elevated temperatures as already mentioned.

The work presented herein is focused on investigating the feasibility of using as nanofillers for polyimide matrices new silicate type nanotubes (SNT) and zirconium dioxide (ZrO_2) nanoparticles (with different morphology as compared to layered MMT platelets) that were custom synthesized specifically for nanocomposite application [7, 8]. The rheology and mechanical behavior of the PI nanocomposites as a function of the nanofiller shapes (i.e., platelets, nanotubes and isometric form) will be presented and discussed to provide a starting point for further experiments that will improve our understanding of optimal methods of incorporating nanoparticles with varying shapes and sizes into polyimide matrices and of the effects of the nanoparticles morphology on the structure and properties of polyimide nanocomposites in general.

2. Experimental

2.1. Silicate nanotubes

Silicate nanotubes (SNT) with a chrysotile type structure of $Mg_3Si_2O_5(OH)_4$ were synthesized using a hydrothermal method that is facilitated by high pressure autoclaves as described elsewhere [7]. The SNT density is 2.5 g/cm^3. TEM showed that the SNT particles have average outer diame-

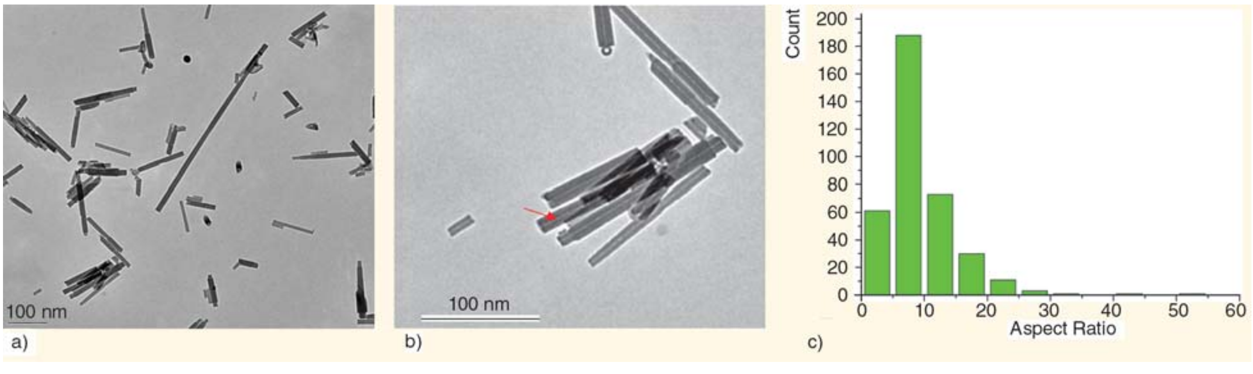

Figure 1. TEM photomicrographs of the SNT particles at low (a) and high (b) magnifications; (c) frequency count of aspect ratio (length/diameter) of the SNT particles

ter = 15 nm and average interior diameter = 3 nm as illustrated in Figures 1a and 1b. The length of the SNT ranges from 50 to 600 nm and its average aspect ratio is 10 (Figure 1c).

2.2. Zirconium dioxide particles

Zirconium dioxide (ZrO_2) particles were synthesized using a hydrothermal method [8]. These particles have spherical shapes as indicated in Figure 2. The average diameter of these particles is 20 nm. The density of the particles is ~6 g/cm^3.

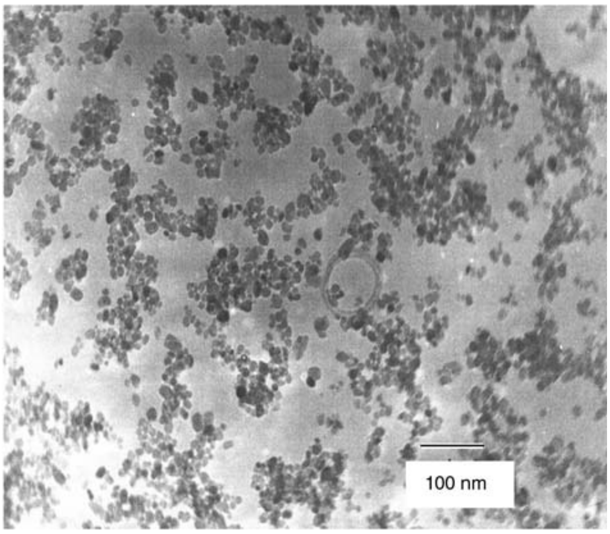

Figure 2. TEM photomicrograph of ZrO_2 type particles

2.3. Treatment of SNT and ZrO_2 with silane coupling agent

To improve compatibility of the nanoparticles with polyimide matrix, the SNT and ZrO_2 particles were treated with *m*-aminophenyltrimethoxysilane (Gelest. Inc.) following the procedure described in [11]. The amount of the silane needed to obtain minimum uniform multilayer coverage was estimated from the known values of the specific wetting surface of the silane (i.e., ~350 m^2/g) and the surface area of the filler (i.e., ~100 m^2/g) and found to be about 3.5 times less than the amount of filler used. Specifically, one gram of nanoparticles (SNT or ZrO_2) was dispersed in 50 ml of ethanol with the aid of an ultrasonic mixer (40 kHz, average sonic power: 45 W) for 1 hour. 0.3 ml of the silane was added to the sonicated suspension followed by additional sonication for 10 min. The resulting suspension of the nanoparticles was centrifuged and the supernatant ethanol was decanted to yield the silane-treated nanoparticles of this study. The silane-treated nanoparticles were rinsed twice with ethanol followed by curing of the silane layer and dried until constant weight was achieved in a vacuum oven maintained at 60°C for 5 hr.

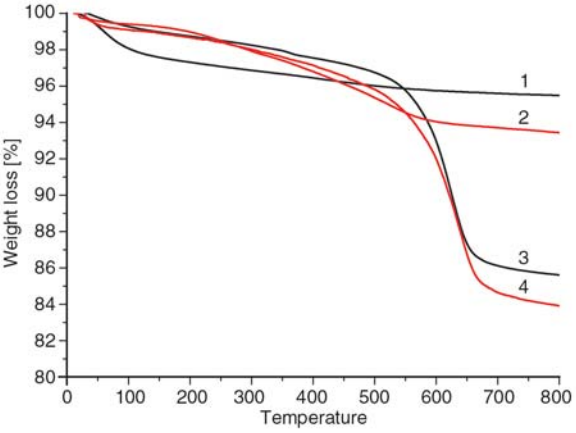

Figure 3. TGA scans of nanoparticles: 1 – pure ZrO_2 nanoparticles; 2 – ZrO_2 treated with silane coupling agent; 3 – pure SNT type particles; 4 – SNT treated with silane coupling agent

TGA was used to confirm the silane treatment of the SNT and ZrO_2 as depicted in Figure 3. This figure shows degradation temperature of the organosilane compound at temperatures greater than 300°C, making the silane-treated particles suitable for processing/mixing with polyimide matrices that must be cured at temperatures ranging from 200 to 300°C. The weight loss of pure SNT particles at 550–650°C (Figure 3) is ascribed to evaporation of water incorporated into the crystal structure of chrysotile.

2.4. Organic treatment of MMT

Natural montmorillonite clay Na-MMT [Cloisite®Na$^+$, cation exchange capacity (CEC): 92.6 meq/100 g] was obtained from Southern Clay Products, Inc. The density of the particles is ~2.8 g/cm^3. Hydrochloric acid (concentration: 36.5%) and 4,4′*bis*(4″-aminophenoxy) diphenylsulfone (BAPS) were obtained from Fisher Chemical and Wakayama Seika Kogyo Co., Ltd. in Japan, respectively.

The Na-MMT was organically modified with BAPS ammonium salts. A mixture of BAPS and hydrochloric acid in deionized water (DI water) was prepared. An aqueous dispersion of Na-MMT that was agitated for 3 hours was added to this previously prepared mixture just mentioned. The resulting mixture was agitated simultaneously with a mechanical stirrer and ultrasound at 60°C for 6 hours, and the mixture was then left at room temperature for 12 hours. The resulting white precipitate was filtered and washed repeatedly with DI water at 60°C to remove superfluous ammonium salts and Cl^- ion. Removal of Cl^- ion was monitored by titration with addition of 0.1N $AgNO_3$ into the filtered liquid (based on whether a white precipitation of AgCl appeared or not). The filtered cake was freeze-dried for 12–18 hours to yield BAPS-modified clay (MMT-BAPS) used in this study.

2.5. Polyimide matrices

Poly(amic acid) (PAA) of poly(pyromellitic dianhydride-*co*-4,4′-oxydianiline) (PM) was supplied by Sigma-Aldrich. The PAA-PM is a 15.0–16.0 wt% solution in N-methyl-2-pyrrolidone (NMP) with a viscosity of 50–70 poise. PI type films (30–40 μm thick) were prepared from the PAA-PM by casting on soda lime glass plates and subsequent curing in an oven under air atmosphere. Imidization was achieved by placing the films in an air oven for curing at 100°C/1 hr, 200°C/1 hr, 300°C/1 hr, and 350°C/30 min. Subsequently, the cast films were removed after complete imidization from the glass plates by soaking in water. The density of the PI type film prepared from PAA-PM is 1.42 g/cm^3, and the film is hereinafter referred to as PI-PM.

The oligoimide (OI) based on 1,3-*bis*(3′,4,-dicarboxyphenoxy)benzene and 4,4′*bis*(4″-aminophenoxy)diphenylsulfone and endcapped with phthalic anhydride was synthesized following the procedure previously described in [12]. Note that the oligoimide with the chemical structure shown in Figure 4. was used as a model material for evaluating the rheological behavior of polyimide matrix filled with the nanoparticles.

The number and weight average molecular weights (M_n = 3609 g/mole and M_w = 11553 g/mole respectively) were obtained from gel permeation chromatography following standard procedures.

2.6. Processing of polyimide nanocomposites

The PI-PM nanocomposite films with different concentrations of nanoparticles (i.e., SNT, ZrO_2 or MMT-BAPS) were prepared by adding the desired amount of the nanoparticles to NMP. The resulting suspension of particles in NMP was homogenized with the aid of an ultrasonic mixer (40 kHz, average sonic power: 45 W) for 1 hour. The sonicated suspension was transferred into a three neck round bottom flask equipped with a mechanical stirrer, a nitrogen gas inlet, and a drying tube outlet filled with calcium sulfate. After stirring the nanoparticle solution for 10 min, the PAA-PM was added to the nanoparticle suspension and the stirring of the mixture was continued for an additional 60 min until a constant viscosity was obtained. The solid content of the nanoparticles/PAA-PM was 10 wt% in NMP. Thin (30–40 μm thick) PI-PM nanocomposite films were prepared with varying nanoparticles weight concentrations (wt) from the nanoparticles/PAA-PM solution as already described above for the pure (unfilled) PI-PM films. Using the material densities (1.42 g/cm^3 for PI-PM, 2.5 g/cm^3 for SNT, 6 g/m^3 for ZrO_2, and ~2 g/cm^3 for MMT-BAPS), the corresponding volume concentrations (vol) of nanoparticles in the polyimide nanocomposites were estimated using Equation (1):

$$vol = \frac{1}{1+\frac{\rho_1}{\rho_2}\cdot\left(\frac{1}{wt}\right)}\cdot 100 \qquad (1)$$

where ρ_1 is density of the particles and ρ_2 is density of the polymer matrix.

A simple solution mixing method was used to prepare a mixture of NMP solution of OI with nanoparticles (i.e., SNT, ZrO_2 or MMT-BAPS). Firstly, the nanoparticles were dispersed in NMP using an ultrasonic mixer (40 kHz, average sonic power: 45 W) for 1 hour. Various amounts of the nanoparticles were used to yield final OI/nanoparticles mixtures containing 3–20 wt% of the respective nanoparticles. Subsequently, NMP solution of OI (20 wt% OI concentration) was added to the modified nanoparticles/NMP dispersion, and the com-

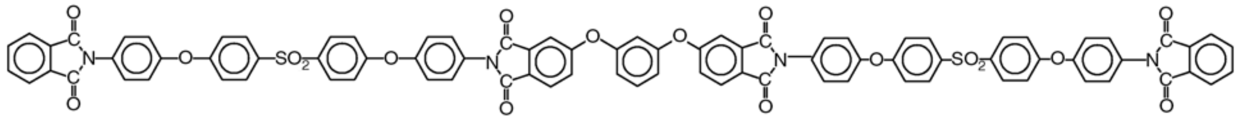

Figure 4. Structure of the oligoimide used to evaluate the rheological behavior

bined mixture was stirred with a magnetic stirrer for 5 hours followed by ultrasonic mixing of same for 1 hour. The resulting NMP dispersion of OI with the nanoparticles was poured on a Teflon®-coated metal substrate that was subsequently heated at 100°C for 1 hour, 200°C for 1 hour, and 280°C for 0.5 hour to completely remove NMP solvent as monitored by TGA. The Teflon® coating made it easy to collect the OI/nanoparticles blends in the form of powder. As described in the next section, these powdered samples were used to prepare test specimens for the rheology measurements described in the next section.

2.7. Measurements

A strain-controlled dynamic rheometer ARES® from TA Instruments was used to measure the dynamic and steady shear viscosity of the polymers in the cone and plate configuration following standard procedures. The diameter of the plate was 25 mm and the cone angle was 0.1 rad. Nitrogen was used as the heating gas for temperature control. The powdered samples were compacted into disks at room temperature using a compression molding machine. The disk was then subsequently placed between the plates of the rheometer that were preheated to the desired temperature.

Tensile stress-strain properties of the PI-PM based nanocomposite films were measured using a tensile testing machine (Alliance RT/10, MTS systems Co., Ltd.) following standard ASTM D882-95 method. A specimen gage length of 50 mm and width of 5 mm and a testing speed of 2 mm/min were used. Care was taken to ensure proper alignment of the specimen with the testing fixture. An abrasive paper was placed between the specimen and test fixture surface to prevent slippage. Ten replicate measurements were conducted for each sample and the average results of the ten specimens are reported in this article.

The XRD patterns of nanocomposites PI-PM/MMT-BAPS and OI/MMT-BAPS were recorded with an X-ray diffractometer (D/MAX Ultema III, Rigaku Co., Ltd.). The X-ray was generated with nickel-filtered CuK$_\alpha$ ($\lambda = 0.154$ nm) at 40 kV and 44 mA. The samples were scanned at 2θ angles ranging from 2 to 10° using a scanning rate of 10°/min at room temperature. An increase in the basal layer spacing of organically modified MMTs in the PI/MMT composites, which was determined from a shift in the (001) peak position, confirmed ion exchange or polymer intercalation between the silicate layers.

3. Results and discussion

3.1. Rheology of model Oligoimide Based Nanocomposites

To evaluate the feasibility of homogeneous dispersion of the nanoparticles in polyimide matrix, we used the rheology method that was previously reported to be an effective method for characterizing the exfoliation of clay nanoparticles in a variety of polymers [12, 13]. Homogenous dispersion of nanoparticles in the polymer should lead to a time-dependent rheological behavior (i.e., thixotropy) that is characteristic of formation of percolation type network at some concentration of the nanoparticles. Generally, it is possible to estimate this percolation threshold P_c theoretically [14] by using Equation (2) for a cylinder:

$$P_c = \frac{0{,}6}{r} \tag{2}$$

and Equation (3) for an ellipsoid:

$$P_c = \frac{1{,}27}{r} \tag{3}$$

where aspect ratio $r = L/d$, and L is the length of cylinder or diameter of ellipsoid and d is the diameter of cylinder or thickness of the ellipsoid. The preceding equations and the average aspect ratio of ~10 for SNT (Figure 1c) were used to estimate the percolation threshold (P_c) and the P_c (SNT) was found to be ~6 vol%. Assuming an average diameter (lateral dimension) of ~200 nm for the MMT particles [15] and a thickness of ~1 nm the percolation threshold for the MMT particles was estimated as P_c (MMT) = 0.64 vol%.

As previously reported for oligoimides melt blended with clay particles (MMT-15A, Southern Clay Products) [12], the application of strong shear flow field in a HAAKE MiniLab® Micro Compounder can lead to relatively good dispersion of MMT-15A particles in a polymer volume. In addition, the significant viscosity increase exhibited by the OI/MMT nanocomposites after application of

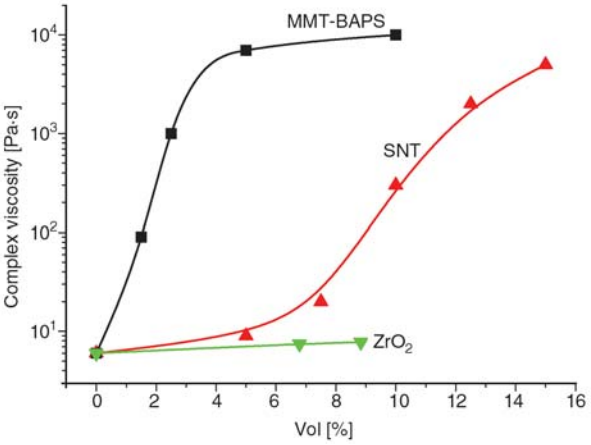

Figure 5. Dependence of complex viscosity on volume concentration of nanoparticles in oligoimide OI. Temperature $T = 260°C$, frequency $\omega = 1$ rad/s, strain $\varepsilon = 1\%$.

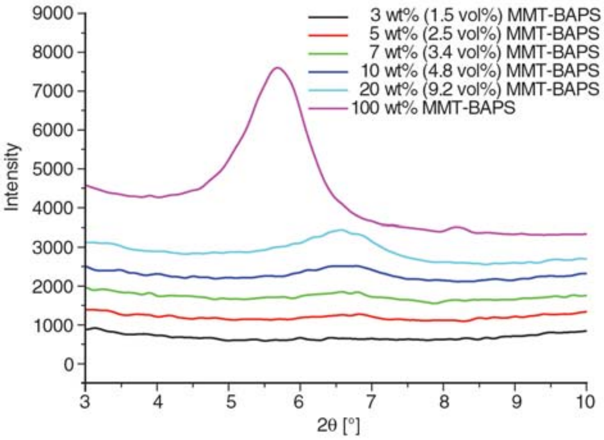

Figure 6. XRD patterns of oligoimide (OI) nanocomposites filled with MMT-BAPS particles. The weight and volume concentrations of the particles are indicated on the graph.

the strong shear flow fields may be attributed to the partial exfoliation of the organo-MMT particles and formation of the percolating (network) structure at ~10 wt% of MMT-15A particles in OI melt as previously reported [12, 13]. This prior work suggests that OI/MMT clay nanocomposites can be used as excellent model systems for investigating the process of exfoliation (or optimal dispersion) of the MMT-BAPS particles in PI reported in the present paper.

Figure 5 shows the dependence of complex viscosity (frequency $\omega = 1$ rad/s, strain $\varepsilon = 1\%$) on concentration of the nanofillers (i.e., MMT-BAPS, SNT and ZrO_2) for the present OI nanocomposites prepared as already described in the experimental section 2.6. The viscosities of the nanocomposites were estimated at 260°C, a temperature corresponding to the fluid state of the OIs. The figure shows significant increase (~3 decades) for the OI/MMT-BAPS and OI/SNT nanocomposites occurring at 2–3 vol% MMT-BAPS and 8–12 vol% SNT nanofiller concentrations, respectively. For the two types of nanocomposites just mentioned, the critical nanofiller concentrations corresponding to the dramatic rise in viscosity were found to be both higher than the percolation threshold values estimated theoretically as already described (i.e., P_c (MMT) = 0.64 vol% and P_c (SNT) = 6 vol%). This trend in the viscosity data is consistent with that previously reported in the literature for similar polymer nancomposites and has been attributed to different degrees of exfoliation of the nanofillers in the polymer matrix [2, 3, 12]. The X-ray data for OI/MMT-BAPS nanocomposites at different concentrations of particles (see Figure 6) provide indirect confirmation of this hypothesis because an increase in MMT-BAPS concentration leads to aggregation of the MMT platelets at concentrations > 3 vol%, that is clearly evident from appearance of a diffraction peak at around $2\theta = 6.3°$. It is worthy to note that this 2θ value is equivalent to MMT-BAPS interlayer spacing of 1.4 nm while the diffraction peak at $2\theta = 7.3°$ corresponding to an interlayer spacing of 1.2 nm (Figure 6).

The preceding results are consistent with our expectations of strong influence of the particle morphology and aspect ratio of the nanofillers (i.e., MMT platelets or SNT cylinders). For example, the relatively low aspect ratio SNT was found to exhibit a dramatic viscosity rise that is known to be consistent with formation of a percolation network structure at relatively higher concentrations than that exhibited by the relatively higher aspect ratio MMT (Figure 5).

As can be seen in Figure 5, the concentration dependence of viscosity for the OI/ZrO_2 nanocomposite was found to be consistent with that predicted by the following classical Thomas equation (4) [16]:

$$\eta = 1 + 2.5\phi + 0.05\phi^2 + A\exp(B\phi) \qquad (4)$$

where ϕ is volume fraction of particles; $A = 0.0273$ and $B = 16.6$. In this case, this relatively modest increase in viscosity with increasing ϕ (up to 9 vol% as depicted in Figure 5) is somewhat similar to that reported in the literature for polymers filled with spherical particles with various sizes [16]. The observed behavior of the OI/SNT and OI/MMT nanocomposites suggests that anisotropic particles such as MMT or SNT are more effective in inducing formation of percolating network structure (i.e., gelation) than spherical particles such as ZrO_2 used in this study [17].

3.2. Mechanical properties of PI-PM nanocomposite films

The mechanical properties (Young's modulus E_t, tensile strength σ_t and elongation at break ε_t) of the PI-PM based nanocomposite films are summarized in Table 1. Clearly, this table shows that incorporation of SNT and MMT-BAPS into polyimide matrix improves its modulus considerably. Figure 7 compares the nanofiller concentration dependencies of the relative modulus (i.e., modulus E_t divided by the modulus of the pure PI-PM matrix (E_0 = 2.8 GPa)) for the three types of nanocomposites studied. It is evident from this figure that the PI-PM/MMT-BAPS showed the largest increase in modulus with increasing nanofiller concentration. This finding is consistent with the nanofiller concentration dependencies of the viscosity of the nanocomposites already discussed (see Figure 5). As before, the large increase in modulus just mentioned is thought to be due to the relative high aspect ratios and enhanced dispersion of the MMT-BAPS nanofiller compared with that of the isometric ZrO_2 nanofillers. The results confirm our expectation that the morphology of the nanoparticles (platelets, tubes or isometric form) and especially their aspect ratios strongly influences the viscoelastic properties of the nanocomposites in both their solid and liquid states. Therefore, understanding the role of the nanofiller variables such as morphology, aspect ratio and composition on the properties of polymer nancomposites may lead to development of new materials with optimal properties for targeted application areas.

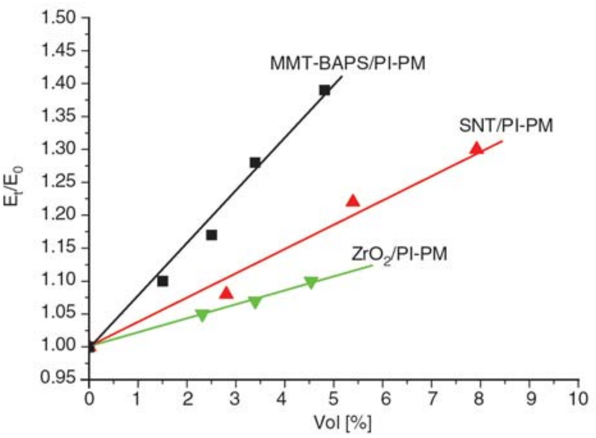

Figure 7. Dependence of tensile modulus E_t of nanocomposite films PI-PM on volume concentration of the nanoparticles (see Table 1, E_0 is the modulus of unfilled PI-PM film)

As shown in Table 1, the tensile strength and deformation-at-break of the PI-PM based nanocomposite films decreases slightly with increasing concentrations of the nanofiller used to an extent that depends on the specific characteristics of the nanofiller used. This decrease in tensile strength may be attributed to the less than optimum adhesion between the nanofillers and the matrix and the possible formation of an inhomogeneous network structure density in the nanocomposite like others have reported for other polymer nanocomposites [2, 3]. It is worthy to note that formation of an inhomogeneous network structure just mentioned is exacerbated by the strong rise in viscosity near the

Table 1. Properties of nanocomposite films based on PI-PM type polyimide matrix

Particles	Nanoparticles concentration [wt%]	Nanoparticles concentration [vol%]	Tensile modulus [GPa]	Tensile strength [MPa]	Deformation at break [%]
MMT-BAPS	0	0	2.85 ± 0.05	131 ± 3	30 ± 2
	3	1.5	3.13 ± 0.04	120 ± 2	22 ± 6
	5	2.5	3.34 ± 0.11	117 ± 5	16 ± 3
	7	3.4	3.65 ± 0.07	110 ± 4	13 ± 3
	10	4.8	3.96 ± 0.10	108 ± 6	5 ± 2
SNT	5	2.8	3.07 ± 0.07	123 ± 3	24 ± 2
	10	5.4	3.50 ± 0.10	97 ± 2	12 ± 3
	15	7.9	3.70 ± 0.10	86 ± 3	6 ± 2
ZrO_2	10	2.3	3.00 ± 0.05	105 ± 2	15 ± 2
	15	3.4	3.06 ± 0.07	95 ± 4	10 ± 5
	20	4.5	3.13 ± 0.10	90 ± 3	7 ± 3

percolation threshold as already mentioned, making it crucial to determine as in this study the optimal preparation conditions that may reduce or eliminate any potential micro-heterogeneity in the resultant nanocomposite films. Despite the reduction of the tensile strength caused by incorporation of the nanofillers in the polyimide nanocomposites, it is interesting to note that incorporation of relatively high concentrations of SNT and ZrO_2 (up to 10 vol%) does not lead to catastrophic decrease of elongation-at-break (ε_t) that is widely reported in the literature for a number of PI nanocomposites containing organoclay nanofillers [2, 3]. This last point suggests the possibility of using the present SNT and ZrO_2 to develop useful polyimide nanocomposites films with improved thermal and barrier properties, and adequate mechanical properties for a number of coating applications where the coating film flexibility is an important performance requirement. This important benefit offered by the SNT and ZrO_2 is believed to be due to the desirable intrinsic properties of these ceramic particles that can be prepared with prescribed properties for specific applications including polymer nanocomposites as already mentioned. This study may stimulate a better understanding of the effects of methods of incorporation of nanoparticles with varying shapes and sizes into polyimide matrices and the effects of the nanoparticles morphology on the structure and properties of polyimide nanocomposites, enhancing our ability to prepare useful polymer nanocomposites in general with improved properties for targeted applications where common polymer nanocomposite systems are not useable.

4. Conclusions and outlook

It can be concluded from the results of this study that simple rheometric methods can be reliably used to probe the influence of methods of incorporation of nanoparticles with varying shapes and sizes into polyimide matrices and the effects of the nanoparticles morphology on the quality of dispersion and properties of polyimide nanocomposites. By using model oligimides systems filled with the three types of nanoparticles studied (i.e., MMT-BAPS, SNT and ZrO_2), it was demonstrated that the critical concentration for gelation or formation of a percolating network structure that is characteristic of the huge rise in viscosity with increasing nanoparticles concentration strongly depends on the morphology and aspect ratio of the nanoparticles. The significant increase in viscosity (~3 decades) exhibited by the model oligoimides nanocomposites filled with MMT-BAPS, SNT or ZrO_2 nanofillers was observed at 2–3 vol% MMT-BAPS and 8–12 vol% SNT or ZrO_2 nanofiller concentrations, respectively.

On the other hand, the critical nanofiller volume concentrations corresponding to the dramatic rise in viscosity for the OI/MMT-BAPS and OI/SNT nanocomposites were found to be higher than the percolation threshold values (P_c) estimated theoretically (i.e., P_c (MMT) = 0.64 vol% and P_c (SNT) = 6 vol%). This disagreement between the experimental and theoretical estimations of P_c is thought to be due to agglomeration of the nanoparticles that was indirectly confirmed by XRD data for the OI/MMT nanocomposite.

In general, it is worthy to note that the SNT and ZrO_2 nanoparticles of this study can be used to develop useful polyimide nanocomposites films with adequate thermo-mechanical properties for a number of coating applications where the coating film flexibility and thermooxidative stability are important performance requirements. Overall, the results confirm our expectation that the morphology of the nanoparticles (platelets, tubes or isometric form) and especially their aspect ratios strongly influences the viscoelastic properties of the nanocomposites in both their solid and liquid states.

Acknowledgements

Financial support of this work by the U.S. National Science Foundation under contract grant numbers CBET 0317646 and CBET 0752150, and by the Russian Foundation of Basic Research under contract grant number 07-03-00846-a is gratefully acknowledged.

References

[1] Xanthos M.: Functional fillers for plastics. Wiley-VCH, Weinheim (2005).

[2] Sinha Ray S., Okamoto M.: Polymer/layered silicate nanocomposites: A review from preparation to processing. Progress in Polymer Science, **28**, 1539–1641 (2003).

[3] Zeng Q., Yu A., Lu G., Paul D.: Clay-based polymer nanocomposites: Research and commercial development. Journal of Nanoscience and Nanotechnology, **5**, 1574–1592 (2005).

[4] Kashiwagi T., Du F., Douglas J. F., Winey K. I., Harris R. H., Shields J. R.: Nanoparticle networks reduce the flammability of polymer nanocomposites. Nature Materials, **4**, 928–932 (2005).

[5] Falini G., Foresti E., Lesci G., Roveri N.: Structural and morphological characterization of synthetic chrysotile single crystals. Chemical Communication, **2002**, 1512–1513 (2002).

[6] Zhang Y., Lu S., Li Y., Dang Z., Xin J., Fu S., Li G., Guo R., Li L.: Novel silica tube/polyimide composite films with variable low dielectric constant. Advance Materials, **17**, 1056–1059 (2005).

[7] Korytkova E., Maslov A., Pivovarova L., Drozdova I., Gusarov V.: Formation of $Mg_3Si_2O_5(OH)_4$ nanotubes under hydrothermal conditions. Glass Physics and Chemistry, **30**, 51–55 (2004).

[8] Pozhidaeva O., Korytkova E., Romanov D., Gusarov V.: Formation of ZrO_2 nanocrystals in hydrothermal media of various chemical compositions. Russian Journal of General Chemistry, **72**, 849–853 (2002).

[9] Yudin V., Otaigbe J., Gladchenko S., Olson B., Nazarenko S., Korytkova E., Gusarov V.: New polyimide nanocomposites based on silicate type nanotubes: Dispersion, processing and properties. Polymer, **48**, 1306–1315 (2007).

[10] Bessonov M., Koton M., Kudryavtsev V., Laius L. A.: Polyimides-thermally stable polymers. Consultants Bureau, New York (1987).

[11] Gelest, Inc, Edited by B. Arkles, 2nd edition, 88–89 (1998).

[12] Yudin V., Divoux G., Otaigbe J., Svetlichnyi V.: Synthesis and rheological properties of oligoimide/montmorillonite nanocomposites. Polymer, **46**, 10866–10872 (2005).

[13] Zhong Y., Wang S-Q.: Exfoliation and yield behavior in nanodispersions of organically modified montmorillonite clay. Journal of Rheology, **47**, 483–495 (2003).

[14] Garboczi E., Snyder K., Douglas J., Thorpe M.: Geometrical percolation threshold of overlapping ellipsoids. Physical Review E, **52**, 819–828 (1995).

[15] Giannelis E., Krishnamoorti R., Manias E.: Polymer-silicate nanocomposites: Model systems for confined polymers and polymer brushes. Advances in Polymer Science, **138**, 107–120 (1999).

[16] Nielsen L.: Mechanical properties of polymers and composites. Marcel Dekker, New York (1994).

[17] Barnes H.: Thixotropy- A review. Journal of Non-Newtonian Fluid Mechanics, **70**, 1–33 (1997).

eXPRESS Polymer Letters Vol.2, No.7 (2008) 494–501
Available online at www.expresspolymlett.com
DOI: 10.3144/expresspolymlett.2008.59

Effect of polyhedral-oligomeric-sil-sesquioxanes on thermal and mechanical behavior of SC-15 epoxy

I. K. Jones[1], *Y. X. Zhou*[1*], *S. Jeelani*[1], *J. M. Mabry*[2]

[1]Tuskegee University's Center for Advanced Materials, Tuskegee, AL 36088, USA
[2]Air Force Research Laboratory, Edwards AFB, CA 93524, USA

Received 4 March 2008; accepted in revised form 10 May 2008

Abstract. In this study, thermal and mechanical properties of nanocomposites containing SC-15 epoxy resin and polyhedral-oligomeric-sil-sesquioxanes (POSS) have been studied. Dynamic Mechanical Analysis (DMA) results show that the addition of 5 wt% of POSS yielded a 13% increase in the storage modulus and a 16°C enhancement in T_g. Thermo gravimetric Analysis (TGA) results show that the thermal stability of epoxy increased with higher POSS content. Tension tests were used to evaluate the mechanical properties of materials. Both modulus and tensile strength are linear functions of POSS content. Scanning Electric Microscopy (SEM) pictures of fracture surfaces show that the roughness of the fracture surfaces of epoxy increased after adding POSS. Based on experiment results, a three-parameter nonlinear constitutive equation was developed to describe the strain-softening stress-strain relationship behavior of materials. The parameters in this model are the elastic modulus, a strain exponent, m, and a compliance factor, β. Their relationships to the POSS weight fraction were obtained from the experiment results. The simulated stress-strain curves from the model agree with the test data. Analysis of the model shows that both the strain exponent, m, which controls the strain softening and hardening effect of the material, and the compliance parameter, β, which controls the flow stress level of the material, increase with higher POSS content.

Keywords: *nanocomposite, epoxy, POSS, thermal and mechanical properties*

1. Introduction

Epoxy resin has been important to the engineering field for many years. Components made of epoxy-based materials provide outstanding mechanical and thermal properties. Using an additional phase, such as inorganic fillers, to strengthen epoxy resins has become a common practice. Because microscale fillers have been successfully synthesized with epoxy resin [1–5], nanoparticle-filled resins are attracting considerable attention; they can enhance properties sometimes even better than conventional filled polymers at volume fractions between 1% and 5%. Adding small amounts of nanoparticles (<5 wt%) to a matrix system can increase thermal, mechanical, and electrical properties without compromising the weight or processability of the composite. Consequently, many automotive, aerospace, electronics, and biotechnology companies have shown interest in nanocomposite materials [6–11]. The extremely high surface area of nanocomposites is one of its most attractive characteristics because it helps create a great interface in a composite. According to Reynaud *et al.* [12], an interface of 1 nm thick makes up roughly 0.3% of the total polymer's volume in microparticle-filled composites, whereas it can reach 30% of the total volume in nanocomposites.

The primary objective of this paper is to determine the effect of adding polyhedral-oligomeric-sil-sesquioxanes (POSS) on the thermal and mechani-

---

*Corresponding author, e-mail: yzhou@tuskegee.edu

cal properties of epoxy. POSS is inorganic silica-like nanocages 1.5 nm in size that have organic substituents (as shown in Figure 1). Inactive organic substituents make POSS physically compatible with relevant polymers and promote dispersion in the polymer at a molecular level [13], while substituents that are reactive promote curing or grafting reactions [14]. Thermoplastics such as polypropylene [15, 16], polycarbonate [17, 18], and polyamide [19, 20], and thermosets such as epoxy [21, 22] have been reinforced with POSS. Previous results indicate that adding POSS to a matrix system can increase thermal and mechanical properties [23–26].

In this study, POSS was mixed into epoxy with different weight fractions. Tensile tests were performed to evaluate mechanical performance. Thermogravimetric Analysis (TGA) and Dynamic Mechanical Analysis (DMA) were used to evaluate thermal performances. Based on experiment results, a nonlinear constitutive equation was developed to describe the stress-strain relationship of the materials.

2. Experiment

2.1. Materials and manufacturing nanocomposites

The resin used in this study is a commercially available SC-15 epoxy obtained from Applied Poleramic, Inc. It is a low-viscosity, two-phased, toughened epoxy resin system consisting of part A (resin mixture of diglycidylether of bisphenol-A, aliphatic diglycidlether epoxy toughener) and part B (hardener mixture of cycloaliphatic amine and polyoxylalkylamine). The EpoxyCyclohexyl POSS was obtained from Hybrid Plastics. The chemical structure is shown in Figure 1. The average epoxy functionality of EpoxyCyclohexyl POSS is 10. POSS molecules are similar to the smallest silica particles. However, unlike silica or modified clays, each POSS molecule contains covalently bonded reactive functionalites suitable for polymerization or for grafting POSS monomers to polymer chains. Some other POSS molecule also contains nonreactive organic functionalities for solubility and compatibility with various polymer systems. But no nonreactive organic functionalities were attached in EpoxyCyclohexyl POSS.

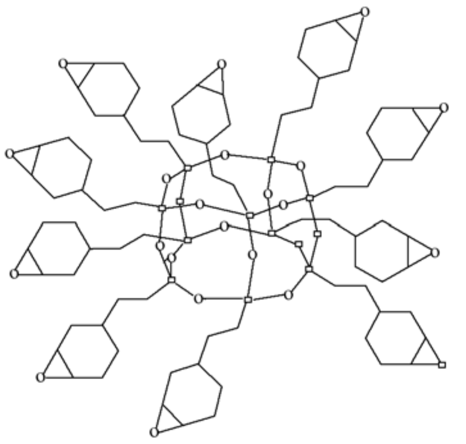

Figure 1. EpoxyCyclohexyl POSS $(C_8H_{13}O_2)_n(SiO_{1.5})_n$

POSS and part A were carefully weighed and mixed together using a magnetic stirring for 24 hours at 800 rpm and 40°C. The weight fractions of POSS ranged from 1 to 5 wt%. Next, part B was added to the modified part A and mixed using a high-speed mechanical stirrer for about 5 minutes. The mix-ratio of part A and part B of SC-15 was 10:3. The rigorous mixing of part A and part B produced highly reactive volatile vapor bubbles during the initial stages of the reaction, which could detrimentally affect the final product by creating voids. A high vacuum was applied for about 30 minutes, using the Brand Tech Vacuum system. After the bubbles were completely removed, the mixture was transferred into a teflon-coated, dog-bone-shaped metal mold and stored for 24 hours at room temperature. The cured material was then de-

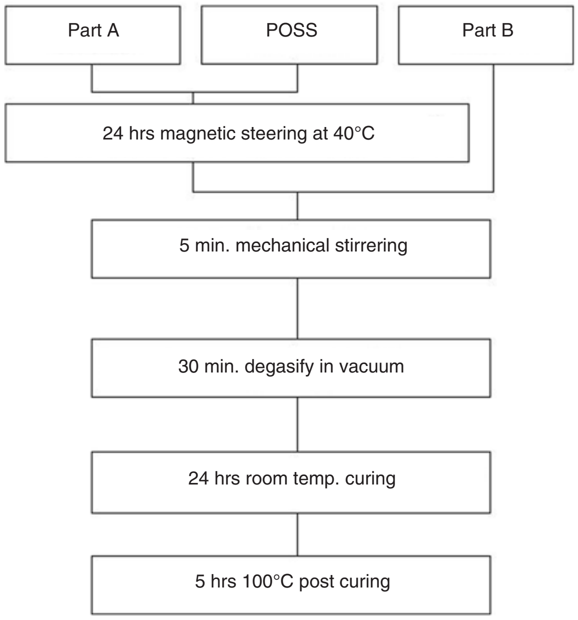

Figure 2. Manufacturing processing of POSS/epoxy nanocomposites

molded and trimmed. Finally, test samples were machined for thermal and mechanical characterization. All panels were post-cured at 100°C for 5 hours. Figure 2 shows the block diagram for manufacturing POSS/epoxy nanocomposites.

2.2. Test procedure

Dynamic mechanic analysis (DMA) was performed on a TA Instruments 2980 operating in the three-point bending mode at an oscillation frequency of 1 Hz. Data were collected from room temperature to 160°C at a scanning rate of 3°C/minute. The sample specimens were cut into rectangular bars, 1.7 mm×30 mm×10 mm, with a diamond saw. Thermogravimetric analysis (TGA) was conducted using a TA Instruments TGA 2950 at a heat rate of 10°C/minute from ambient to 800°C. The TGA samples were cut into small pieces using an ISOMET cutter and were machined to maintain the sample weight of about 10 mg, using a mechanical grinder. These samples were put in ceramic crucibles and placed inside the apparatus. The real-time characteristic curves were generated by Universal Analysis 2000-TA Instruments Inc., a data acquisition system.

Tensile testing on the dogbone-shaped specimens was performed according to ASTM Standard D 638-89. Five replicate specimens from four different materials were tested. All tests were performed at room temperature. The test was performed under displacement control mode at a crosshead speed of 2.0 mm/min and a strain rate of 0.5/min. Two parameters, elastic modulus (E) and ultimate tensile strength (σ_b), were evaluated from each stress-strain curve.

3. Results and discussions

3.1. Thermal properties

The DMA plots in Figure 3 show storage modulus versus temperature as a function of POSS loading. Storage modulus steadily increases with increasing POSS weight percent. The addition of 5 wt% of POSS yielded a 13% increase in the storage modulus at 30°C. POSS is a rigid body; an increase in POSS concentration increases the rigidity of the composite system. Figure 4 shows loss factor versus temperature curves of POSS/epoxy nanocomposites. As POSS content increases, the tanδ peaks of nanocomposites significantly shift to a higher temperature while the widths of tanδ peaks remarkably broaden and their intensities lower. An increase of 16°C in T_g was observed in 5 wt% POSS/epoxy as compared with neat epoxy. According to Huang *et al.* [27], incorporating POSS increases the crosslinking density of resulting nanocomposites. The increase in crosslinking density leads to high T_g, broad tanδ peaks, and high storage modulus.

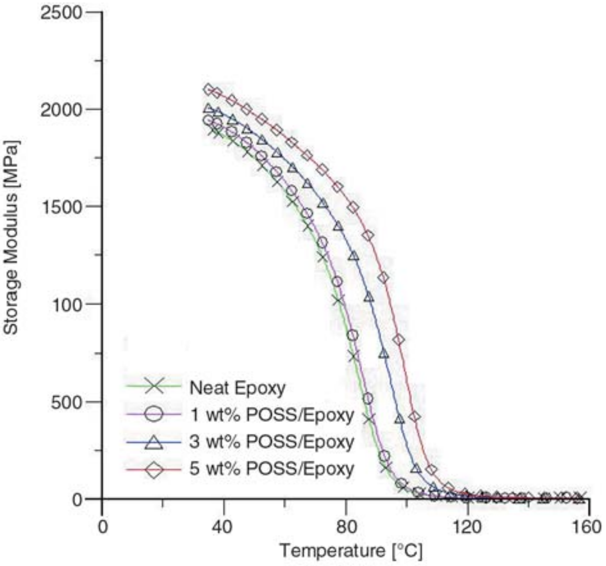

Figure 3. Storage modulus versus temperature plots of POSS/epoxy nanocomposites

Another important characteristic of polymers is their stability at high temperatures. Thermogravimetric analysis (TGA) was used to estimate the thermal stability of POSS/epoxy nanocomposites.

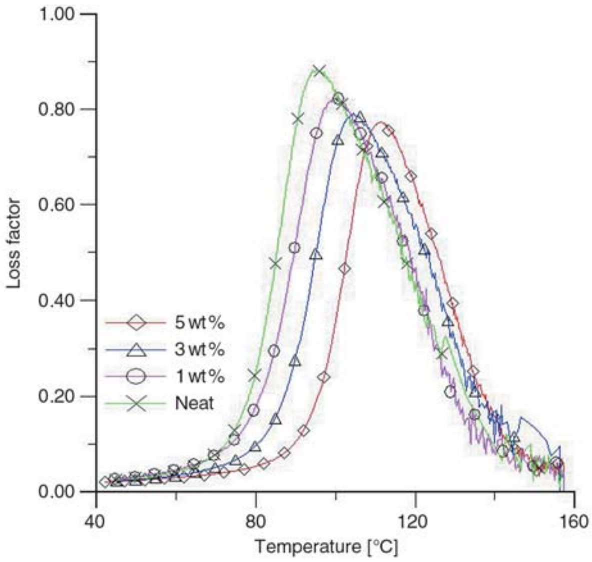

Figure 4. Loss factor versus temperature plots of POSS/epoxy nanocomposites

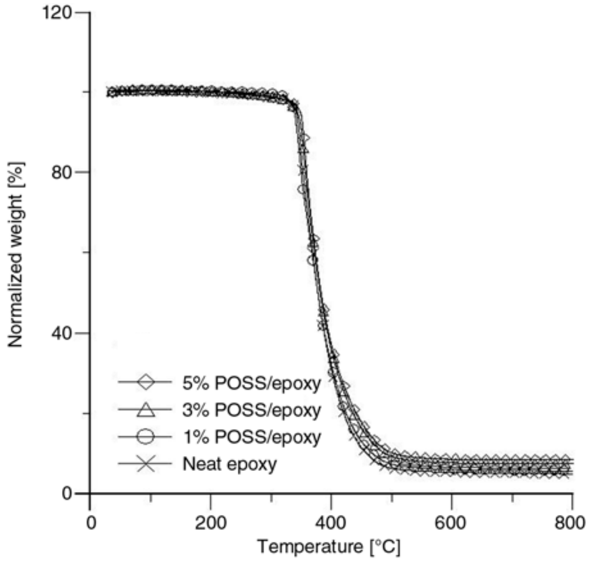

Figure 5. Weight loss versus temperature curves of POSS/epoxy nanocomposites

Figure 5 shows the normalized weights versus temperature curves of four materials. All samples began to decompose around 350°C and completely decomposed around 450°C. This study considers the derivative peaks as the decomposition temperature. As shown in Figure 6, decomposition temperatures increased with higher POSS content. An increase of 10°C in decomposition temperature was observed in 5 wt% POSS/epoxy as compared with neat epoxy.

3.2. Tensile properties

Figure 7 shows the typical tensile stress-strain curves of neat and nanophased epoxy. The stress-strain curves show considerable nonlinearity before reaching maximum stress, which is assumed to be the yield strength of the material. After this point, stress decreased steadily with strain until fracture occurred. Five specimens were tested for each condition; the average properties obtained from these tests are listed in Table 1.

Figure 7 and Table 1 show that the yield strength and modulus of epoxy and POSS/epoxy nanocomposites increase continuously with increasing POSS content. 5% POSS yielded a 16.6% increase in modulus and a 19.4% increase in yield strength. The small size of POSS, which restricts the mobility of polymer chains under loading, improved the modulus and yield strength; good interfacial adhesion between the POSS and matrix also contributed to the reinforcement [25]. Figure 8 represents the variation of modulus E and yield strength σ_s with the weight fraction of POSS as a linear relationship.

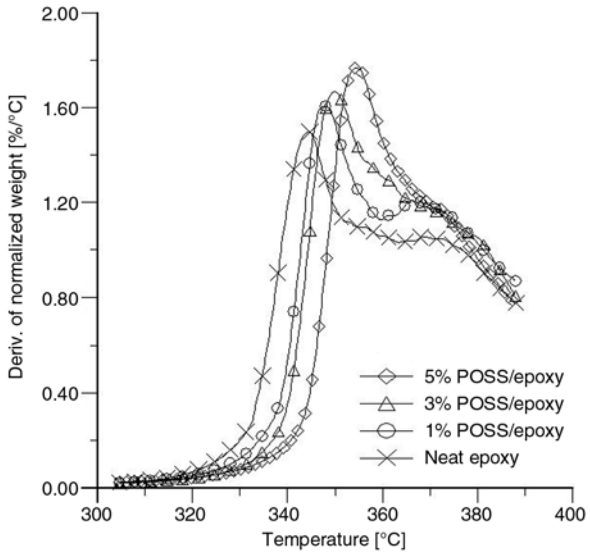

Figure 6. Effect of POSS content on thermal stability of epoxy

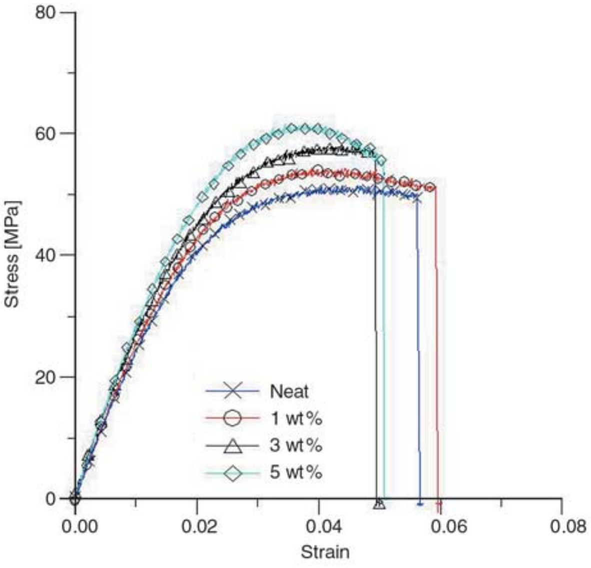

Figure 7. Tensile results of POSS/epoxy stress vs. strain curve

Table 1. Tensile properties of poss/epoxy nanocomposites

Material	Modulus [GPa]	Enhancement in modulus	Strength [MPa]	Enhancement in strength
Neat epoxy	2.59	–	51.5	–
1 wt% POSS	2.73	5.4%	54.3	5.4%
3 wt% POSS	2.77	6.9%	57.9	12.4%
5 wt% POSS	3.02	16.6%	61.5	19.4%

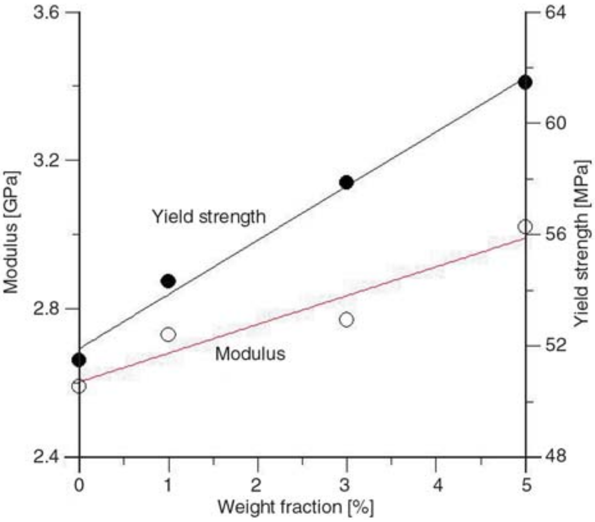

Figure 8. Effect of POSS weight fraction on modulus and yield strength of epoxy

Compared with multi-walled CNT-reinforced epoxy [28], vapor-grown CNF-reinforced epoxy [9], and nanoparticle-reinforced epoxy [29], no optimal loading was observed on the POSS/epoxy system, indicating good dispersion of POSS in epoxy. The Equations (1a) and (1b) fit the modulus and tensile strength data of the composite:

$$E = E_0 + m_1 w_p \tag{1a}$$

$$\sigma_s = \sigma_{s0} + m_2 w_p \tag{1b}$$

where E_0 and σ_{s0} are reference elastic modulus and reference yield strength, and w_p is the weight fraction of POSS. Two other parameters, m_1 and m_2, appearing in Equations (1a) and (1b), represent weight fraction strengthening coefficients for modulus and tensile strength, respectively. Mathematically, they are defined by Equation (2):

$$m_{1,2} = \frac{\partial(E, \sigma_s)}{\partial w_f} \tag{2}$$

Using the least square method, the m values of the composite were calculated as shown by Equations (3a) and (3b):

$$\sigma_s = 51.9 + 194.4W \quad \text{[MPa]} \tag{3a}$$

$$E = 2.60 + 7.7W \quad \text{[GPa]} \tag{3b}$$

3.3. Fracture surfaces

The fracture surfaces of neat epoxy and the nanocomposites were compared using SEM. Figure 9a shows that neat epoxy resin exhibits a relatively smooth fracture surface and that the initial crack occurred at the tension edge of the specimen. The river pattern in Figure 9a indicates a typical cleavage fracture, accounting for the low fracture toughness of the unfilled epoxy. Compared to neat epoxy, the fracture surfaces of the nanocomposites show considerably different fractographic features. For example, the failure surfaces of the nanocomposites containing 1 wt% POSS and 5 wt% POSS are shown in Figure 9b and 9c. Generally, adding POSS into the epoxy matrix results in a much rougher fracture surface and the surface roughness increases with higher POSS content.

The higher magnification micrographs of POSS/epoxy nanocomposites are shown in Figure 10a (for 1% POSS/epoxy) and Figure 10b (for 5% POSS/epoxy). The rougher fracture surface consists of many small smooth zones. These smooth zones nucleate in the material at areas of localized deformation and, in the center of each partly oval-shaped zone, a second-phased particle can be observed, as shown in Figure 10c. During the failure process, the crack propagation changed direction as it crossed second-phased particles. The pinning effect, which prevents crack opening,

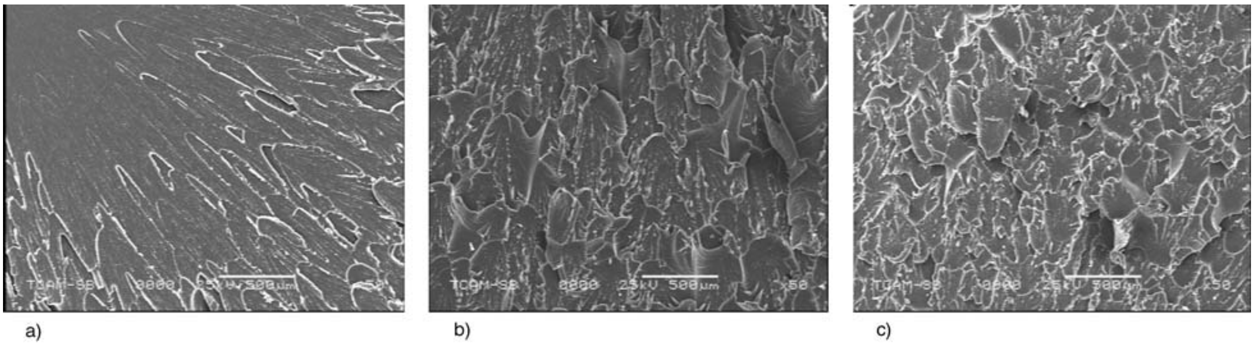

Figure 9. Fracture surface of neat and nanophased epoxy (a – neat epoxy; b – 1 wt%POSS/epoxy and c – 5 wt% POSS/epoxy)

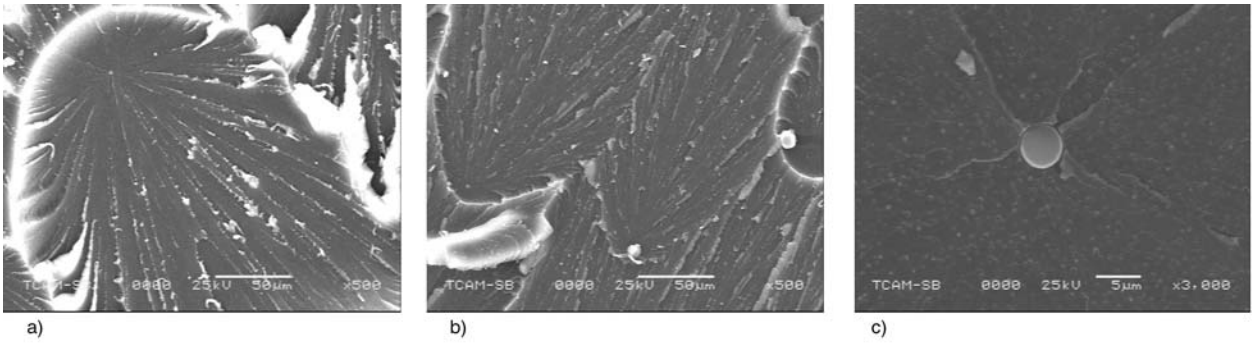

Figure 10. Fracture surface of POSS/epoxy nanocomposite (a – large smooth zone in 1% POSS/epoxy; b – small smooth zone in 5% POSS/epoxy and c – second-phased particle in the center of smooth zone)

increased the strength of the epoxy. The size of the smooth zones on a fracture surface is determined by the number and distribution of second-phased particles. When second-phased parties are few and widely spaced, the cracks propagate longer before coalescing, resulting in a fracture surface with large smooth zones. Smaller zones are formed when many second-phased particles are produced. Figures 10a and 10b show that the size of smooth zones decreases with increasing POSS weight fractions. Fewer smooth zones and more surface roughness imply that the number of second-phased particles increased with increasing POSS content. The path of the crack tip is distorted because of more second-phased particles, which make crack propagation more difficult.

3.4. Constitutive equation

The failure of fiber reinforced epoxy involves a complicated damage accumulation process resulting from random fiber breakage, stress transfer form fiber to matrix, and interface debonding between the fiber and matrix. It is necessary to obtain stress strain relationship of matrix to analyze such a complicated probabilistic failure phenomenon. To better understand the stress-strain relationship of neat and nanophased epoxy, a nonlinear constitutive equation has been developed. In the proposed constitutive model (Equation (4)), the total strain is assumed to be composed of an elastic part and an inelastic part:

$$\varepsilon = \varepsilon_e + \varepsilon_i \tag{4}$$

where ε_e and ε_i represent the elastic and inelastic strains, respectively. The elastic strain is assumed to be path-independent and related to the elastic modulus of the material. It is expressed by Equation (5):

$$\varepsilon_e = \frac{\varepsilon}{E} \tag{5}$$

where E is the elastic modulus of the POSS/epoxy material, which is a function of both strain rate and temperature, and where σ is the stress. The inelastic strain, ε_i, is assumed to be a function of both stress and strain, as shown by Equation (6):

$$\varepsilon_i = \beta\sigma\varepsilon^m \tag{6}$$

where β represents a compliance parameter and m is a strain exponent. Therefore, by substituting Equations (5) and (6) into Equation (4) and rearranging, we obtain the Equation (7):

$$\sigma = \frac{E\varepsilon}{1 + E\beta\varepsilon^m} \tag{7}$$

To determine the material parameters in the constitutive equation, Equation (7) is rewritten into Equation (8):

$$\frac{\varepsilon}{\sigma} - \frac{1}{E} = \beta\varepsilon^m \tag{8}$$

This equation, on taking log on both sides, transforms into Equation (9):

$$\ln\left(\frac{\varepsilon}{\sigma} - \frac{1}{E}\right) = \ln\beta + m\ln\varepsilon \tag{9}$$

Equation (9) represents a linear plot of $\ln[\varepsilon/\sigma - 1/E]$ versus $\ln\varepsilon$. The slope of the linear plot is m and the intercept at $\varepsilon = 1$ is $\ln\beta$. These linear plots at different strain rates are nearly parallel to each other, which means that the material has the same strain

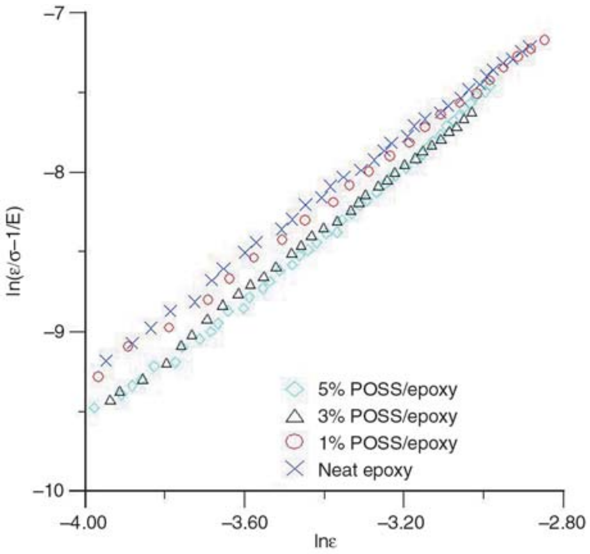

Figure 11. The plot of ln[ε/σ–1/E] vs. lnε of materials

exponent at different test conditions. The plots of ln[ε/σ–1/E] versus lnε of neat epoxy and POSS/epoxy is shown in Figure 11. The compliance factor β and strain exponent m obtained from these plots are plotted as a function of POSS content in Figure 12. Also, strain exponent m and compliance factor expressed as functions of POSS content are as follows. See Equations (10a) and (10b), respectively:

$$m = 1.85 + 4.5W \tag{10a}$$

$$\beta = 0.150 + 2.40W \quad [1/\text{MPa}] \tag{10b}$$

As shown in Figure 13, elastic modulus E, compliance factor β, and strain exponent m in Equation (7), the simulated stress-strain plots fit the experiment data very well.

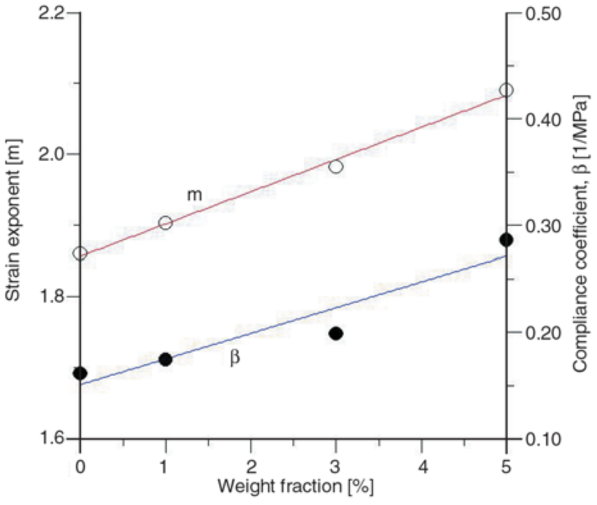

Figure 12. Compliance factor β and strain exponent m

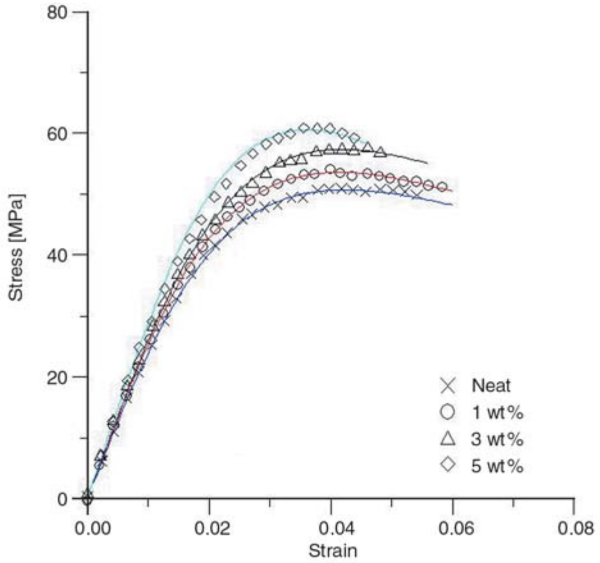

Figure 13. Comparison between experiment results and simulated results

4. Conclusions

1. DMA results exhibited a 16°C increase in T_g in 5 wt% POSS/epoxy as compared with neat epoxy.
2. TGA results show that the POSS content has successfully increased the decomposition temperature as well.
3. The tensile results indicate that 5 wt% loading of POSS in epoxy resin showed the highest improvement in the tensile strength as compared to the neat systems. Also, there was an improvement in the elastic modulus.
4. The nonlinear constitutive equation established in this study can predict the stress-strain tensile behavior of the POSS/epoxy nanocomposite.

Acknowledgements

The authors would like to gratefully acknowledge the support of the National Science Foundation.

References

[1] Donnet J. B.: Nano and microcomposites of polymers elastomers and their reinforcement. Composites Science and Technology, **63**, 1085–1088 (2003).

[2] Zheng Y., Zheng Y., Ning R.: Effects of nanoparticles SiO_2 on the performance of nanocomposites. Materials Letters, **57**, 2940–2944 (2004).

[3] Day R. J., Lovell P. A., Wazzan A. A.: Toughened carbon/epoxy composites made by using core/shell particles. Composites Science and Technology, **61**, 41–56 (2001).

[4] Bagheri R., Pearson R. A.: Role of particle cavitation in rubber-toughened epoxies: II. Inter-particle distance. Polymer, **41**, 269–276 (2001).

[5] Kumar K. D., Kothandaraman B.: Modification of (DGEBA) epoxy resin with maleated depolymerised natural rubber. Express Polymer Letters, **2**, 302–311 (2008).

[6] Zhou Y. X., Wu P. X., Cheng Z-Y., Ingram J., Jeelani S.: Improvement in electrical, thermal and mechanical properties of epoxy by filling carbon nanotube. Express Polymer Letters, **2**, 40–48 (2008).

[7] Chisholm N., Mahfuz H., Rangari V. K., Ashfaq A., Jeelani S.: Fabrication and mechanical characterization of carbon/SiC-epoxy nanocomposites. Composite Structures, **67**, 15–124 (2005).

[8] Gojny F. H., Wichmann M. H. G., Fiedler B., Bauhofer W., Schulte K.: Influence of nano-modification on the mechanical and electrical properties of conventional fibre-reinforced composites. Composites, Part A: Applied Science and Manufacturing, **36**, 1525–1535 (2005).

[9] Pervin F., Zhou Y., Rangari V., Jeelani S.: Testing and evaluation on the thermal and mechanical properties of carbon nano fiber reinforced SC-15 epoxy. Materials Science and Engineering, Part A, **405**, 246–253 (2005).

[10] Zhou Y., Pervin F., Biswas M. A., Rangari V., Jeelani S.: Fabrication and characterization of montmorillonite clay-filled SC-15 epoxy. Materials Letters, **60**, 869–873 (2006).

[11] Auad M. L., Nutt S. R., Pettarin V., Frontini P. M.: Synthesis and properties of epoxy-phenolic clay nanocomposites. Express Polymer Letters, **1**, 629–639 (2007).

[12] Reynaud E., Gauthier C. Perez J.: Nanophases in polymers. Review Metallurgie, **96**, 169–176 (1999).

[13] Haddad T. S., Stapleton R., Jeon H. G., Mather P. T., Lichtenhan J. D., Phillips S.: Nanostructured hybrid organic/inorganic materials. Silsesquioxane modified plastics. Polymer Preprints, **40**, 496–497 (1999).

[14] Lee A., Lichtenhan J. D.: Thermal and viscoelastic property of epoxy-clay and hybrid inorganic-organic epoxy nanocomposites. Journal of Applied Polymer Science, **73**, 1993–2001 (1999).

[15] Fina A., Tabuani D., Frache A., Camino G.: Polypropylene-polyhedral oligomeric silsesquioxanes (POSS) nanocomposites. Polymer, **46**, 7855–7866 (2005).

[16] Fina A., Abbenhuis H. C. L., Tabuani D., Frache A., Camino G.: Polypropylene metal functionalised POSS nanocomposites: A study by thermogravimetric analysis. Polymer Degradation and Stability, **91**, 1064–1070 (2006).

[17] Mulliken A. D., Boyce M. C.: Polycarbonate and a polycarbonate-POSS nanocomposite at high rates of deformation. Journal of Engineering Materials and Technology, **128**, 543–550 (2006).

[18] Zhao Y., Schiraldi D. A.: Thermal and mechanical properties of polyhedral oligomeric silsesquioxane (POSS)/polycarbonate composites. Polymer, **46**, 11640–11647 (2005).

[19] Ramasundaram S. P., Kim K. J.: In-situ synthesis and characterization of polyamide 6/POSS nanocomposites. Macromolecular Symposia, **249–250**, 295–302 (2007).

[20] Baldi F., Bignotti F., Ricco L., Monticelli O., Ricco T.: Mechanical and structural characterization of POSS-modified polyamide 6. Journal of Applied Polymer Science, **100**, 3409–3414 (2006).

[21] Matejka L., Strachota A., Plestil J., Whelan P., Steinhart M., Šlouf M.: Epoxy networks reinforced with polyhedral oligomeric silsesquioxanes (POSS): Structure and morphology. Macromolecules, **37**, 9449–9456 (2004).

[22] Strachota A., Kroutilova I., Kovarova J., Matejka L.: Epoxy networks reinforced with polyhedral oligomeric silsesquioxanes (POSS). Thermomechanical properties. Macromolecules, **37**, 9457–9464 (2004).

[23] Fu B., Namani M., Lee A.: Influence of phenyl-trisilanol polyhedral silsesquioxane on properties of epoxy network glasses. Polymer, **44**, 7739–7747(2003).

[24] Liu Y., Zheng S., Nie K.: Epoxy nanocomposites with octa(propylglycidyl ether) polyhedral oligomeric silsesquioxane. Polymer, **44**, 12016–12025 (2005).

[25] Dodiuk H., Kening S., Blinsky I., Dotan A., Buchman A.: Nanotailoring of epoxy adhesives by polyhedral-oligomeric-sil-sesquioxanes (POSS). International Journal of Adhesion and Adhesives, **25**, 211–18 (2005).

[26] Liu H. Z., Zhang W., Zheng S. X.: Montmorillonite intercalated by ammonium of octaaminopropyl polyhedral oligomeric silsesquioxane and its nanocomposites with epoxy resin. Polymer, **46**, 157–165 (2005).

[27] Huang J-C., He C-B., Xiao Y., Mya K. Y., Dai J., Siow Y. P.: Polyimide/POSS nanocomposites: Interfacial interaction, thermal properties and mechanical properties. Polymer, **44**, 4491–4499 (2003).

[28] Zhou Y., Pervin F., Lewis L., Jeelani S.: Experimental study on the thermal and mechanical properties of multi-walled carbon nanotube-reinforced epoxy. Materials Science and Engineering, Part A: Structural Materials: Properties, Microstructure and Processing, **452–453**, 657–664 (2007).

[29] Rodgers R., Mahfuz H., Rangari V. K., Chisholm N., Jeelani S.: Infusion of SiC nanoparticles into SC-15 epoxy: An investigation of thermal and mechanical response. Macromolecular Materials and Engineering, **290**, 423–429 (2005).

eXPRESS Polymer Letters Vol.2, No.7 (2008) 502–510
Available online at www.expresspolymlett.com
DOI: 10.3144/expresspolymlett.2008.60

Starch-based nanocomposites reinforced with flax cellulose nanocrystals

X. Cao[1], *Y. Chen*[1,2], *P. R. Chang*[1,3*], *A. D. Muir*[1], *G. Falk*[1]

[1]BioProducts and Bioprocesses National Science Program, Agriculture and Agri-Food Canada, 107 Science Place, Saskatoon, SK, S7N 0X2, Canada
[2]Research Centre for Medical and Structural Biology, School of Basic Medical Science, Wuhan University, Wuhan 430071, China
[3]Department of Agricultural and Bioresourse Engineering, University of Saskatchewan, Saskatoon, SK, S7N 5A9, Canada

Received 3 April 2008; accepted in revised form 23 May 2008

Abstract. In this study, the cellulose crystals, prepared by acid hydrolysis of flax fiber, consisted of slender rods with lengths ranging from 100 to 500 nm and diameters ranging from 10 to 30 nm, respectively. After mixing the suspension of flax cellulose nanocrystals (FCNs) and plasticized starch (PS), the nanocomposite films were obtained by the casting method. The effects of FCNs loading on the morphology, thermal behaviour, mechanical properties and water sensitivity of the films were investigated by means of wide-angle X-ray diffraction, differential scanning calorimetry, tensile testing, and water absorption testing. Scanning electron microscopy photographs of the failure surfaces clearly demonstrated a homogeneous dispersion of FCNs within the PS matrix and strong interfacial adherence between matrix and fillers, which led to an increase of glass transition temperature ascribed to the starch molecular chains in the starch-rich phase. In particular, these nanocomposite films exhibited a significant increase in tensile strength and Young's modulus from 3.9 to 11.9 MPa and from 31.9 to 498.2 MPa, respectively, with increasing FCNs content from 0 to 30 wt%. Also, with a loading of FCNs, the resulting nanocomposite films showed a higher water resistance. Therefore, FCNs played an important role in improving the mechanical properties and water resistance of the starch-based materials.

Keywords: *nanocomposites, reinforcements, starch, flax, mechanical properties*

1. Introduction

The development of commodities derived from petrochemical polymers has brought many benefits to mankind. However, it is becoming more evident that the ecosystem is considerably disturbed and damaged as a result of the non-degradable plastic materials used in disposable items. Therefore, the interest in polymers from renewable resources has recently gained exponential momentum and the use of biodegradable and renewable materials to replace conventional petroleum plastics for disposable applications is becoming popular [1, 2]. Within the broad family of renewable polymers, starch is one of the most attractive and promising sources for biodegradable plastics because of the abundant supply, low cost, renewability, biodegradability, and ease of chemical modifications [3, 4]. In recent years, plasticized starch (PS) has attracted considerable attention and has offered an interesting alternative for synthetic polymers where long-term durability is not needed and rapid degradation is an advantage [5]. However, compared with conventional synthetic thermoplastics, biodegradable products based on starch, unfortunately, still exhibit many disadvantages, such as water sensitivity, brittleness, and poor mechanical properties [6]. Vari-

---

[*]Corresponding author, e-mail: Changp@agr.gc.ca

ous physical or chemical means have been used to solve these problems, including blending with other synthetic polymers [7–9], the chemical modification [10–12], graft copolymerisation [13], and incorporating fillers such as lignin [14], clay [15], and multi-walled carbon nanotubes [16].

More recently, there is an increased use of cellulose nanocrystals (CNs) as the loading-bearing constituent in developing new and inexpensive biodegradable materials due to a high aspect ratio, a high bending strength of about 10 GPa, and a high Young's modulus of approximately 150 GPa [17]. The CNs from various sources such as cotton, tunicate, algae, bacteria, ramie, and wood for preparation of high performance composite materials have been investigated extensively [18]. Both natural and synthetic polymers were explored as the matrixes. Natural polymers such as poly(β-hydroxyoctanoate) (PHO) [19], soy protein [20], silk fibroin [21] reinforced with cellulose whiskers were reported. Meanwhile, Poly-(styrene-*co*-butyl acrylate) (poly(S-*co*-BuA)) [22], poly(vinyl chloride) (PVC) [23], polypropylene [24], waterborne polyurethane [25], were also used as synthetic matrixes.

The flax plant (*Linum usitatissimum*) is a member of the Linaceae family, which is an important crop in many regions of the world. Fibers from flax have been used for thousands of years to make different textile products because of their excellent fiber characteristics. Therefore, the search on short fibers from flax as a replacement for synthetic fibers in many non-textile products, e.g. in polymer compounds, building materials and absorbent materials, has attracted much attention in the last decade [26]. However, incorporating flax cellulose nanocrystals (FCNs) in the starch-based composite films has not been reported in the literatures. In present work, we attempt to prepare CNs from flax fiber by acid hydrolysis with concentrated sulfuric acid, and then use the resulting CNs to reinforce PS for preparation of nanocomposite films with improved performances. The resulting films were prepared by casting the mixture of aqueous suspensions of CNs and PS in various weight ratios. The morphology, structure, and performance of the resulting nanocomposite films were investigated by scanning electron microscopy (SEM), wide-angle X-ray diffraction (WAXD), differential scanning calorimetry (DSC), and measurement of the mechanical properties and water uptake.

2. Experimental

2.1. Materials

Field pea starch, with average granule size of about 29 μm and composed of 35% amylose and 65% amylopectin, was supplied by Nutri-Pea Limited Canada (Portage la Prairie, Canada). Raw flax fiber was supplied by Biolin Research Incorporated, Canada. The glycerol (99% purity), sodium hypochlorite solution (available chlorine 10–13%), sodium hydroxide, and sulfuric acid (98%) were bought from Sigma-Aldrich Canada Ltd. (Oakville, Canada) and used as received.

2.2. Preparation of FCNs

A colloidal suspension of cellulose nanocrystals in water was prepared by acid-catalyzed hydrolysis of flax fiber. Briefly, the flax fiber (30 g) was first cut into small fragments and mixed with sulfuric acid aqueous solution (250 ml, 64%) and stirred vigorously at 45°C for 4 h. Subsequently, the suspension was neutralized with sodium hydroxide aqueous solution (40%), discolored by sodium hypochlorite solution and washed by dialyzing. The dispersion of flax cellulose nanocrystals (FCNs) with a solid content of 1.4 wt% was obtained through a 30 min ultrasonic treatment. The suspension did not sediment or flocculate as a consequence of the surface sulfate groups that were created during the sulfuric treatment [27].

2.3. Preparation of the PS/FCNs nanocomposite films

The fabrication of plasticized starch/flax cellulose nanocrystals (PS/FCNs) composite films was based on a convenient casting solution process. Starch, glycerol, cellulose nanocrystallites suspension and distilled water were mixed together in order to obtain nanocomposite films with a homogeneous dispersion. The glycerol content was fixed at 36 wt% based on the dry starch matrix. Then this mixture was charged into a bottom flask equipped with a stirrer and heated at 100°C for 30 min for the starch to be gelatinized. After cooling down to about 70°C, the resulting paste was degassed under vacuum to remove the remaining air and cast in a polystyrene square Petri dish, followed by drying in a vent oven at 50°C. By changing the content of FCNs over a range of 5, 10, 15, 20, 25, and 30 wt%, a series of plasticized PS/FCNs nanocomposite films with a thickness of about 0.3 mm were prepared and coded as PS/FCNs-5, PS/FCNs-10, PS/FCNs-15, PS/FCNs-20, PS/FCNs-25, and PS/FCNs-30, respectively, in which the FCNs content was expressed on water-free PS matrix. As a control, a neat PS film without addition of FCNs was obtained using the same fabrication process. Before various characterizations, the resulting films were kept in a conditioning desiccator of 43% relative humidity (*RH*) for one week at room temperature to ensure the equilibration of the water content in the films.

2.4. Characterizations

AFM was used to characterize the morphology of FCNs. Measurements were conducted in tapping mode by a Nanoman AFM (Veeco Metrology Group, USA) at ambient temperature. In the sample preparation, a droplet of dilute FCNs suspension was coated on a flake of mica, and the water was evaporated at ambient temperature.

Scanning electron microscopy (SEM) measurements were carried out on a field-emission scanning electron microscope (FESEM, JEOL JSM-6700, JEOL Ltd, Japan). To study the structure of the nanocomposites, the failure surfaces of the PS/FCNs films after tensile testing was observed. The samples were coated with Platinum and observed with an accelerating voltage of 5 kV.

Attenuated Total Reflectance Fourier Transform Infrared (ATR-FTIR) spectra of the film samples were recorded on a Nicolet 5700 FTIR spectrometer (Thermo Electron Corporation, Waltham, MA, USA). The PS, PS/FCNs-10, PS/FCNs-20 and PS/FCNs-30 films were taken at random from the flat films and data were collected at room temperature over 16 scans with a resolution of 4 cm^{-1}.

Wide-angle X-ray diffraction patterns were recorded on a Bruker AXS X-ray diffraction (Bruker AXS Inc., Madison, WI, USA), using CuK_α radiation ($\lambda = 0.154$ nm) at 40 kV and 30 mA with a scan rate of 4°/min. The diffraction angle ranged from 4 to 40°.

Differential scanning calorimetry (DSC) measurement of the films was carried out on a DSC204 apparatus (Netzsch Co., Germany) under a nitrogen atmosphere. Each sample conditioned at 43% *RH* was subjected to the heating/cooling cycle between –100 to 120°C to obtain reproducible glass transition temperature (T_g) values. In this case, T_g was taken at the half-variation in the heat capacity of the second run. The heating rate was 10°C/min.

The tensile strength and elongation at break of the films were measured on a universal testing machine (CMT 6503, Shenzhen SANS Test Machine Co. Ltd., China) at room temperature with gauge length of 5 cm and crosshead speed of 10 mm/min. An average value of five replicates for each sample was taken.

The kinetics of water absorption was determined for all composites. The samples used were thin rectangular strips with dimensions of 50 mm×10 mm×0.3 mm. The samples were dried at 80°C under vacuum overnight and kept at 0% *RH* (P_2O_5) for one week. After weighing, they were conditioned at room temperature in a desiccator of 98% *RH* ($CuSO_4{\cdot}5H_2O$ saturated solution). The conditioning of samples in high moisture atmosphere was preferred to the classical technique of immersion in water, because starch is very sensitive to water and can partially dissolve after long time exposure to water. The samples were removed at specific intervals and weighed until the equilibrium state was reached. The water uptake (*WU*) of the samples was calculated by Equation (1):

$$WU\,[\%] = \frac{W_t - W_0}{W_0} \cdot 100 \tag{1}$$

where W_0 and W_t were the weights of the sample before exposure to 98% *RH* and after *t* h exposure to 98% *RH*, respectively. An average value of three replicates for each sample was taken.

3. Results and discussions

3.1. Morphology of FCNs and PS/FCNs nanocomposites

The AFM image of a dilute suspension of FCNs in Figure 1 shows that the suspension contains flax cellulose fragments consisting of both individual and aggregated nanocrystals. These fragments display slender rods and have a broad distribution in

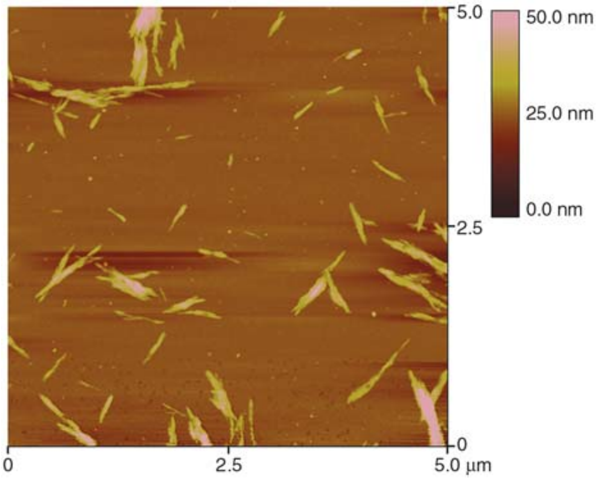

Figure 1. AFM topography image of FCNs after drying on a mica surface

size, which have lengths (L) ranging from 100 to 500 nm and diameters (D) ranging from 10 to 30 nm.

Figure 2 shows the SEM images of the failure surfaces of PS matrix and nanocomposite films. As compared to the PS film, the morphology of the FCNs in the PS matrix can be easily identified. The FCNs appear as white dots, whose concentration on the failure surface of the nanocomposites is a direct function of the filler loading from 10 to 30 wt%. These white dots correspond to the nanocrystals in the perpendicular plane of the nanocomposite films. No large aggregates and a homogeneous distribution of the FCNs in the PS matrix were observed in all nanocomposite films, implying good adhesion between fillers and matrix. This is attributed to the good compatibility resulting from the chemical similarities between starch and cellulose and the hydrogen bonding interactions existing in the interface between fillers and matrix. Such an even and uniform distribution of the fillers in the matrix could play an important role in improving the mechanical performance of the resulting nanocomposite films as discussed later.

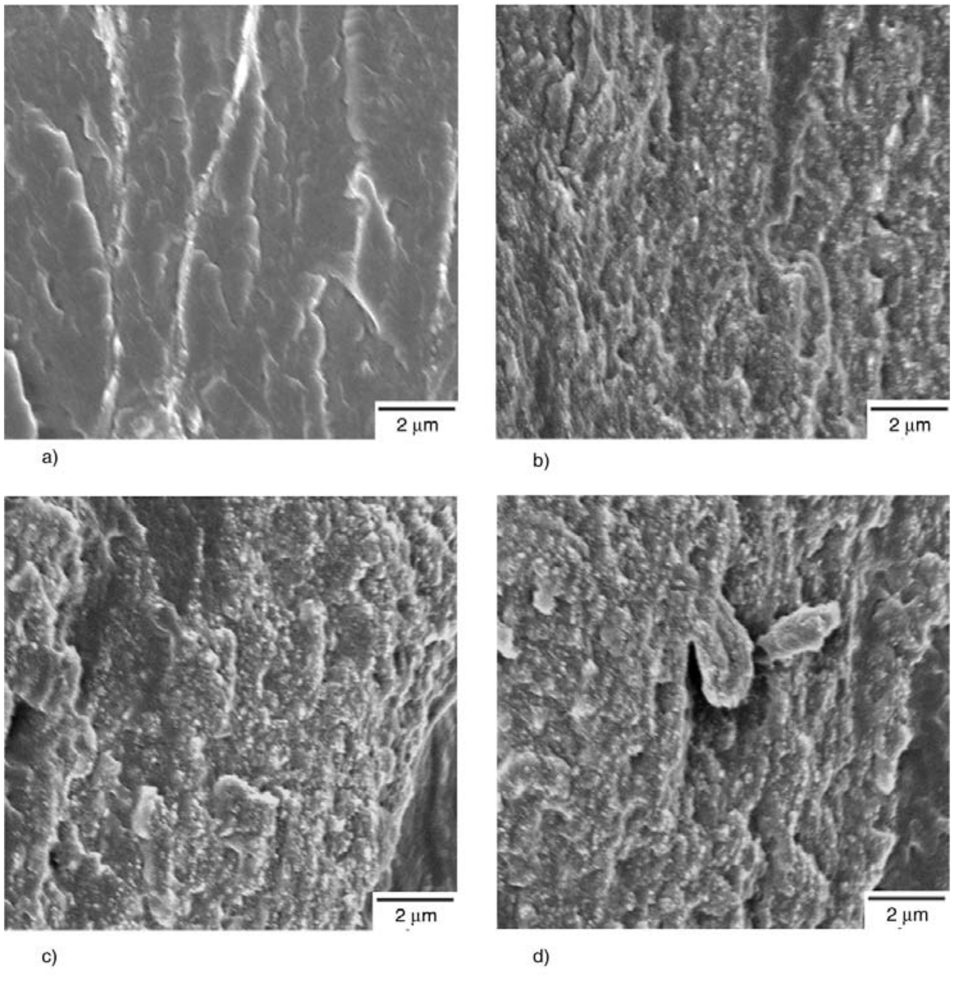

Figure 2. FESEM images of the failure surfaces of the PS and PS/FCNs nanocomposits with different FCNs content: a, 0 wt%; b, 10 wt%; c, 20 wt%; d, 30 wt%. (Scale bar: 2.0 µm)

3.2. Structure of PS/FCNs nanocomposites

Figure 3 shows the FTIR spectra of the PS, PS/FCNs-10, PS/FCNs-20 and PS/FCNs-30 films. The peaks at 3280 and 993 cm^{-1} in the spectra of PS were attributed to the stretching vibrations of the hydrogen bonding –OH groups and C–O stretching vibrations in starch, respectively [9, 28]. The composite films containing cellulose nanocrystals as filler exhibited almost the same FTIR spectra as the PS film due to the chemical similarities between starch and cellulose. However, the relative peak strength of stretching vibrations for –OH groups in the FTIR spectra composite films weakened, indicating the hydrogen bonding between starch molecules was partially destroyed. Furthermore, the wavenumber of the peak for C–O stretching vibrations shifted from 993 to 982 as FCNs content changed from 0 to 30 wt%, this suggested that new interactions between cellulose and starch molecules as a result of the addition of cellulose nanocrystals into starch.

The WAXD of the nanocomposites was studied as a function of the FCNs content and the corresponding diffractograms are shown in Figure 4. For the PS film, a typical C-type crystallinity pattern with peaks at 2θ = 5.6° (characteristic of B type polymorphs), 17.0° (characteristic of both A and B type polymorphs), 20.1 and 22.5° (characteristic of B type polymorphs) were clearly observed [29]. The crystalline structure resulting from spontaneous recrystallization or retrogradation of starch molecules after melting or gelatinization has frequently been detected in food and thermoplastic materials [30]. In this case, the samples had been stored for more than 3 months before WAXD testing. With the addition of FCNs in the starch matrix, some diffraction peaks appear in the diffractograms. With an increase of the FCNs content in the films, the peaks become more significant. When the FCNs content increases to more than 20 wt%, three well-defined peaks at 2θ = 14.7, 16.5, and 22.7° are observed, which corresponds to the typical crystal pattern of cellulose I. Although the diffraction peak intensity of starch and cellulose in the nanocomposite changes with the composition ratio, no evidence of any additional peak or peak shift in the diffraction angles is observed. Therefore, it can be concluded that the diffractograms of nanocomposites are only superimpositions of the diffractograms of the two components.

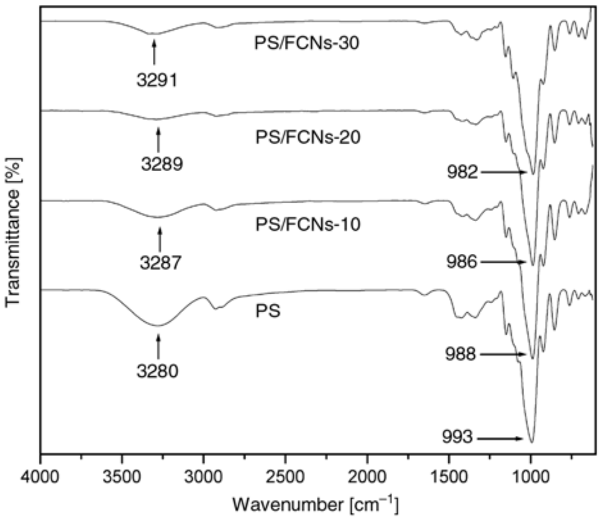

Figure 3. The FTIR spectra of the PS and PS/FCNs nanocomposite films

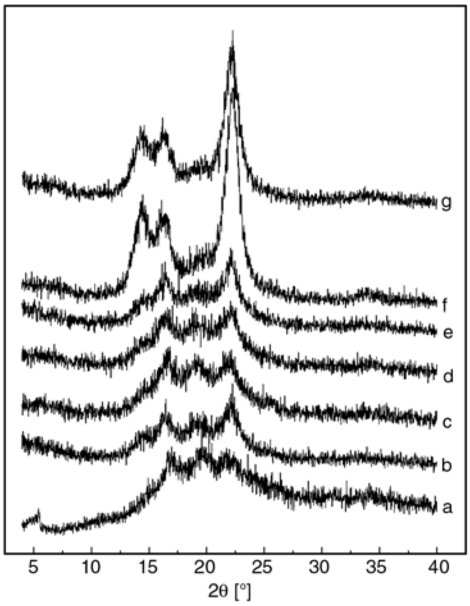

Figure 4. The WXRD patterns for PS and PS/FCNs nanocomposites: a – PS; b, PS/FCNs-5; c – PS/FCNs-10; d – PS/FCNs-15; e – PS/FCNs-20; f – PS/FCNs-25; g – PS/FCNs-30

3.3. Thermal analysis

Figure 5 shows the DSC thermograms in the temperature range of –100 to 120°C of the PS/FCNs nanocomposites conditioned at 43% *RH*. As we know, in DSC experiments, the glass transition temperature (T_g) is generally taken as the inflection point of the specific heat increment at the glass-rubber transition. From Figure 5 it is obvious that all samples display two distinct specific heat increments, which correspond to the glass transitions of

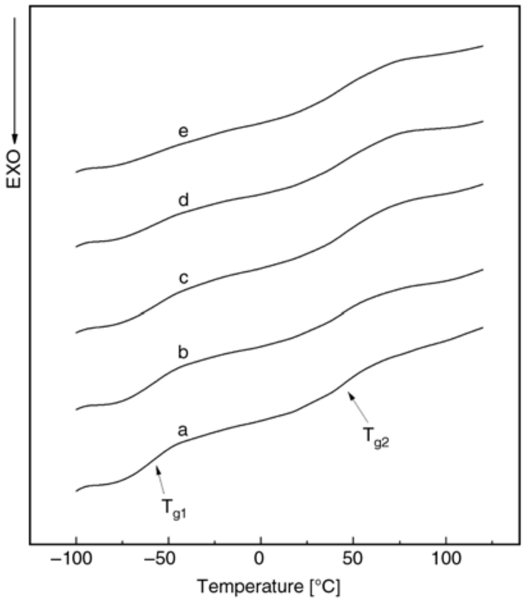

Figure 5. DSC thermograms of PS and PS/FCNs nanocomposites with different FCNs content: a – 0 wt%; b – 5 wt%; c – 10 wt%; d – 20 wt%; e – 30 wt%

the PS matrix. The values of T_g for all the nanocomposites are tabulated in Table 1. As Dufresne et al have previously reported, the PS plasticized by glycerol is a complex heterogeneous system composed of glycerol-rich domains dispersed in a starch-rich continuous phase and each phase exhibits its own T_g [31]. Therefore, the transitions located in the temperature ranged from –80 to –50°C and from 30 to 60°C can be assigned to T_{g1} of glycerol-rich phase and T_{g2} starch-rich phase respectively. With an increase in the FCNs fillers from 0 to 30 wt%, no obvious change of the value of T_{g1} at low temperature for the glycerol-rich phase is observed. However, T_{g2} for starch-rich phase shifts to higher temperature from 43.3 to 48.8°C, which indicates that FCNs restrict the mobility of starch chains due to the strong intermolecular interactions between starch and stiff FCNs.

3.4. Mechanical properties

The mechanical properties of the neat PS matrix films as well as the nanocomposite films reinforced with various contents of FCNs were investigated by tensile testing at room temperature. The typical stress-strain curves of the PS and its FCNs nanocomposites are shown in Figure 6. Generally, the nanocomposite films exhibit two characteristic regions of deformation behaviour. At low strains (<10%), the stress increases rapidly with an increase in strain. At higher strain the stress regularly increases with the strain increasing up to the break of the films. No evidence of necking phenomenon at the stress-strain curves confirms the good dispersion of the FCNs in the matrix and homogeneous morphology of the nanocomposites, which correlates with the results from SEM images. The dependence of tensile strength, Young's modulus, and elongation at break on FCNs content for the PS/FCNs nanocomposites is plotted in Figure 7, and the corresponding data are presented in Table 2. From the results we can see that the FCNs content has a profound effect on the mechanical properties. The tensile strength increases from 3.9 to 11.9 MPa and Young's modulus increase signifi-

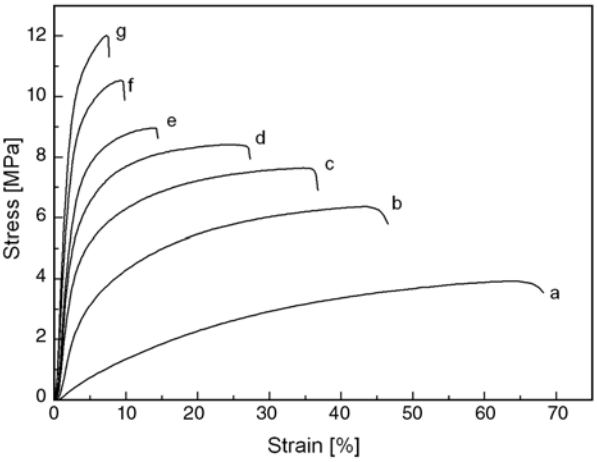

Figure 6. Stress-strain curves of PS and PS/FCNs nanocomposite films with FCNs content: a – 0 wt%; b – 5 wt%; c – 10 wt%; d – 15 wt%; e – 20 wt%, f – 25 wt%; g – 30 wt%

Table 1. The DSC data of PS and the PS/FCNs nanocomposites

Sample	$T_{g1,\,mid}$ [°C]	ΔCp [J/g·K]	$T_{g2,\,mid}$ [°C]	ΔCp [J/g·K]
PS	–58.3	0.375	43.3	0.419
PS/FCNs-5	–55.8	0.319	44.9	0.550
PS/FCNs-10	–56.7	0.321	47.2	0.613
PS/FCNs-20	–55.1	0.319	47.8	0.497
PS/FCNs-30	–55.6	0.247	48.8	0.619

Table 2. Mechanical properties of PS and PS/FCNs nanocomposites obtained from tensile tests: tensile strength (σ), Young's modulus (*E*), and elongation at break (ε_B)

Sample	σ [MPa]	E [MPa]	ε_B [%]
PS	3.9 ± 0.3	31.9 ± 5.1	68.2 ± 3.1
PS/FCNs-5	6.4 ± 0.2	82.6 ± 5.3	44.3 ± 5.2
PS/FCNs-10	7.6 ± 0.3	180.4 ± 13.2	35.9 ± 4.3
PS/FCNs-15	8.2 ± 0.4	255.3 ± 12.1	26.8 ± 5.5
PS/FCNs-20	8.9 ± 0.3	311.9 ± 20.5	14.1 ± 4.2
PS/FCNs-25	10.5 ± 0.5	447.5 ± 14.3	9.4 ± 1.6
PS/FCNs-30	11.9 ± 0.8	498.2 ± 23.4	7.2 ± 1.8

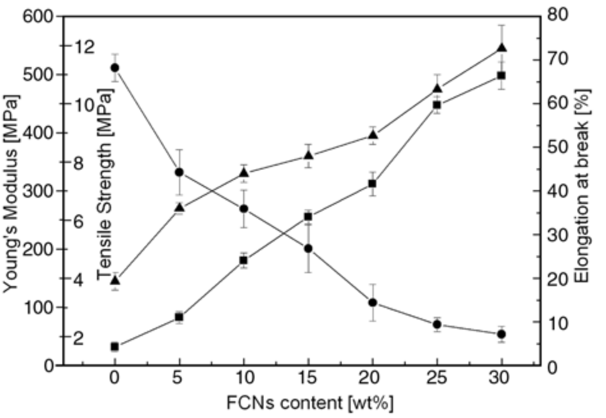

Figure 7. The mechanical properties of tensile strength (▲), Young's modulus (■), and elongation at break (•) of PS/FCNs nanocomposite as a function of FCNs content

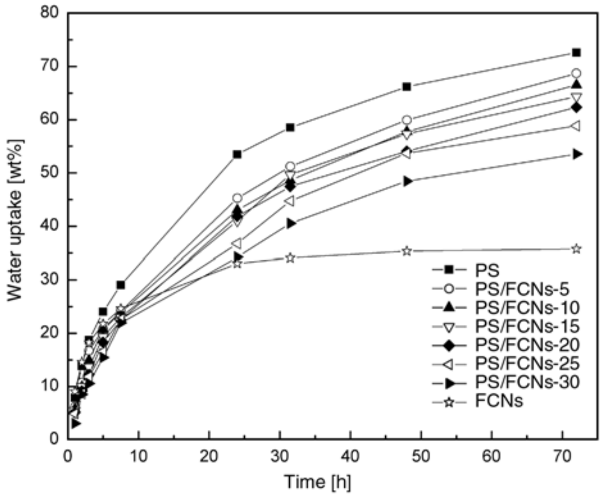

Figure 8. Water uptake during conditioning in 98% *RH* as a function of time for the PS and PS/FCNs films

cantly from 31.9 to 498.2 MPa with increasing filler content from 0 to 30 wt%, respectively, while the elongation at break decreases from 68.2 to 7.2%. This can probably be explained by the reinforcement effect from the homogeneously dispersed high-performance FCNs fillers in the PS matrix and the strong hydrogen bonding interaction between FCNs and PS molecules. The cellulose nanocrystals from flax fiber showed an effect similar to that of ramie-based [32] on the mechanical properties in the PS-based nanocomposites.

3.5. Water sensitivity

The water uptake of the PS and PS/FCNs films during conditioning in 98% *RH* as a function of time is shown in Figure 8. After 72 h, the water uptake of the PS film and FCNs is around 70 and 35 wt%, respectively. After incorporating FCNs into the PS matrix, the water uptake decreased as the FCNs content increased, and it was about 50 wt% for the PS/FCNs-30. Therefore, it can be concluded that the swelling of the material is suppressed in the presence of FCNs within the PS matrix. This phenomenon can be ascribed firstly to the low water uptake of the FCNs itself; and secondly to the presence of strong hydrogen bonding interactions between filler/filler and filler/matrix. Meanwhile, the low glycerol content to the whole material might also be responsible for the reduction of the water uptake.

4. Conclusions

A suspension of cellulose nanocrystals was prepared from flax fibers by acid hydrolysis and used to reinforce the PS matrix with content from 5 to 30 wt% for preparation of nanocomposite materials by a casting method. The SEM images showed that the FCNs fillers dispersed well within the PS matrix and had good adhesion in the interfacial area. The values of T_g ascribed to the starch-rich phase increased with increasing content of FCNs, indicating that the existence of FCNs reduced the flexibility of starch molecular chains. It is worth noting that the tensile strength and Young's modulus of the nanocomposites increased, respectively, from 3.9 to 11.9 MPa and from 31.9 to 498.2 MPa with an increase of FCNs content from 0 to 30 wt%. Meanwhile, the starch-based nanocomposites also show a higher water resistance. The performance improvements of the PS/FCNs nanocomposites may be ascribed to the chemical similarities between starch and cellulose and the hydrogen bonding interactions existing in filler/matrix.

Acknowledgements

This work was financially supported in part by the Agricultural Bioproducts Innovation Program (ABIP) of Canada via Pulse Research Network (PURENET) and Next Generation BioProducts for Health and Wellness Network (NGBHW).

References

[1] Yu L., Dean K., Li L.: Polymer blends and composites from renewable resources. Progress in Polymer Science, **31**, 576–602 (2006).

[2] de Menezes A. J., Pasquini D., Curvelo A. A. S., Gandini A.: Novel thermoplastic materials based on the outer-shell oxypropylation of corn starch granules. Biomacromolecules, **8**, 2047–2050 (2007).

[3] Mohanty A. K., Misra M., Hinrichsen G.: Biofibres, biodegradable polymers and biocomposites: An overview. Macromolecular Materials and Engineering, **276–277**, 1–24 (2000).

[4] Mathew A. P., Dufresne A.: Morphological investigation of nanocomposites from sorbitol plasticized starch and tunicin whiskers. Biomacromolecules, **3**, 609–617 (2002).

[5] Tábi T., Kovács J. G.: Examination of injection moulded thermoplastic maize starch. Express Polymer Letters, **1**, 804–809 (2007).

[6] Santayanon R., Wootthikanokkhan J.: Modification of cassava starch by using propionic anhydride and properties of the starch-blended polyester polyurethane. Carbohydrate Polymers, **51**, 17–24 (2003).

[7] Cao X., Chang P. R., Huneault M. A.: Preparation and properties of plasticized starch modified with poly(ε-caprolactone) based waterborne polyurethane. Carbohydrate Polymers, **71**, 119–125 (2008).

[8] Cao X., Zhang L., Huang J., Yang G., Wang Y.: Structure-properties relationship of starch/waterborne polyurethane composites. Journal of Applied Polymer Science, **90**, 3325–3332 (2003).

[9] Chen Y., Cao X., Chang P. R., Huneault M. A.: Comparative study on the films of poly(vinyl alcohol)/pea starch nanocrystals and poly(vinyl alcohol)/native pea starch. Carbohydrate Polymers, **73**, 8–17 (2008).

[10] Cao X., Zhang L.: Miscibility and properties of polyurethane/benzyl starch semi-interpenetrating polymer networks. Journal of Polymer Science, Part B: Polymer Physics, **43**, 603–615 (2005).

[11] Cao X., Zhang L.: Effects of molecular weight on the miscibility and properties of polyurethane/benzyl starch semi-interpenetrating polymer networks. Biomacromolecules, **6**, 671–677 (2005).

[12] Cao X., Wang Y., Zhang L.: Effects of ethyl and benzyl groups on the miscibility and properties of castor oil-based polyurethane/starch derivative semi-interpenetrating polymer networks. Macromolecular Bioscience, **5**, 863–871 (2005).

[13] Suda K., Kanlaya M., Manit S.: Synthesis and property characterization of cassava starch grafted poly[acrylamide-co-(maleic acid)] superabsorbent via γ-irradiation. Polymer, **43**, 3915–3924 (2002).

[14] Lepifre S., Froment M., Cazaux F., Houot S., Lourdin D., Coqueret X., Lapierre C., Baumberger S.: Lignin incorporation combined with electron-beam irradiation improves the surface water resistance of starch films. Biomacromolecules, **5**, 1678–1686 (2004).

[15] Chen B., Evans J. R. G.: Thermoplastic starch-clay nanocomposites and their characteristics. Carbohydrate Polymers, **61**, 455–463 (2005).

[16] Cao X., Chen Y., Chang P. R., Huneault M. A.: Preparation and properties of plasticized starch/multiwalled carbon nanotubes composites. Journal of Applied Polymer Science, **106**, 1431–1437 (2007).

[17] Šturcová A., Davies G. R., Eichhorn S. J.: Elastic modulus and stress-transfer properties of tunicate cellulose whiskers. Biomacromolecules, **6**, 1055–1061 (2005).

[18] Azizi Samir M. A. S., Alloin F., Dufresne A.: Review of recent research into cellulosic whiskers, their properties and their application in nanocomposite field. Biomacromolecules, **6**, 612–626 (2005).

[19] Dubief D., Samain E., Dufresne A.: Polysaccharide microcrystals reinforced amorphous poly(β-hydroxyoctanoate) nanocomposite materials. Macromolecules, **32**, 5765–5771 (1999).

[20] Wang Y., Cao X., Zhang L.: Effects of cellulose whiskers on properties of soy protein thermoplastics. Macromolecular Bioscience, **6**, 524–531 (2006).

[21] Noshiki Y., Nishiyama Y., Wada M., Kuga S., Magoshi J.: Mechanical properties of silk fibroin-microcrystalline cellulose composite films. Journal of Applied Polymer Science, **86**, 3425–3429 (2002).

[22] Helbert W., Cavaille J. Y., Dufresne A.: Thermoplastic nanocomposites filled with wheat straw cellulose whiskers. Part I: Processing and mechanical behavior. Polymer Composites, **17**, 604–611 (1996).

[23] Chazeau L., Cavaillé J. Y., Canova G., Dendievel R., Boutherin B.: Viscoelastic properties of plasticized PVC reinforced with cellulose whiskers. Journal of Applied Polymer Science, Part B: Polymer Physics, **71**, 1797–1808 (1999).

[24] Ljungberg N., Bonini C., Bortolussi F., Boisson C., Heux L., Cavaille J. Y.: New nanocomposite materials reinforced with cellulose whiskers in atactic polypropylene: Effect of surface and dispersion characteristics. Biomacromolecules, **6**, 2732–2739 (2005).

[25] Cao X., Dong H., Li C. M.: New nanocomposite materials reinforced with flax cellulose nanocrystals in waterborne polyurethane. Biomacromolecules, **8**, 899–904 (2007).

[26] Smeder B., Liljedahl S.: Market oriented identification of important properties in developing flax fibres for technical uses. Industrial Crops and Products, **5**, 149–162 (1996).

[27] Dong X. M., Kimura T., Revol J-F., Gray D. G.: Effects of ionic strength on the isotropic-chiral nematic phase transition of suspensions of cellulose crystallites. Langmuir, **12**, 2076–2082 (1996).

[28] Zhang Y., Han J. H.: Plasticization of pea starch gilms with monosaccharides and polyols. Journal of Food Science, **71**, E253–E261 (2006).

[29] Rindlava A., Hulleman S. H. D., Gatenholma P.: Formation of starch films with varying crystallinity. Carbohydrate Polymers, **34**, 25–30 (1997).

[30] Souza Rosa R. C. R., Andrade C. T.: Effect of chitin addition on injection-molded thermoplastic corn starch. Journal of Applied Polymer Science, **92**, 2706–2713 (2004).

[31] Angles M. N., Dufresne A.: Plasticized starch/tunicin whiskers nanocomposites. 1. structural analysis. Macromolecules, **33**, 8344–8353 (2000).

[32] Lu Y., Weng L., Cao X.: Morphological, thermal and mechanical properties of ramie crystallites-Reinforced plasticized starch biocomposites. Carbohydrate Polymers, **63**, 198–204 (2006).

eXPRESS Polymer Letters Vol.2, No.7 (2008) 511–519
Available online at www.expresspolymlett.com
DOI: 10.3144/expresspolymlett.2008.61

Investigation of the pressure generated in the mould cavity during polyurethane integral skin foam moulding

P. Grőb[*], *J. Marosfalvi*

Department of Machine and Product Design, Budapest University of Technology and Economics, Műegyetem rkp. 3., H-1111 Budapest, Hungary

Received 13 April 2008; accepted in revised form 26 May 2008

Abstract. An industrial scale measuring system was set up to investigate the pressure arising in the mould cavity during polyurethane integral skin foaming. The system is able to measure the pressure arising in the mould cavity and the pressure distribution using a piezoresistive pressure sensor. The pressure distribution was measured at 18 points along the mould surface at constant production parameters. Then six production parameters, which affect the pressure, were investigated in detail with the Taguchi method of experimental design. The results of the design were processed by ANOVA (analysis of variance). Three major influencing parameters were estimated by regression analysis. Finally an equation was developed to give a good estimation to the pressure arising in the mould cavity.

Keywords: *processing technologies, industrial applications, design of experiments, pressure measurement, polyurethane*

1. Introduction

Polyurethane foaming as an empirical technology has predominantly been based on experience up to date. There is little information available about the real foaming process of products, the reaction pressure generated, and its distribution; therefore the design of foaming moulds and their optimization from various aspects – deformation, costs etc. – primarily rely on experience and estimates.

A few people dealt with the pressure generated at foaming previously. Campbell [1] described in detail the way how the pressure develops: in the beginning the blowing agent is in liquid form and dissolved in the mixture. After the chemical reaction starts the temperature increases and when the temperature reaches the boiling point of the blowing agent it starts to evaporate. Due to this the foam starts to expand, it fills the mould cavity. Having finished the mould filling the inner pressure in the foam increases.

Gupta and Khakhar [2] divided the generation of the pressure into three stages: in the first stage there is no foaming, the mixture flows into the mould, the pressure is equal to the atmospheric pressure; in the second stage the foam starts to expand, the density decreases, the pressure is still equal to the atmospheric pressure; the third phase starts when the expanding foam fills the mould cavity completely. In the last phase the density becomes constant and the pressure increases. After the foam reaches the gel-point (the gel-point is the point at which an infinite polymer network first appears), there is no more change in the density. He tried to describe the changes of the pressure in time with the changes of the amount of the blowing agent and the density. Similarly, as Campbell demonstrated, the pressure arises when the foam completely fills the cavity and which coincides with the changes of the density and the amount of the blowing agent.

---

[*]Corresponding author, e-mail: grob.peter@gt3.bme.hu

Beruto *et al.* [3] studied the connection between the blowing agent and the pressure arising in the bubbles of the foam. He calculated a so-called 'foaming power', which was a mechanical work what the foaming system was doing against the enviroment. The foaming power can be calculated with Equation (1):

$$W_e = \Omega \int P_e(t)\mathrm{d}h(t) \tag{1}$$

where W_e is the foaming power [W]; Ω is the volume of the foam [dm^3], $P_e(t)$ is the pressure [N/m^2], $h(t)$ the displacement of the foaming system [m]. He found that, if the amount of the blowing agent decreases, the foaming power will decrease too. If the total amount evaporates, the power becomes zero.

The literature discusses measurements of the pressure generated during foaming at several instances, but none of them have been measured the pressure in the mould cavity directly. Clarke [4] made attempts to determine cycle time from pressure data. He assumed that the changes in the closing pressure of the hydraulic cylinder correspond to the pressure generated in the mould. Vespoli *et al.* [5] built a Kistler pressure transmitter into the mould; however, it was not placed into the mould cavity but at the beginning of the feed bush. He intended to determine the viscosity changes from the pressure changes. He used the value of pressure rise to validate his viscosity function estimate.

Ryan *et al.* [6] built an in-line rheometer with two pressure transducers. The rheometer was placed between the mixing head and the mould to investigate whether the behaviour of the mixture behind the mixing head is Newtonian or not. He found out that it is a good approximation to consider the mixture as a Newtonian fluid and from the pressure-difference the apparent viscosity can be calculated. Kim *et al.* [7] also built a special rheometer to measure the pressure-growth to assess the viscosity. He set up the pressure transducer at the inlet point of the mould. Likewise Vespoli, he used the value of pressure rise to validate his viscosity function estimate. The viscosity calculations are important, because when the mould filling time is longer than the gel-time, a pre-mature gelation occurs, which leads to defective products. From the changes of viscosity the gel-time can be calculated. Yokono *et al.* [8] used his pressure measurement data for validate his simulation of the arising pressure. The simulation is based on the principle of adiabatic compression. Kodama *et al.* [9] built his pressure transmitter into the lateral wall of a large-size mould. He attempted to make inferences from the pressure figure on the expansion of the foam after removal from of the mould.

From the pressure measurements, only Kodama's measurement [9] was performed directly in the mould cavity, but he also performed measurements only at one location. It is important to mention that the primary aim of these works was else than to determine the value and distribution of pressure.

There are only a few publications which contain useful information related to the pressure arising in the mould cavity during polyurethane foaming. The main reason for this can be that the foaming technology is still based on some empirical experience, and the companies do not publish their information. However, in the absence of this experience and information the proper design and the optimizing of the foaming moulds can not be made in advance.

The aim of our work was to set up a measuring system of industrial scale to gain real *in situ* information on the foaming process. The measuring system was made suitable for measuring the reaction pressure and its distribution. We tried to obtain more accurate information on the foaming process.

2. The applied mathematical methods

2.1. The Taguchi method

The Taguchi method, developed by Genichi Taguchi [10], is one of the experimental design methods, based on a fractional factorial design. He simplified and standardized the fractional factorial design method and made it easy to use for everyone. It is intended to select the appropriate, previously specified orthogonal array matrix and then to assign the factors to the appropriate columns according to the specified rules.

In addition to its easy application the greatest advantage of the method is that the results are displayed not only numerically but also illustrated in graphs. In case of examining each factor, e.g. the steeper a curve is, the more significant its impact on the target value. In the same way, interactions can also be examined graphically: by depicting the impact of the two factors in the same graph. It can be observed that there is interaction between them if the curves intersect each other; and if they do not intersect each other, there is no correlation between them in the given range.

2.2. Analysis of variance (ANOVA)

Variance analysis is a statistical method suitable for comparing the expected values of groups with identical standard deviation and Gaussian distribution, also known as ANOVA – generated from the initial letters of its English name: ANalysis Of Variance. So the ANOVA is an extended two sample t-test.

For variance analysis, the H_0 null hypothesis is that the factor does not affect the process. So it can be demonstrated not only what degree of impact the factor has, but also which of the factors examined affect the target function examined and which of them not – as regards the reliability level concerned.

First the sum of squares (S) have to be calculated, then the mean square (or variance) can be considered. Next step is to obtain the variance ratio (F). This F value is compared to the value of the F-test table at the desired confidence level. If the $F<F_{table}$ than the null hypothesis is accepted, so that factor does not affect the process. Finally the percentage contribution (P) is calculated, which is shown the percentage contribution of each factor to the process.

3. Experimental

3.1. The technology of polyurethane foaming

The foaming technology of polyurethanes differs from traditional injection moulding. In general, it is termed RIM according to the English abbreviation (Reaction Injection Moulding). By RIM there are two liquid reactive components, stored separately, which are mixed with high pressure in the mixing head, and then the mixture is poured immediately into the mould. In the mould a chemical reaction starts, the liquid mixture becomes solid foam, simultaneously the foam expands, and then the curing begins in the course of which the product solidifies and takes the shape required [11, 12].

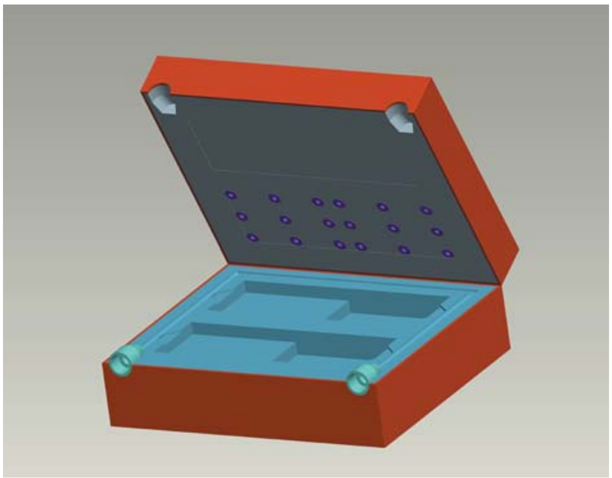

Figure 1. The 3D model of the test mould with staggered mould cavity and the measurement points (purple colour)

3.2. The test-mould

A test-mould for pressure measurements was designed and manufactured in cooperation with Ratipur Ltd., Komló, Hungary. The following requirements were specified for the test mould: the mould should be manufactured according to the industrial technology; the mould should be suitable for testing both flexible, rigid and integral skin foam systems; the specimen should be of ‘industrial’ size; the mould should be suitable for fixing both thermal and pressure sensors; the mould cavity should be suitable to admit inserts to produce different specimens; the mould should be possible to inject from several places and directions; each mould cavity should be sealed separately.

The 3D model of the test mould is shown in Figure 1.

3.3. Pressure measurement

There are 18 measurement points set up uniformly in the mould to measure pressure. These points cover the surface of the entire mould cavity. They were placed with particular care ensuring that measurement points that critical points, e.g. at the step (sudden change in cross-section), or at the edge of the product, should be detected as well.

Measurement points were set up only in the upper part of the mould and only above one of the mould cavities. Figure 2 shows the mould arrangement with the measurement spots.

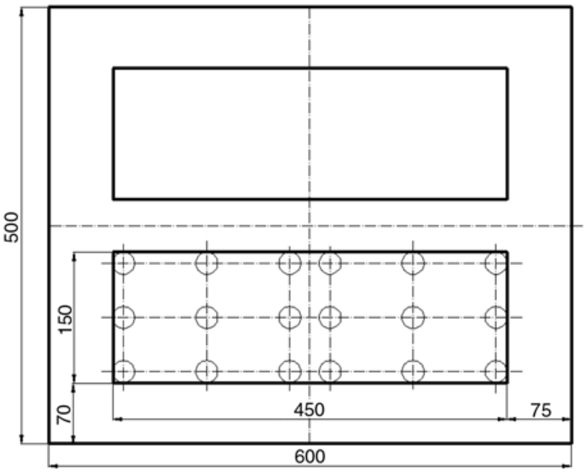

Figure 2. Outline of the arrangement of the test mould and the 18 measurement spots

An insert for sensor was installed to each measurement point. The sensor – type number 4079A by the Kistler Company, it is a piezoresistive type combined heat and pressure sensor developed for the RIM technology – can be placed into this insert. The detected pressure data are transmitted through the cable to the amplifier. The signal boosted by the amplifier gets into an A/D converter; this is required for computerized processing. Finally, the received signal was recorded by the Windaq software of DataQ Instruments Inc.

3.4. The examined material

The examined material is the foam nominated by the code ELASTOFOAM I4703/100/schw, produced by Elastogran Kemipur Ltd. (Hungary). This foam system is suitable for producing flexible integral skin foam products of 400–800 g/dm^3 density and 50–80 Shore A rigidity. The system contains two components: component 'A' is a mixture of polyols, catalyst and other additives, component 'B' is the izocyanate, in this case it is methylene diphenyl diisocyanate (MDI). The cream time, this is the time, when the material volume begins to increase, for this system is 30 sec, the rise time, it is the end of foaming, is 90 sec, the tack-free time, when the foam surface becomes tack-free, equal to the rise time. The density of the freely rising foam is 130 g/dm^3. The blowing agent is n-pentane. The formulation for this foam system is the following: 100 wt% polyol, 53.5 wt% izocyanate, 5.0 wt% n-pentane.

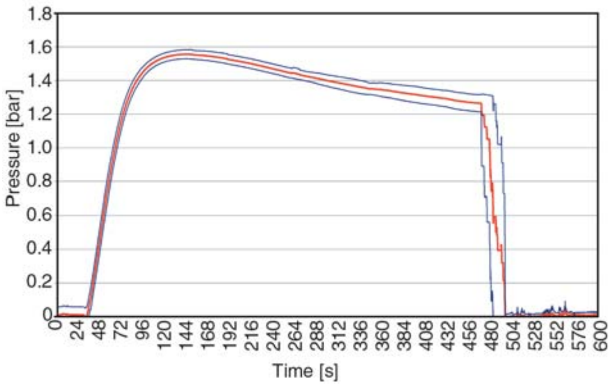

Figure 3. The time vs. pressure curve investigating the pressure distribution

4. Results and discussion

4.1. Pressure distribution

Taking into account that no information was available on the pressure distribution in the mould cavity, first it was examined whether there is a significant difference in the pressure data measured at the 18 measurement points at constant production parameters. The time vs. pressure graph is presented in Figure 3.

The red curve represents the average of 18 measurements; the blue curves represent the standard deviation of the measured data. As it can be seen in the diagram the standard deviation of the data is quite small, it can be concluded that there is no significant difference among the 18 measurement points in terms of the maximum and the runoff of the pressure generated. This also means that pressure distribution is uniform along the surface of the product; it does not depend on geometry of the cavity and the location.

4.2. Estimation of pressure based on empirical data

In the polyurethane foam industry the pressure and the average density are important parameters, so the connection between them is not negligible. The pressure is essential for the mould design; the density is a defined requirement from the customer. The connection between density and pressure is found in the industrial practice as an empirical estimate. An empirical formula for the scale of the pressure generated was recommended by the manufacturer of the foam system. According them the estimated pressure can be calculated with Equation (2):

$$\text{estimated pressure} = \frac{\text{density of the product}}{\text{density of the freely rising foam}}\ \text{[bar]} \qquad (2)$$

The density of the product [g/dm^3] is the ratio of the quantity of material injected and the volume of the mould; and the density of the freely rising foam [g/dm^3] is a technological parameter. The ratio of these two data will yield the estimate of the inner pressure value to affect the mould.

The pressure data were measured during the manufacturing of foam products with different average densities. This information was compared with the estimated ones, this contrast is shown in Figure 4. The red line represent the estimated ones, the black line represent the measured data.

It can be observed in Figure 4 that the lines of estimated and measured pressure data are diverging. The pressure, which is calculated with the empirical formula, is higher than the real pressure value. This means that the moulds designed with this method are overestimated.

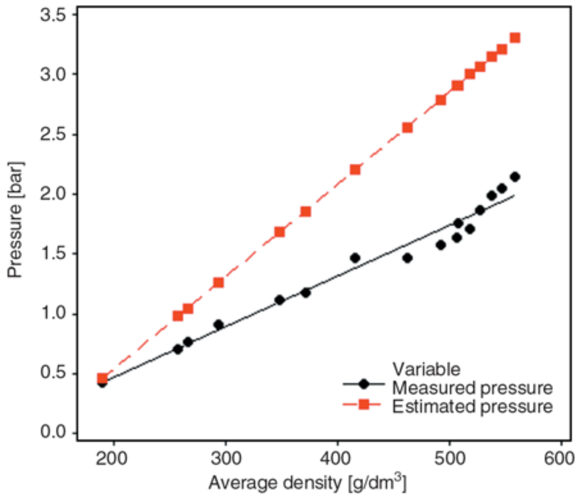

Figure 4. Measured and estimated pressure vs. average density

4.3. Selecting substantial factors

Six technological factors affecting the pressure were investigated. These factors were as follows: mould temperature (MT), temperature of the components (CT), injected mass flow rate (MF), injection time (IT), volume (VO), and the mixing ratio by weight of the polyol and isocyanate (MR). These are the most important factors in the industrial practice.

Our aim is to select the significant factors. These factors were investigated at two levels. Table 1 shows the set of the levels. The engineers of the company provided us with assistance in selecting levels. The design was a 2^{6-1} design with 6 factors and 32 runs.

Figure 5 shows a graphical representation of the results. The steeper the line; the larger the impact of the given factor on the target function – on the maximum value of pressure in the present case. Table 2 contains a numerical presentation of results and the order of the factors.

As it can be seen from Figure 5 and Table 2, the injected mass flow rate (MF) has the greatest impact on the generated pressure; it is followed by the volume of the mould cavity (VO) and the injection time (IT). It can be clearly observed that the impact of these three factors on the target function is much stronger than that of the others. As expected, by increasing the injection time, the injected mass will be increased, and consequently the pressure will also be increased. The same can be observed in case of changing the geometry: higher pressure will be result at lower volume with

Table 1. Levels of the factors to the examination for selecting the substantial factors

	Level 1	**Level 2**
Mould temperature (MT)	35°C	45°C
Temperature of the components (CT)	23°C	29°C
Injection time (IT)	5 s	7 s
Injected mass flow rate (MF)	150 g/s	200 g/s
Volume (VO)	2.53 dm^3	1.69 dm^3
Mixing ratio (MR)	100:51	100:54

Table 2. Numerical presentation of of the six factor’s impact on the pressure

	Mould temperature (MT)	**Temperature of the components (CT)**	**Injection time (IT)**	**Injected mass flow rate (MF)**	**Volume (VO)**	**Mixing ratio (MR)**
Level 1	1.92	1.95	1.67	1.63	1.63	1.99
Level 2	2.09	2.06	2.34	2.38	2.38	2.01
Difference	0.17	0.12	0.67	0.76	0.75	0.02
Order	4	5	3	1	2	6

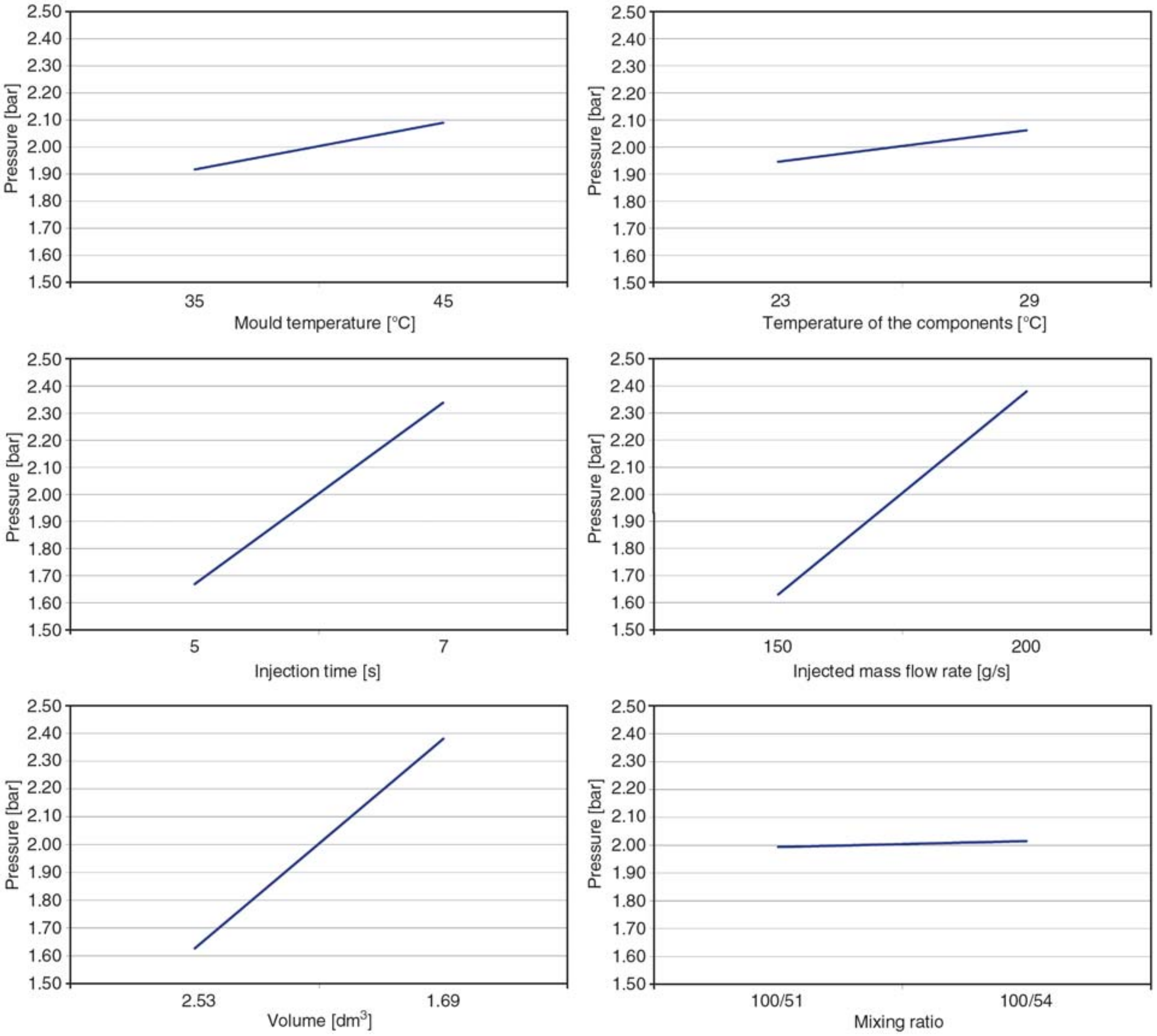

Figure 5. Graphic presentation of the six factor's impact on the pressure

the same mould charge. At the same time, it was found that the pressure decreases by reducing the injected mass flow.

Processing results by variance analysis (ANOVA)

Table 3 contains the ANOVA evaluation of results. Degrees of freedom (f) are a measure of the amount of information that can be uniquely determined from a given set of data. It equals one less that the number of levels. Here the number of levels was two. The total degrees of freedom are equal to the total trial numbers minus one. The number of trials was 32. Sum of squares (S) is a measure of the

Table 3. The ANOVA data table for pressure

	Degree of freedom (f)	**Sum of squares (S)**	**Variance (V)**	**Variance ratio (F)**	**Percentage contribution (P)**
MT	1	0.24	0.24	1.53	1.41
CT	1	0.11	0.11	0.69	0.64
IT	1	3.59	3.59	23.08	21.28
MF	1	4.58	4.58	29.41	27.11
VO	1	4.55	4.55	29.21	26.93
MR	1	0.0036	0.0036	0.023	0.02
Error	25	3.27	0.16	1	22.605
Total	31	16.88	–	–	100

deviation of the experimental data from the mean value of the data. Variance (V) is a quotient of the square sum and the degrees of freedom. Variance measures the distribution of the data about the mean of the data. Variance ratio (F) is used to measure the significance of the factors. It is equal to the quotient of variance of each factor and the variance of the error.

The last column in Table 3 indicates the percentage contribution (P), which was obtained by dividing the sum of squares by the total sum of squares and multiplying the result by 100, of each factor in terms of the entire process. The three major factors (injection time (IT) 21.28%; injected mass flow rate (MF) 27.11%; volume (VO) 26.93%) have totally a 75% impact on pressure. Let us mention that the impact of factors are not taken into consideration is nearly 22%. This means that there are other factors, besides the factors involved in the investigation, which affect the pressure. Thus, it may be considered that further factors should be involved in the investigation to get a more accurate approximation.

By comparing the variance ratios (F) with the value pertaining to 95% reliability ($F_{95}(1.25) = 4.2417$), it can be concluded that only the injection time (IT), injected mass flow rate (MF) and the volume (VO) affect the process.

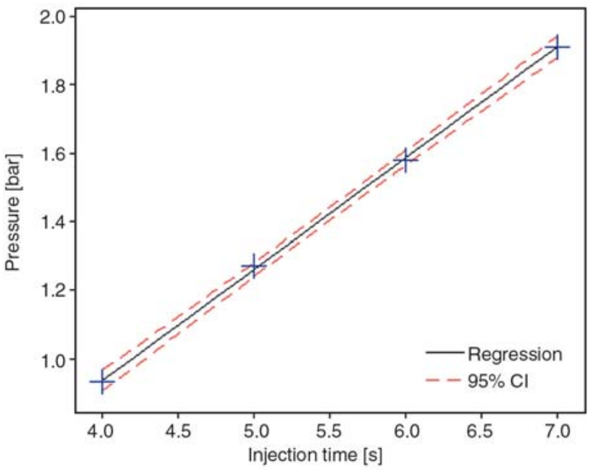

Figure 6. The regression line and the confidence interval for injection time

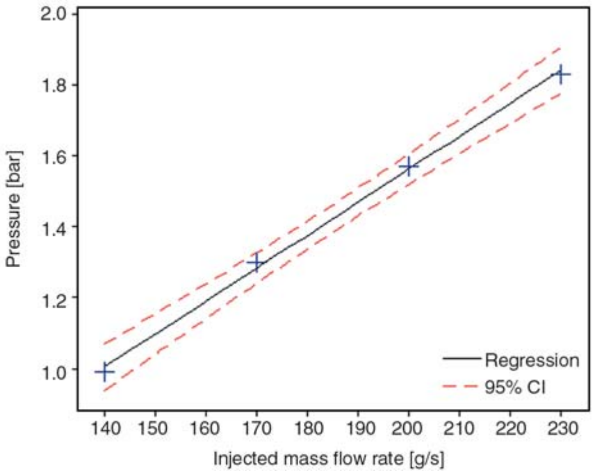

Figure 7. The regression line and the confidence interval for injected mass flow rate

4.4. Estimation of the pressure based on the three main factors

The three main factors (injection time (IT), injected mass flow rate (MF), volume (VO)) were further investigated. Second time a four-level measurement was designed. Table 4 shows the set of the levels.

To the measured points, supposing a linear relation, a regression line was fitted, using the least square method. The regression lines are shown in Figures 6–8. The blue points represent the measured points, the black continuous line is the regression line, and the red dashed line is the line of the confidence interval for 95%.

Table 5 shows the equations of the regression lines and the coefficient of determination. The coeffi-

Table 4. Levels of the factors to the examination for estimation of the pressure

	Level 1	Level 2	Level 3	Level 4
Injection time (IT)	4 s	5 s	6 s	7 s
Injected mass flow rate (MF)	140 g/s	170 g/s	200 g/s	230 g/s
Volume (VO)	2.53 dm^3	2.24 dm^3	1.96 dm^3	1.69 dm^3

Table 5. The equations of the regression lines and the coefficient of determinations

	Equation of the regression line	Coefficient of determination (R^2)
Injection time (IT)	$p = 0.325(\mathrm{IT}) – 0.3650$	0.999
Injected mass flow rate (MF)	$p = 0.0093(\mathrm{MF}) – 0.298$	0.998
Volume (VO)	$p = 0.4216(\mathrm{MF}) – 0.298$	0.997

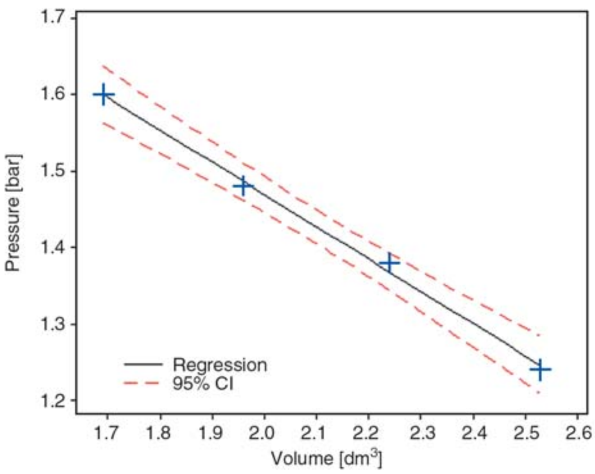

Figure 8. The regression line and the confidence interval for volume

cient of determination indicates the strength of a linear relationship between the line and the points. If the coefficient is close to 1, that means excellent regression estimation.

The value of the pressure (p) is obtained in [bar], if the injection time (IT) is in [s], the injected mass flow rate (MF) is in [g/dm^3] and the volume is in [dm^3]. The equations shown in Table 5. are good approximations of the measured data, because of the values of coefficient of determination are near 1.

The equations in Table 5 are adequate if the values of the other factors are constant. E.g. the pressure can be predicted from the injection time, when the injected mass flow and the volume is invariable. It is hard to achieve in the industry, so a multiple linear regression test was made. This test took into consideration the effects of all factors. Equation (3) shows the result of the multiple linear regression:

$$p = -1.21 + 0.324\cdot(\mathrm{IT}) + 0.00938\cdot(\mathrm{MF}) - 0.422\cdot(\mathrm{VO}) \qquad (3)$$

Coefficient of determination: $R^2 = 0{,}987$.

If the injection time, the injected mass flow rate and the volume of the mould are known, a good estimation can be given with this equation.

5. Conclusions

The pressure generated in the mould cavity during polyurethane integral skin foam moulding was investigated. A test mould was designed and built to measure the maximal pressure arising in the mould cavity and the distribution over the mould surface. It was found that the value of the pressure is the same along the surface of the product; it does not depend on the geometry of the mould cavity. The measurements proved that the empirical correlation used in the polyurethane foam industry for mould design considerably overestimates the moulds in ranges of higher average density. It was established that the three major manufacturing parameters, which have effects on the value of the pressure, are the injected mass flow rate, the injection time and the geometry of the mould cavity. These three production parameters impact on pressure are nearly 75%, the rest 25% go to the other, approximately 15, production parameters. Finally a multiple regression analysis was made, which included the three major factors, to give a good estimation to the pressure arising in the mould. This equation can be used in the mould design instead the empirical correlation, which was demonstrated in our work overestimates the moulds in ranges of higher average density, leads to a better designed mould.

Acknowledgements

The authors are gratefully acknowledged the support of Hungarian Research Found (OTKA T046229) and the Ratipur Ltd., Komló, Hungary.

References

[1] Campbell G. A.: Polyurethane foam process development. A system engineering approach. Journal of Applied Polymer Sciene, **16**, 1387–1402 (1972).

[2] Gupta V. K., Khakhar D. V.: Formation of integral skin polyurethane foams. Polymer Engineering and Science, **39**, 164–176 (1999).

[3] Beruto D. T., Baiardo M., Mezzasalma S. A.: Foaming power, bubble nature, and sample density related to the expansion regime in polyurethane foams. Journal of Materials Synthesis and Processing, **7**, 229–237 (1999).

[4] Clarke W. D.: Foam pressure monitoring as a method of studying demold characteristics of appliance polyurethane insulation foam systems. Journal of Cellular Plastics, **21**, 183–186 (1985).

[5] Vespoli N. P., Albertino L. M., Peterson A. A., Ewen J. H.: Mold filling studies of polyurea RIM systems. Journal of Elastomers and Plastics, **18**, 159–176 (1986).

[6] Ryan J., Coates P. D., Johnson A. F., Hynds J., Patrick P.: Mould flows and post-mixhead rheology studies for poly(urethane-urea)s. Plastics and Rubber Processing and Applications, **13**, 121–127 (1990).

[7] Kim D. S., Garcia M. A., Macosko C. W.: Using mold pressure rise data to obtain viscosity of fast polymerizing systems. International Polymer Processing, **XIII**, 162–171 (1998).

[8] Yokono H., Tsuzuku S., Hira Y., Gotoh M., Miyano Y.: Simulation of foaming process of polyurethane integral skin foams. Polymer Engineering and Science, **25**, 959–964 (1985).

[9] Kodama K., Ryoshi H., Okamura M., Fujita S., Fujita J.: New determination method of flowability and demolding properties in polyurethane rigid molded foams. Journal of Cellular Plastics, **33**, 318–329 (1997).

[10] Roy R. K.: A primer on the Taguchi method. van Nostrand Reinhold Publishing, New York (1990).

[11] Randall D., Lee S.: The polyurethanes book. John Wiley and Sons, New York (2002).

[12] Macosko C. W.: RIM fundamentals of reaction injection molding. Hanser Publishers, Munich (1989).

eXPRESS Polymer Letters Vol.2, No.7 (2008) 520–527
Available online at www.expresspolymlett.com
DOI: 10.3144/expresspolymlett.2008.62

Hybrids of HNBR and in situ polymerizable cyclic butylene terephthalate (CBT) oligomers: properties and dry sliding behavior

J. Karger-Kocsis[1*], *D. Felhős*[1], *T. Bárány*[2], *T. Czigány*[2]

[1]Institute for Composite Materials, University of Kaiserslautern, Erwin Schrödinger Str. 58, D-67663 Kaiserslautern, Germany
[2]Department of Polymer Engineering, Budapest University of Technology and Economics, Műegyetem rkp. 3., H-1111 Budapest, Hungary

Received 2 May 2008; accepted in revised form 10 June 2008

Abstract. A peroxide curable hydrogenated nitrile rubber (HNBR) was modified by cyclic butylene terephthalate oligomer (CBT), added in 100 parts per hundred rubber (phr). CBT polymerization was expected to occur simultaneously with that of the curing of the HNBR rubber (T = 190°C, t = 25 min).

Differential scanning calorimetry (DSC) indicated that only a minor part of CBT has been polymerized (pCBT) in the hybrid. Dynamic mechanical thermal analysis (DMTA) revealed that HNBR formed the continuous whereas (p)CBT the dispersed phase. Mechanical properties (hardness, tensile modulus, ultimate tensile strength and strain, tear strength) of the HNBR and HNBR/CBT were determined and collated. Tribological properties were investigated with pin(steel)-on-plate(rubber) (POP), with roller(steel)-on-plate (rubber) (ROP), with oscillating steel cylinder on rubber plate (Fretting) test configurations. Coefficient of friction (COF) and specific wear rate of the HNBR-based systems were determined. It was found that the resistance to wear increases with CBT hybridization. On the other hand, COF did not change much with CBT content. The friction and wear characteristics strongly depended on the test configurations. The worn surface of the HNBR systems was inspected in scanning electron microscope (SEM) to conclude the typical wear mechanisms. SEM investigation showed that the CBT was predominantly recrystallized from its molten state under the curing conditions set. The well developed prism- and platy-like, micron-scaled CBT crystals were made responsible for the reinforcing effect observed.

Keywords: *rubber, polymer blends and alloys, material testing, cyclic butylene terephthalate (CBT), sliding wear*

1. Introduction

To combine thermoplastics with rubbers via melt blending has been always a preferred topic of research and development works which were mostly fuelled by economical reasons. The related efforts resulted in various types of thermoplastic elastomers (e.g. [1]) from which the thermoplastic dynamic vulcanizates [1–3] acquired considerable market segment. Nowadays, by marketing cyclic butylene terephthalate oligomers (CBT) a further interesting option appeared for rubber / thermoplastic combinations. CBT oligomers, having a melting range of T = 140–150°C, can be polymerized into the corresponding linear polybutylene terephthalate in the presence of suitable catalysts. The temperature of the CBT polymerization is $T \geq 150$°C. The time needed for CBT polymerization depends on the type and amount of the catalyst, it is, however, usually less than 30 min at T = 190°C. Attention should be paid to several peculiarities of the CBT polymerization including its final product. The CBT polymerization is athermic and it can be per-

---

[*]Corresponding author, e-mail: karger@ivw.uni-kl.de

formed even below the melting temperature of the final polybutylene terephthalate ($T_m \approx 225°C$) [4]. The isothermal polymerization ($T \approx 190–195°C$), which is preferentially used, is followed by crystallization. Though some studies quoted that polymerization and crystallization are simultaneous (e.g. [5]) they are more likely consecutive processes [6]. The crystallization of the polymerized CBT, occurring in an undercooled melt at $T \approx 190–195°C$, seems to be a hardly controllable process [6]. The overall crystallinity of the *in situ* polymerized CBT is markedly higher than that of 'traditional' polybutylene terephthalates, produced by polycondensation [5–6]. Due to the above listed peculiarities we are using the abbreviation pCBT instead of the widely used PBT for the in situ polymerized CBT product further on.

Considering the fact that the usual polymerization temperature of CBT is close to the vulcanization temperature of different rubbers, hybrid rubber thermoplastics systems composed of crosslinked rubber and thermoplastic pCBT can be produced. A further benefit of this approach is that CBT, being a solid, powder-like material at ambient temperature can be easily incorporated in rubber mixes using the traditional mixing equipments. Park [7] already filed a patent on how to produce thermoplastic dynamic vulcanizates using CBT. Note that in the related system pCBT forms the continuous whereas the dynamically crosslinked rubber the disperse phase. The new method, exploiting the in situ polymerization of CBT in presence of curable rubber is more straightforward than the traditional dynamic vulcanization using high molecular mass linear polyesters ([8] and references therein).

Recall that the prerequisite of this rubber/thermoplastic combination is that the CBT polymerization is not affected by either the components of the cure recipe or the curing pathway of the rubber.

However, pCBT may be a beneficial polymeric additive for rubbers also when the rubber is 'statically' cured. It means that the CBT is incorporated in the curable rubber and it is polymerized to pCBT simultaneously with the curing of the rubber. The aim of this paper was to check the feasibility of this 'hybridization' using a suitable, high temperature-resistant rubber, namely hydrogenated nitrile rubber (HNBR). It was presumed, that peroxide curing of HNBR does not affect the polymerization of CBT. Next we report on the first results received on the structure, mechanical and sliding wear properties of HNBR/CBT hybrids.

2. Experimental

2.1. Materials

The composition of the peroxide curable HNBR was the following: HNBR (Therban® LT VP/KA 8882 of Lanxess, Leverkusen, Germany; acrylonitrile content: 21%, Mooney viscosity, ML(1+4)100°C = 74) – 100 part; diphenylamine-based thermostabilizer (Luvomaxx CDPA of Lehmann & Voss, Hamburg, Germany) – 1.1 part; zinc-containing mercapto-benzimidazole compound (Vulcanox® ZMB 2/C5 of Lanxess) – 0.4 part, t-butylperoxy-diisopropyl benzene (Perkadox 14-40 B-PD of Akzo-Nobel, Düren, Germany; active peroxide content: 40%) – 7.5 part, MgO – 2 part, triallyl isocyanurate – 1.5 part, ZnO – 2 part. This mix was produced separately and provided by Lanxess. The curing time of this base mix to reach 90% crosslinking was ca. 10 min at $T = 175°C$. This peroxide curable HNBR was mixed with 100 parts per hundred rubber (phr) cyclic butylene terephthalate (CBT® 160, Cyclics Europe, Schwarzheide, Germany) on a two-roll mixing mill (LRM-150BE of Labtech, Bangkok, Thailand) at ca. 40°C by setting a friction ratio of 1.15. Note that this CBT contained already the polymerization catalyst. Curing of the HNBR both in presence and absence of CBT occurred at $T = 190°C$ for 25 min in a laboratory press. Note that the temperature is higher and the time is longer than required for the HNBR alone as being adjusted to the polymerization of CBT [9]. Specimens for the investigations listed below were cut/punched from the compression molded sheets of ca. 2 mm thickness.

2.2. Phase structure

To get some insight in the structure of the HNBR/CBT hybrid differential scanning calorimetry (DSC) and dynamic mechanical thermal analysis (DMTA) tests were run. DSC traces were registered by a DSC device (DSC821e of Mettler Toledo, Giessen, Germany) in a broad temperature range ($T = –100$ to $+260°C$) at a heating and cooling rate of 20°C/min.

DMTA spectra were recorded on rectangular specimens (length × width × thickness = 20 × 10 ×

ca. 2 mm^3) in tension mode as a function of temperature (from –100°C to +100°C) and a frequency of 10 Hz using a Q800 device of TA Instruments (New Castle, DE, USA). Tests were run at a static preload 0.01 N with a superimposed sinusoidal 0.01% strain. Heating of the specimens occurred in a stepwise manner (temperature steps of 5°C were followed by an equilibration period of 3 min at each temperature).

2.3. Property determination

For the density determination the Archimedes principle (buoyancy method with water) was adopted according to ISO 1183. The Shore hardness of the rubbers was determined according to ISO 868 using a hardness measuring device of Zwick (Ulm, Germany). The Martens (earlier termed to universal) hardness (HM) was determined by the ISO 14577-1 (2002) standard using a Shimadzu DUH 202 device with a Vickers-type diamond indenter. Two types of microhardness tests were carried out. In the first case the maximum force and its holding time were 5 mN and 2 second (s), respectively. In the second case the loading- deloading cycle was repeated at the same position of the indenter, and the load was increased in three consecutive steps. The maximum load values during the three steps were 1.6, 3.3 and 5 mN, respectively, with 2 s holding time each. Tensile tests were carried out on 2 mm thick dumbbells (type: S1 according to DIN 53504) on a Zwick 1445 (Ulm, Germany) universal testing machine at a deformation rate of 500 mm/min. From the related stress-strain curves apart from the ultimate properties, the stress values at 100 and 200% elongations (termed M-100 and M-200, respectively) were also read (ISO 37). To determine the tear strength the recommendation of the ISO 34-1 standard was followed, i.e. angle-type specimen with cut was subjected to 500 mm/min deformation rate.

2.4. Sliding friction and wear

Friction and wear characteristics were determined in pin(steel)-on-plate(rubber) (POP) configuration using a Wazau device (Berlin, Germany), in which a steel pin (100Cr6; arithmetical roughness, R_a, less than 1 µm) with a hemispherical tip of 10 mm diameter rotated along a circular path (diameter: 33 mm). The pin was pushed against the rubber plate with a given load. The following parameters were selected for this configuration – normal load: 2 N, sliding speed: 250 mm/s, duration: 1.5 hour (h). Measuring both the normal and the friction force components via a torque load cell the COF values were calculated and monitored during the test.

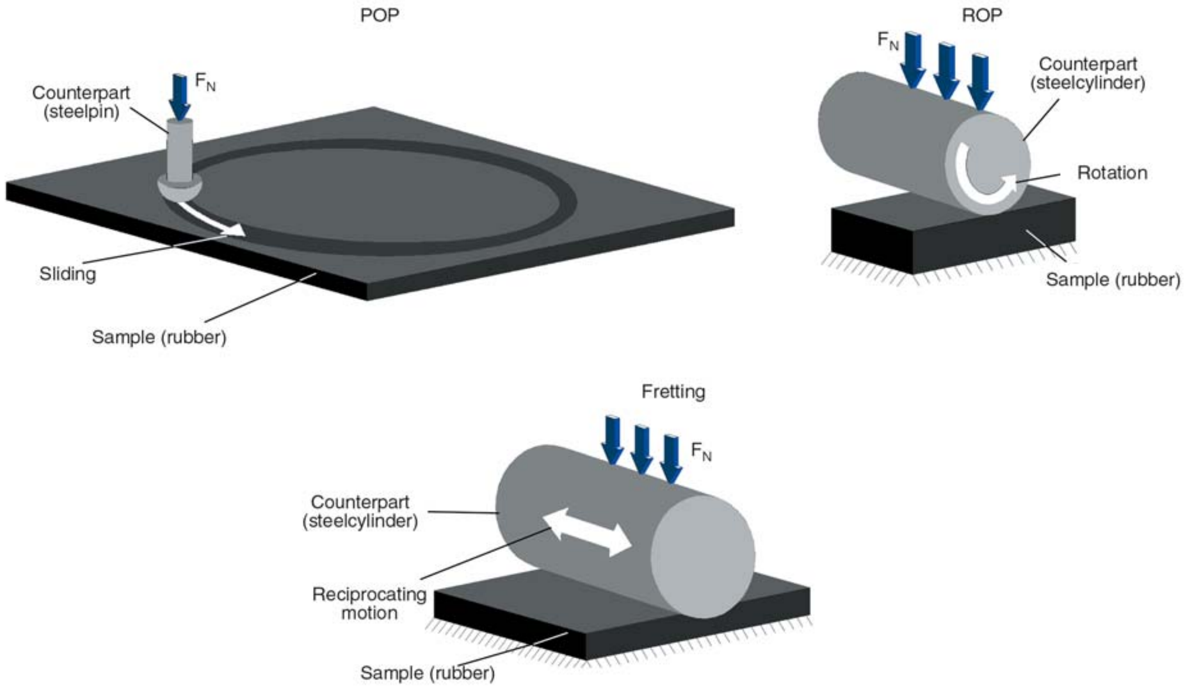

Figure 1. Schematic set-up of the tribotesting devices. Designations: pin(steel)-on-plate(rubber) (POP), roller(steel)-on-plate(rubber) (ROP), oscillating steel cylinder on rubber plate (Fretting)

To study the sliding wear a further test, termed to roller(steel)-on-plate(rubber) and referred to ROP, was also used. A rotating steel roller (9SMnPb28k, diameter: 10 mm, width: 20 mm, $R_a \approx 0.9$ μm) pressed against a rubber strip of 9 mm width in a SOP 3000 tribotester (Dr Tillwich GmbH, Horb-Ahldorf, Germany). The frictional force induced by the torque was measured online and thus the COF was registered during the test. The test parameters were – load: <4 N (varied); sliding speed: 250 mm/s; duration: max. 1.5 h.

In the third tribotest (fretting) a steel cylinder was oscillating on the surface of the fixed rubber specimen. The cylinder was pressed against the rubber with a given load. The diameter and the contact length of the cylinder ($R_a \approx 0.9$ μm) were 15 and 12 mm, respectively. The applied normal load was <30 N (varied), the frequency of the oscillation was set for 10 or 20 Hz (varied), the stroke selected was <5 mm (varied), and the duration of the measurements was 3 h.

The test configurations are depicted schematically in Figure 1.

The specific wear rates were determined by Equation (1):

$$W_s = \frac{\Delta m}{\rho \cdot F \cdot L} \qquad (1)$$

where Δm is the mass loss recorded gravimetrically, ρ is the density, F is the normal force and L is the overall sliding distance.

Worn surfaces of the specimens were inspected in a scanning electron microscope (SEM; JSM5400 of Jeol, Tokyo, Japan). Prior to SEM investigation the specimens were sputtered with an Au/Pd alloy using a device of Balzers (Lichtenstein).

3. Results and discussion

3.1. Phase structure

Figure 2 displays the DSC traces registered during heating (1st, 2nd) and cooling (after 1st heating). The glass transition (T_g) step of the HNBR is well resolved at $T \approx -25$°C during the 1st heating. The next step at $T \approx 60$°C should be assigned to the T_g of pCBT. Note that neither CBT [10] nor HNBR shows any thermal transition at $T \approx 60$°C. So, CBT is likely polymerized, however, did not crystallize. This is quite surprising, but in line with recent results claiming that pCBT crystallization is of stochastic nature [6]. In the subsequent temperature range two melting peaks can be found: at $T \approx 130$°C and $T \approx 220$°C. The first one should be assigned to the melting of the unpolymerized CBT, whereas the second one to the melting of the pCBT formed. The small exotherm at $T \approx 105$°C may be linked with the cold crystallization of (p)CBT. During subsequent cooling the pCBT crystallizes at $T \approx 165$°C. As the related enthalpy value is markedly higher (13.6 J/g) than that of the melting from the 1st heating (<1 J/g), one should presume that pCBT has been formed during the 1st heating instead of the HNBR curing process. Note that such peculiar thermal behaviour was already reported for the in-situ bulk polymerization of CBT [10, 11].

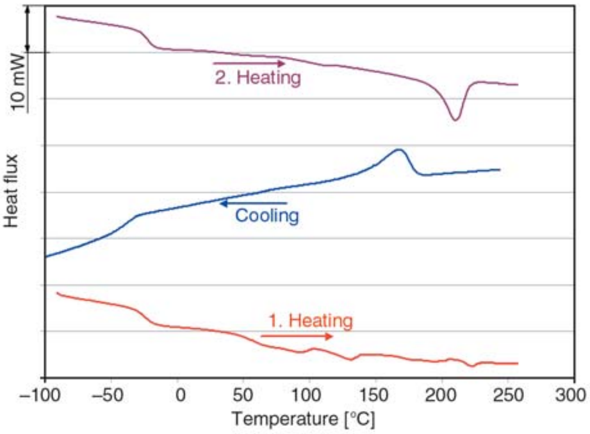

Figure 2. DSC traces registered on the HNBR/(p)CBT hybrid during heating and cooling

The 2nd heating curve displays again the T_g of HNBR. On the other hand, the T_g step of the pCBT can hardly be resolved. This is due to the high crystallinity of the pCBT present. The melting peak of pCBT can be found at $T \approx 215$°C in accord with the expectation. The crystallization (cooling) and melting enthalpies (13.8 J/g in the 2nd heating) are closely matched.

The DMTA curves in Figure 3 give further insight in the phase structure. The fact that the storage modulus (E') vs. temperature shows only one drop, viz. at the T_g of HNBR, substantiates that HNBR forms the continuous whereas (p)CBT the disperse phase. The designation (p)CBT considers that likely a small portion of CBT polymerized and its major fraction remained unpolymerized under the HNBR curing cycle. This, suggested by the DSC tests, will be corroborated by further results later. Nonetheless, (p)CBT works as an active filler of

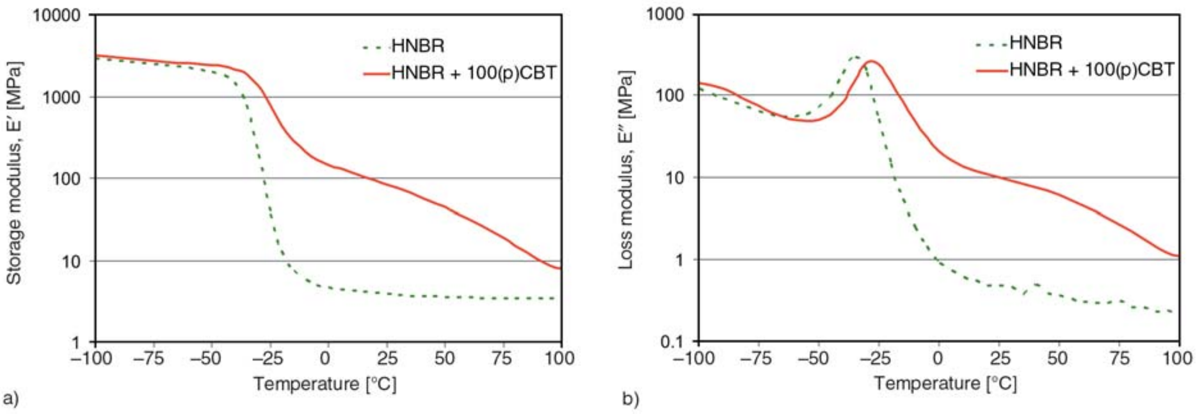

Figure 3. E' vs. T (a) and E'' vs. T (b) traces for the HNBR and HNBR/(p)CBT hybrid

Table 1. Comparison of the properties of HNBR and HNBR/(p)CBT

	HNBR	HNBR + 100(p)CBT
tanδ at the actual T_g of HNBR [1]*	1.360	0.337
Density [g/cm^3]	1.057	1.137
Shore A hardness	42	82
Martens hardness, HM [MPa]	1.45	18.1
M-100 [MPa]	1.3	3.4
M-200 [MPa]	2.7	4.4
Tensile strength [MPa]	4.4	9.6
Strain at break [%]	280	467
Tear strength [kN/m]	4.2	33.6
E-modulus at 0.01% strain from DMTA at T = 25°C [MPa]	4	84

*Note: the T_g of the HNBR (–25°C) increased in presence of (p)CBT (–19°C)

thermoplastic nature. The latter is reflected by the steady decrease of E' with increasing temperature. That is the reason why no plateau modulus appears. The ‘active’ filler character of (p)CBT is well reflected by the enhanced E' compared to that of the plain HNBR (of Figure 3a). Note that the T_g peak of the HNBR, when read at the peak position of the E'' vs. T trace, shifted toward higher temperatures in presence of (p)CBT (cf. Figure 3b and Table 1). This means that the segmental motion of HNBR has been hampered by the (p)CBT present. Considering the fact that this experimental HNBR contains some acrylate moieties, grafting between HNBR and (p)CBT is most likely to occur, namely via transreactions. This would explain the observed shift in the T_g. The less developed shoulder at $T \approx 50$°C in the E'' vs. T trace of the hybrid may be a further hint for this kind of grafting which affects the chain mobility. Note that the T_g relaxation of the amorphous pCBT should appear in this range, too.

3.2. Hardness and mechanical properties

Figure 4 shows the load vs. penetration depth curves of the microhardness measurement for three consecutive loadings. In contrast to HNBR, the relative residual deformation is higher for the hybrid after this test series. This is due to the plastic deformability of the amorphous pCBT and due to the break-up crystal clusters of recrystallized CBT

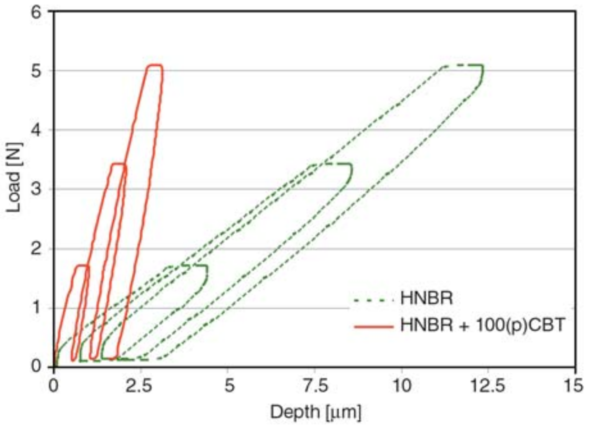

Figure 4. Load vs. penetration depth curves for three consecutive loading/deloading cycles during microhardness measurements on the systems studied

(the latter will be explained later). Note that this behaviour may strongly influence the sliding wear under POP conditions, where recovery effects are of great importance.

The hybridization was associated with considerable increase in both Martens and Shore A hardness values (cf. Table 1). Characteristic stress-strain curves for HNBR and HNBR/(p)CBT are shown in Figure 5. Interestingly, incorporation of CBT increased both ultimate stress and strain simultaneously, i.e. this material worked as an active filler.

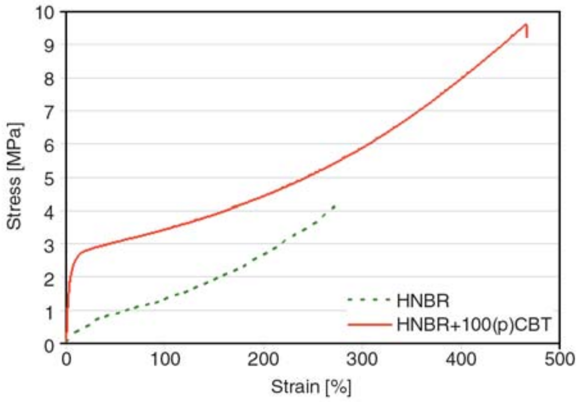

Figure 5. Comparison of the stress vs. strain behavior of HNBR and HNBR/(p)CBT hybrid

HNBR/(p)CBT hybrid outperformed HNBR in respect to the tear strength, as well. Results of the hardness and mechanical tests are summarized in Table 1.

3.3. Friction and wear

Figure 6a shows the steady-state COF of the HNBR and HNBR/(p)CBT hybrid as a function of the tribotests. One can notice a marginal decrease in the COF due to CBT modification for both POP and ROP, while the opposite trend appears for fretting. The specific wear rate of HNBR was reduced by CBT hybridization under both POP and ROP conditions (in the latter case more prominently). On the other hand, an adverse tendency was observed for fretting.

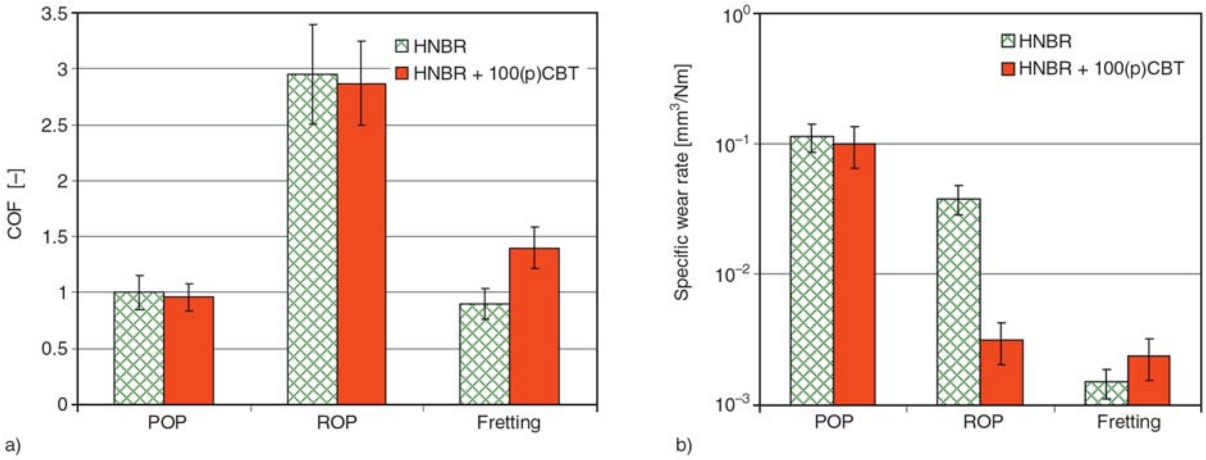

Figure 6. Measured steady-state coefficient of friction (COF) values (a) and specific wear rate data (b) in the POP, ROP and fretting tests

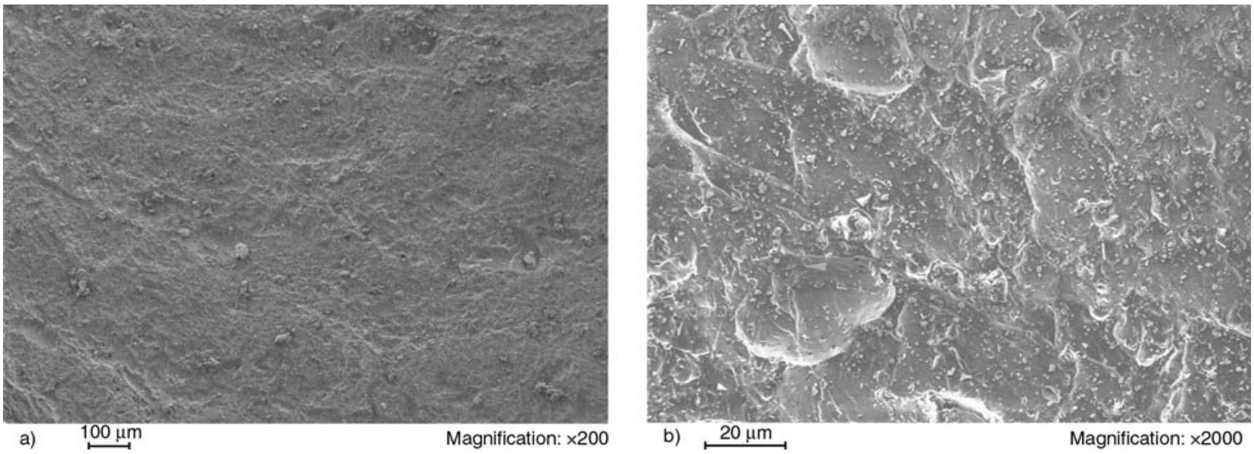

Figure 7. SEM pictures taken from the wear track of plain HNBR after POP test. Note: sliding direction is downwards. (Magnification: a – ×200, b – ×2000)

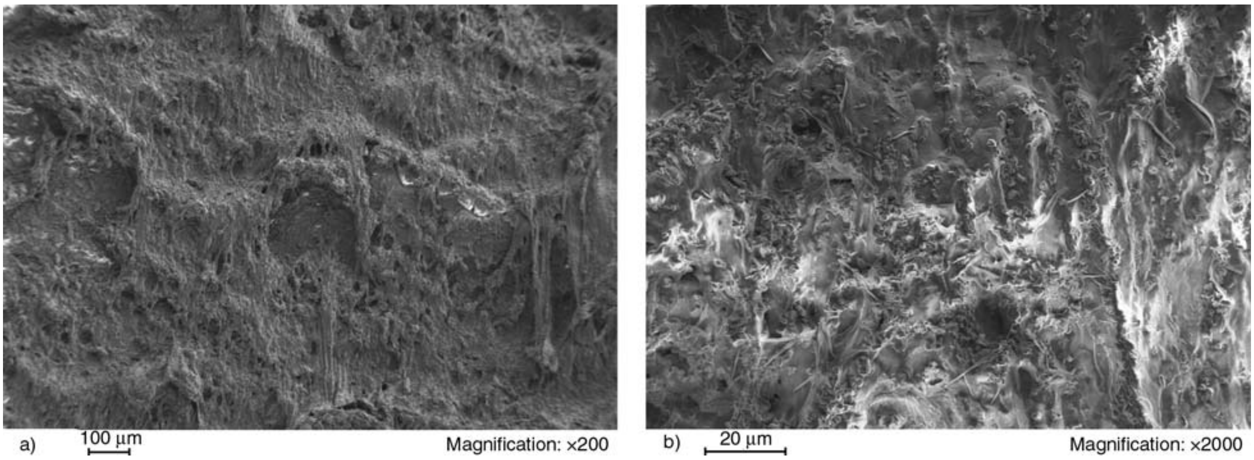

Figure 8. SEM pictures taken from the wear track of HNBR/(p)CBT after ROP test. Note: sliding direction is downwards. (Magnification: a – ×200, b – ×2000)

The wear mechanisms were elucidated for the systems after POP tests. The wear track of the plain HNBR showed that debris were chipped off, generating some craterlike structure – cf. Figure 7. Note that this is the usual failure mode under sliding wear for unfilled rubbers ([12] and references therein). The worn surface after POP became more rough in presence of (p)CBT (cf. Figure 8). This is in line with the change observed for the COF data. On the other hand, the worn surface of the HNBR/(p)CBT reveals that prominent 'plastic type' deformation occurred. Fibrils, remnants of a disrupted fibrillar structure, being elongated to the sliding direction, are indicators of this plastic deformation. Recall, that this is supported by the formation of amorphous pCBT and also in accord with the break-up of CBT crystal clusters, the existence of which will shown later. Moreover this failure mode could be predicted based on results of the cyclic microhardness tests. Nevertheless, chipping phenomena are still discernible on the worn surface (cf. Figure 8a). High magnification SEM picture (cf. Figure 8b) may hint for effects of locally emerging high flash temperatures. This may cause the polymerization and crystallization of CBT and pCBT, respectively, in analogy with the DSC results (cf. Figure 2). The high magnification SEM picture in Figure 9 delivers the strongest argument for the fact that CBT practically did not polymerize under the curing schedule of HNBR. In the worn surface well developed, micron-scale crystals of plate and prism shapes are well resolved. They should have been formed via recrystallization from the CBT melt. Recall that the CBT melting range is between T = 140–150°C, whereas that of the HNBR curing was T = 190°C in this case. So, if CBT did not polymerize, then it had to recrystallize from the melt during the cooling period after curing. The related large crystals of high aspect ratio worked as reinforcing filler in the HNBR. We have further proofs for the above scenario. Preliminary results from extraction (using chloroform, which already at ambient temperature completely dissolves CBT unlike pCBT) and wide-angle X-ray scattering (WAXS) experiments support that only a very small portion of CBT has been polymerized under the cure conditions set.

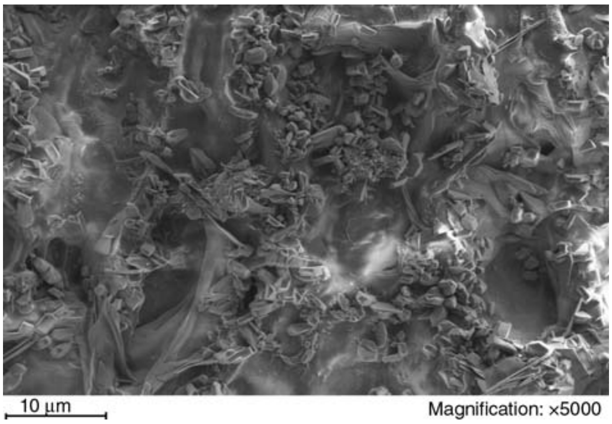

Figure 9. SEM picture taken from the worn surface of HNBR/(p)CBT after POP test (Magnification: ×5000)

This observation is of great practical relevance due to the following aspects. First, incorporation of CBT, even if it does not polymerize under the curing conditions of rubber, may strongly improve the flow behaviour of the related rubber. Recall that the melting temperature of CBT is lower than the usual cure temperature of rubbers and its melt viscosity is very low [9]. Second, the subsequent recrystallization of CBT – during cooling of the cured rubber – results in the formation of microscopic crystals and crystal agglomerates which have high aspect ratio, and thus may work as efficient reinforcements in rubbers. The prerequisite of the latter is a good interfacial bonding between the rubber and (p)CBT. It has to be clarified next how the necessary interfacial bonding between (p)CBT and other rubbers can be achieved.

4. Conclusions

In this work HNBR/CBT hybrids were produced by incorporating cyclic butylene terephthalate oligomers (CBT) in a peroxide-curable HNBR. The CBT, added in 100 parts per hundred parts rubber (phr) amount, was dispersed in the HNBR matrix. According to DSC results the majority of the CBT did not polymerize under the curing of the HNBR rubber. On the other hand, CBT is still able to undergo polymerization/crystallization when the HNBR/CBT hybrid is heated and/or hold above the melting temperature of polybutylene terephthalate. Instead of polymerization, the CBT was molten during the HNBR curing. In the follow-up cooling of HNBR the CBT recrystallized into micron-scaled crystals of high aspect ratio. This was the major reason for the improvements in both mechanical properties and resistance to dry sliding. So, the CBT crystals worked as active filler particles of thermoplastic nature and improved the mechanical and tribological performance of the HNBR prominently. Incorporation of CBT affected the coefficient of friction (COF) only slightly (being dispersed in the HNBR matrix) by contrast to the specific wear rate. The specific wear rate was markedly reduced under POP and ROP testing, whereas it increased in fretting test for the hybrid compared to the plain HNBR.

Acknowledgements

This work was performed in the framework of a bilateral cooperation between Hungary and Germany (MöB and DAAD) and an integrated project of the EU (KRISTAL; Contract Nr.: NMP3-CT-2005-515837; www.kristal-project.org). The authors are thankful to Dr. M. Mezger (Lanxess) for providing the HNBR along with additional remarks to this topic.

References

[1] Legge N. R., Holden G., Schroeder H. E.: Thermoplastic elastomers. Hanser, München (1987).

[2] Coran A. Y., Patel R. P.: Thermoplastic elastomers by blending and dynamic vulcanization. in 'Polypropylene: Structure, Blends and Composites' (ed.: Karger-Kocsis J.) Chapman and Hall, London, Vol 2, 162–201 (1995).

[3] Karger-Kocsis J.: Thermoplastic rubbers via dynamic vulcanization. in 'Polymer Blends and Alloys' (eds.: Shonaike G. O., Simon G. P.) Marcel Dekker, New York, 125-153 (1999).

[4] Brunelle D. J.: Synthesis and polymerization of cyclic polyester oligomers. in 'Modern Polyesters' (eds.: Scheirs J., Long T. E.) Wiley, Chichester, 117–142 (2003).

[5] Parton H., Baets J., Lipnik P., Goderis B., Devaux J., Verpoest I.: Properties of poly(butylene terephthalate) polymerized from cyclic oligomers and its composites. Polymer, **46**, 9871–9880 (2005).

[6] Harsch M., Karger-Kocsis J., Apostolov A. A.: Crystallization-induced shrinkage, crystalline, and thermomechanical properties of in situ polymerized cyclic butylene terephthalate. Journal of Applied Polymer Science, **108**, 1455–1461 (2008).

[7] Park E. H.: Dynamic vulcanization of elastomers with in-situ polymerization. US Patent 7351769, USA (2008).

[8] Papke N., Karger-Kocsis J.: Thermoplastic elastomers based on compatibilized poly(ethylene terephthalate) blends: Effect of rubber type and dynamic curing. Polymer, **42**, 1109–1120 (2001).

[9] Mohd Ishak Z. A., Gatos K. G., Karger-Kocsis J.: On the in-situ polymerization of cyclic butylene terephthalate oligomers: DSC and rheological studies. Polymer Engineering and Science, **46**, 743–750 (2006).

[10] Karger-Kocsis J., Shang P. P., Mohd Ishak Z. A., Rösch M.: Melting and crystallization of in-situ polymerized cyclic butylene terephthalates with and without organoclay: A modulated DSC study. Express Polymer Letters, **1**, 60–68 (2007).

[11] Mohd Ishak Z. A., Shang P. P., Karger-Kocsis J.: A modulated DSC study on the in situ polymerization of cyclic butylene terephthalate oligomers. Journal of Thermal Analysis and Calorimetry, **84**, 637–641 (2006).

[12] Karger-Kocsis J., Felhős D.: Friction and sliding wear of 'nanomodified' rubbers and their coatings: Some new developments. in 'Tribology of Polymeric Nanocomposites' (eds.: Friedrich K., Schlarb A. K.) Elsevier, Amsterdam, 304–324 (2008).

eXPRESS Polymer Letters Vol.2, No.7 (2008) 528–538
Available online at www.expresspolymlett.com
DOI: 10.3144/expresspolymlett.2008.63

Polystyrene/calcium phosphate nanocomposites: Contact angle studies based on water and methylene iodide

S. P. Thomas[1,2], *S. Thomas*[1*] , *R Abraham*[3], *S. Bandyopadhyay*[4]

[1]School of Chemical Sciences, Mahatma Gandhi University, P. D. Hills P.O., Kottayam-686560, Kerala, India
[2]Visiting Research Associate, School of Materials Science and Engineering, University of New South Wales, Sydney-2052, Australia
[3]Department of Physics, St. Dominic's College, Kanjirappilly, Kottayam, Kerala, India
[4]School of Materials Science and Engineering, University of New South Wales, Sydney-2052, Australia

Received 27 April 2008; accepted in revised form 15 June 2008

Abstract. Polystyrene (PS) based nanocomposites were prepared by melt mixing in a Brabender Plasticoder with calcium phosphate as the nanofiller. These nanocomposites showed improvement in almost all physical properties. Contact angle measurements of the composites with water and methylene iodide were carried out. Various contact angle parameters such as total solid surface free energy, work of adhesion, interfacial free energy and spreading coefficient were analysed. The interaction parameter between the polymer and the liquids has been calculated using the Girifalco-Good's equation.

Keywords: *nanocomposites, polystyrene, calcium phosphate, contact angle measurements*

1. Introduction

Nanocomposites are a new class of polymer materials with an ultrafine phase dispersion of the order of a few nanometers that shows very interesting properties often very different from those of conventional filled polymers [1–4]. The presence of these nanoparticles improves the elastic modulus without decreasing the elongation at break and does not worsen the rheological and processing behavior and the optical properties of the polymer matrix. The main problem in the preparation of nanocomposites in the molten state [5–7] is the good filler dispersion the polymer matrix. All properties have been measured considering a possible use of these new materials for several different applications.

Contact angle measurements are often used as an empirical indicator of 'wettability' and interfacial tension. True contact angle determination of a liquid–solid–vapor system satisfies Young's equation, where the wetting tension (γ_{lv} cosθ) is equivalent to the solid surface tension (γ_{sv}) minus the liquid–solid interfacial tension (γ_{lv}) [8]. However, in most cases the contact angle exhibits hysteresis for advancing and receding liquids is due to the roughness and heterogeneity of a solid surface [9–11]. Therefore, in practical usage, the measured angle is always considered an 'apparent' contact angle. The most popular method for direct measurement of the static contact angle is the sessile drop method, where the angle is determined from the tangent made to the drop curvature at the base.

For polymer production where particulates or fibers are used for reinforcement, colorant, flame retardancy or stability, understanding the wetting phenomena has considerable value in relation to the material performance. Lowering the free energy of the system, the polymer chains must preferentially interact with the filler surface, where wettability

---

[*]Corresponding author, e-mail: sabut@sancharnet.in and sabut552001@yahoo.com

plays a dominant role in successfully achieving the desired structure [12, 13]. Park and Jin studied the effects of silane coupling agent treatments on the fiber surface properties in terms of the surface energetics of the fibers and the mechanical interfacial properties, including Interlaminar Shear Strength (ILSS) and fracture toughness (K_{Ic}), of the unsaturated polyester composites [14]. Saihi *et al.* performed the wettability studies on polyethylene terephthalate (PET) fibres according to the Wilhelmy method [15]. They obtained qualitative and quantitative indications about the degree of the water and oil repellency and of the surface free energy of the grafted surface. Yeh et al studied the contact angle behaviour of the Acrylonitrile butadiene styrene (ABS) clay nanocomposites very recently [16]. Contact angle of water on the ABS–clay nanocomposite materials increased with respect to the increase in clay content.

Several other reports on the wetting phenomena on the polymer nanocomposites appeared in the literature recently [17–21]. Here our aim was to study the wetting behaviour of the polystyrene/calcium phosphate nanocomposites with respect to water and methylene iodide. This study focuses on the effect of weight percentage of nanofiller on wetting characteristics such as work of adhesion, total surface free energy, interfacial free energy and spreading coefficient.

2. Experimental

2.1. Materials

Atactic polystyrene was obtained from Polychem Bombay, India. The specific properties of the polymer are denoted in Table 1.

2.2. Nanoparticle preparation

The nanosized calcium phosphate filler particles were synthesized using in situ deposition technique in the presence of polyethylene oxide (PEO) as follows: Firstly, a complex of calcium chloride ($CaCl_2$) with PEO was prepared in desired proportions in methanol. An appropriate stoichiometric amount of trisodium phosphate in distilled water was added to the above complex slowly without stirring. The whole mixture was allowed to digest at room temperature for 24 h when both the chloride and phosphate ions diffused through the PEO and formed a white gel like precipitate, which was filtered, washed and dried. The concentrations of PEO-$CaCl_2$ complex were varied in the range from 2:1, 4:1, 8:1, 16:1 and 32:1 (molar ratio) respectively. The yield of the calcium phosphate was recorded as 83 and 62% for 4:1 and 16:1 ratios respectively. The method of nanoparticle synthesis is given in Figure 1. The particle size was measured by X-ray diffractogram and transmission electron microscopy techniques. X-ray diffractograms of the particles were measured using Philips 1140 X-ray irradiation apparatus using CuK_α radiation with $\lambda = 1.5406$ Å at room temperature. TEM images of the particles and composites were measured by Philips CM200 field emission gun TEM using thin transparent sections. Nanoparticles with ~10 nm size was used for further studies (these were prepared by taking PEO and $CaCl_2$ in the ratio 2:1).

Table 1. Characteristics of polystyrene

Property	Value
Density [g/cc]	1.04–1.065
Poisson's ratio	0.33
Solubility parameter [$(cal/cm^3)^{1/2}$]	18.6
Water absorption (ASTM)	0.05%
Softening temperature [°C]	108°C
Molecular weight (M_w)	218000

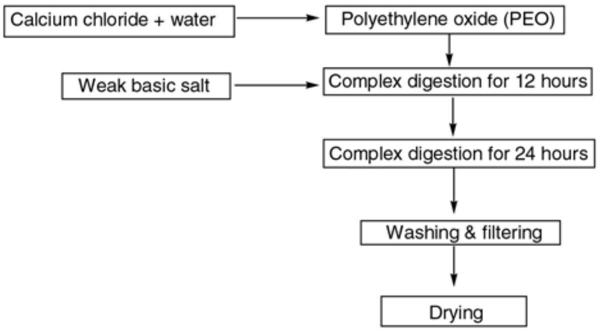

Figure 1. Schematic representation of the nanoparticle synthesis

2.3. Nanocomposite preparation

The nanoparticles were incorporated into polystyrene by melt blending technique using a Brabender Plasticoder at 200°C with varying filler amount as 1, 3, 5, 7 and 10 wt%. The various composites are designated as P0, P1, P3, P5, P7 and P10 respectively.

2.4. Contact angle measurements

Contact angle measurements were carried out in a FTA 100 Series (First Ten Angstroms, Portsmouth, Virginia 23704 USA). Measurements were carried out with water (triply distilled) and methylene iodide (Kemphasol, Bombay) on samples of size $1\times1\times2$ cm^3 at room temperature. The volume of the sessile drop was maintained as 5 µl in all cases using a microsyringe. The contact angle was measured within 45–60 s of the addition of the liquid drop with an accuracy of ±1°. Measurements were repeated six to ten times with different test pieces of the same sample to check the accuracy. Also contact angles were measured with definite time intervals for a single drop and the measurements were recorded as snap shots.

2.5. Theory and calculations

It is well known that the knowledge of surface energetics at a given temperature of a solid has recently allowed significant progress in many academic and scientific fields involving two, not identical, molecular interactions at a certain intermolecular distance, such as adsorption (gas–solid), wettability (liquid–liquid), and adhesion (solid–solid) [22, 23]. The basic equation relating the surface free energy of a solid (γ_s) and that of the liquid in contact with the solid (γ_l), the interfacial free energy between the solid and the liquid (γ_{sl}), and the contact angle (θ) is due to Young [24]. It is given by Equation (1):

$$\gamma_l \cos\theta = \gamma_s - \gamma_{sl} \tag{1}$$

In Equation (1), γ_s and γ_{sl} are not amenable to direct measurement. Plot of $\cos\theta$ against the surface tension for a homologous series of liquids, γ_l, can be extrapolated to give a critical surface tension, γ_c, at which $\cos\theta = 1$ [25]. γ_c has been taken as an approximate measure of the surface energy, γ_s, of the solid. However, a limitation of this consideration is that the precise value of γ_c depends on the particular series of liquids used to determine it.

A more appropriate method has been presented by Fowkes considering solid dispersion forces using a geometric mean equation [26]. Later, Owens and Wendt [27] and Kaelble [28] modified Fowkes equation further by also assuming the polar attraction forces which also included the hydrogen bonding forces. Wu [29] has found a still better agreement to obtain γ_s when he used a harmonic mean equation which combines both the dispersion and the polar forces. Wu's approach has been quite satisfactoriy verified by several authors [30–34]. In order to verify Wu's approach, two liquids of dissimilar polarity are selected. Water and methylene iodide have been reported to be a useful pair of liquids for obtaining γ_s of polymers [35]. Wu's harmonic mean equations for water and methylene iodide are written by Equation (2):

$$(1+\cos\theta_w)\gamma_w = 4\left[\frac{\gamma_w^d\gamma_s^d}{\gamma_w^d+\gamma_s^d}+\frac{\gamma_w^p\gamma_s^p}{\gamma_w^p+\gamma_s^p}\right] \tag{2}$$

and by Equation (3):

$$(1+\cos\theta_m)\gamma_m = 4\left[\frac{\gamma_m^d\gamma_s^d}{\gamma_m^d+\gamma_s^d}+\frac{\gamma_m^p\gamma_s^p}{\gamma_m^p+\gamma_s^p}\right] \tag{3}$$

where the subscripts d and p stand for contributions due to dispersion and polar forces respectively. Data for water and methylene iodide were taken from the literature [27].

Water: $\gamma_w = 72.8$ mJ/m^2, $\gamma_w^d = 21.8$ mJ/m^2,
$\gamma_w^d = 51.0$ mJ/m^2
Methylene iodide: $\gamma_m = 50.8$ mJ/m^2,
$\gamma_m^d = 49.5$ mJ/m^2,
$\gamma_m^p = 1.3$ mJ/m^2

γ_s^d and γ_s^p for different compositions of nanocomposites were determined by solving Equations (2) and (3) with the help of a C programme.

The total solid surface free energy is represented by Equation (4):

$$\gamma_s = \gamma_s^d + \gamma_s^p \tag{4}$$

The work of adhesion, W_A, was calculated using Equation (5):

$$W_A = (1+\cos\theta)\gamma_l \tag{5}$$

where γ_l is the surface tension of the liquid used for the contact angle measurement.

The interfacial free energy, γ_{sl}, was calculated from Dupré's Equation (6) [35]:

$$\gamma_{sl} = \gamma_s + \gamma_l - W_A \tag{6}$$

The spreading coefficient, S_c, was determined from Equation (7) [35]:

$$S_c = \gamma_s - \gamma_{sl} - \gamma_l \tag{7}$$

Girifalco-Good's interaction parameter,ϕ, between the polymer and the liquid was determined using Equation (8) [36]:

$$\phi = \frac{\gamma_l(1+\cos\theta)}{2(\gamma_l\gamma_s)^{\frac{1}{2}}} \quad (8)$$

3. Results and discussion

3.1. Nanoparticle characterization

Nanoparticles of calcium phosphate were characterized by XRD as well as TEM techniques. Figure 2(a–f) corresponds to the XRD patterns of nanoparticles obtained, (a) corresponds to the calcium phosphate without PEO and (b–f) for calcium phosphate with PEO concentration from 2:1 to 32:1 respectively. In the figure, there are a number of crystalline forms reported for calcium phosphate existing in both anhydrous and hydrated states. The calcium phosphate without any polymer shows 3 types of phases. Most of the peaks in diffraction patterns correspond to βcalcium orthophosphate (major phase) while the minor phase contains calcium orthophosphate primary along with small amount of calcium metaphosphate hydrate respectively. With increase of PEO concentration, there occurs a suppression of peaks in the diffraction patterns compared to curve a. A large number of peaks are suppressed and peaks at 2θ of 31.9° broaden with increase of PEO concentrations from 42 to 89%. Only two peaks are clearly seen. The peak at 31.9° corresponds to all the three states ($Ca_3(PO_4)_2$, $Ca_3(H_2PO_4)_2$, $Ca_3(PO_3)_2 \cdot 3H_2O$) and at 25.1° corresponds to the minor phase $Ca_3(H_2PO_4)_2$. It is interesting to note the extent of broadening, from 42 to 89%. This shows the small size of crystals, which could be associated with a good molecular level mixing. Thus on comparing curve a with curve b to f in Figure 2, it is obvious that the effect of polymer plays a prominent role in the structure and growth behaviour of calcium phosphate crystals (in the curves the *y* axis indicates the intensity). Since

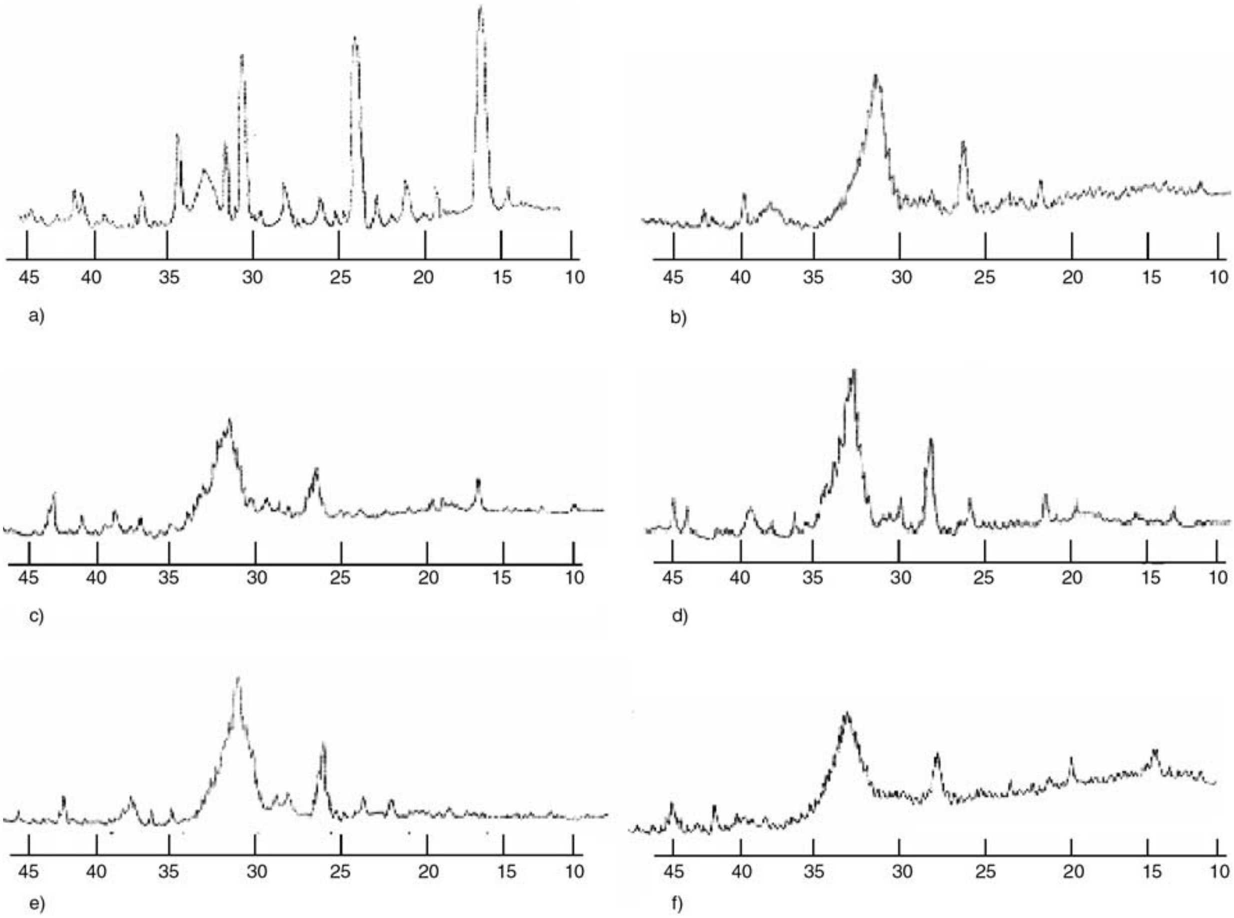

Figure 2. XRD patterns for the calcium phosphate nanoparticles (a) Calcium Phosphate without PEO. The PEO: $CaCl_2$ ratio in (b) 2:1, (c) 4:1, (d) 8:1 (e) 16:1 and (f) 32:1 (in the *x* axis 2θ and in *y* axis intensity is plotted)

$CaCl_2$ is first complexed with PEO, only certain crystalline phases of calcium phosphate are allowed to grow as compared to a large number of phases getting developed in normal free precipitation. From the XRD patterns, the crystallite size was calculated using Scherrer formula, see Equation (9):

$$d[\text{Å}] = \frac{k\lambda}{\Delta 2\theta \cdot \cos\theta} \tag{9}$$

where k is the order of reflection, λ is 1.542 Å, the diffraction angle and $\Delta 2\theta$ is the full width at half maximum (FWHM). As the concentration of the PEO increases the particle size decreases. The corresponding data obtained from XRD measurements is given in Table 2.

The TEM images of the particles are shown in Figures 3(a–c), which are taken for ratios of 2:1, 4:1 and 32:1 respectively. The particles were made a suspension in alcoholic medium and the images were taken after laying the particles on a copper grid. The alcohol evaporated and the particles could be seen clearly in the images. The particle size distributions for each concentration were calculated using image analyzer software. On an average 400 particles were measured at a time to calculate the particle size distribution. The distribution was found to be narrow. The particle size reduction against concentration of PEO is shown in Figure 4. The particle size reduction is attributed to the increase in the amount of oxygen atoms available from PEO matrix as we increase the concentration [37]. The reaction between calcium and phosphate ions is taking place in the 'oxygen cage' available from the PEO molecules. On increasing the concentration of the PEO molecules the number of oxygen atoms increases which will increase the amount of 'oxygen cage' considerably. This enables the suppression of the formed particles and reduces the size further. The yield of the calcium phosphate was recorded as 83 and 72% for 4:1 and 16:1 ratios respectively. Calcium phosphate nanoparticles obtained with the concentration ratio 4:1

Table 2. XRD values for the calcium phosphate nanoparticles

(PEO: $CaCl_2$)	FWHM (2θ) radians	Particle size (L) nm
Calcium phosphate (a)	0.00174	82.4
2:1 (b)	0.0134	10.65
4:1 (c)	0.0156	9.24
8:1 (d)	0.0162	8.96
16:1 (e)	0.0176	8.02
32:1 (f)	0.0181	7.82

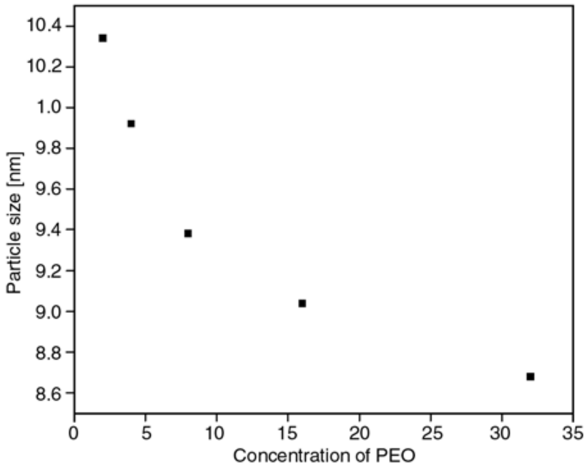

Figure 4. Effect of PEO concentration on particle size of calcium phosphate

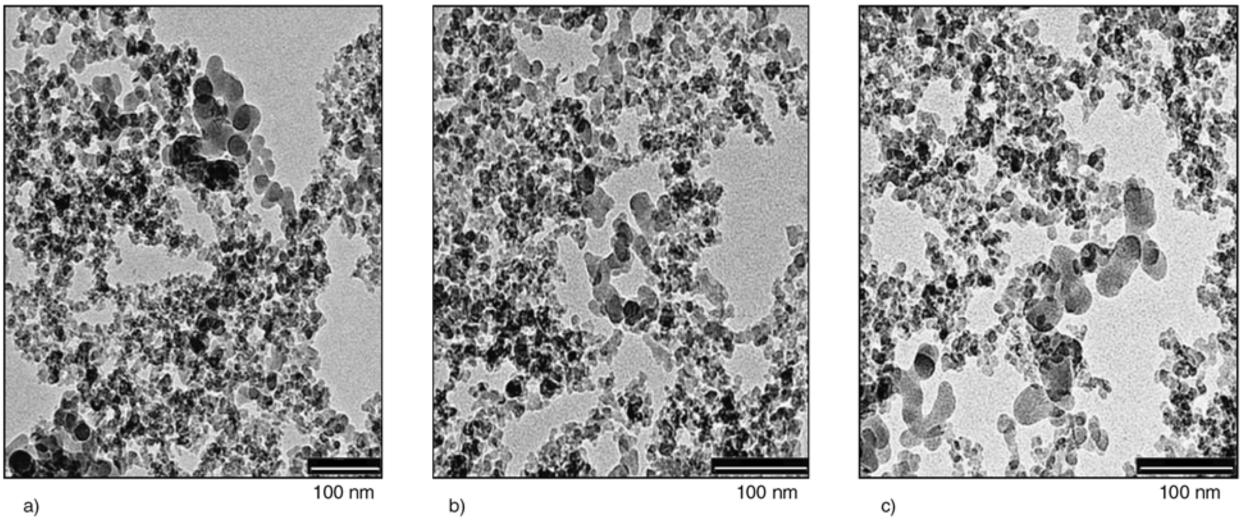

Figure 3. TEM image of the calcium phosphate nanoparticles (PEO: $CaCl_2$, (a) 2:1, (b) 4:1, (c) 32:1)

(particle size approximately 10 nm) were exclusively used for this study.

3.2. Characterization of composites

TEM images of the thin sections of the composites were analysed to see how the particles are dispersed in the matrix for the composites with 3, 5, 7 and 10% respectively (Figure 5(a–d)). TEM will be required to tell if nano-dispersion has been achieved. Generally, the low magnification images indicate how well-dispersed the filler is, while the high magnification images permits the identification of an intercalated or delaminated morphology in polymer nanocomposites. It is quite clear that filler is well distributed in all the styrenic polymers from the TEM images. Discrete particles of nano fillers were seen in the initial compositions (Figure 5(a and b)). Good dispersion of fillers in to the matrix can be seen for the lower concentrations. However, it can be seen from the images, as the concentration of the filler increased, the efficient incorporation is lacking mainly due to the filler agglomeration. We can see that the particles get agglomerated upon increasing the amount of filler.

3.3. Contact angle measurements

Contact angle measurements of nanocomposites of polystyrene with calcium phosphate were done at room temperature with water and methylene iodide as the liquids. Various parameters from these measurements were calculated. At first, the contact angles were measured for each specimen for at least six to ten times. The average is taken as the contact angle for the particular specimen. Figure 6 shows the representative pictures of the measurements with methylene iodide as the liquid. In 6(a) the contact angle for the neat polystyrene is given and 6(b), (c) and (d) represents the same for P3, P5 and P10 respectively. Here the tilt angle is always kept as 0 and an average of the left hand side and right hand side contact angles is given as the true contact angle. In most of the measurements the left and right hand side values are similar. The measurements were done at room temperature with respect to the filler loading. For water the neat polymer show a contact angle equal to 90°. While increasing the filler content the contact angles decreased to around 78° as shown in Figure 7. Polystyrene is basically a hydrophobic polymer and thus the high value of contact angle is justifiable. Calcium phos-

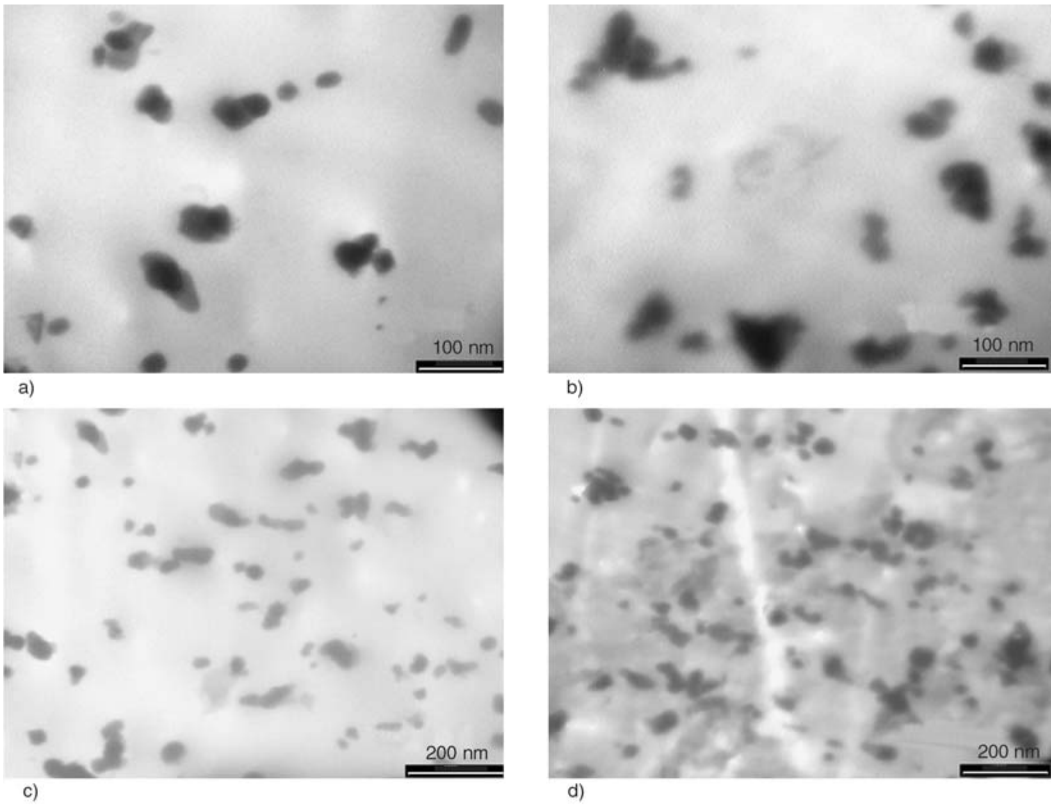

Figure 5. TEM images of polystyrene nanocomposites: a) P3, b) P5, c) P7 and d) P10 (a and b magnification is 100 nm, c and d magnification is 200 nm)

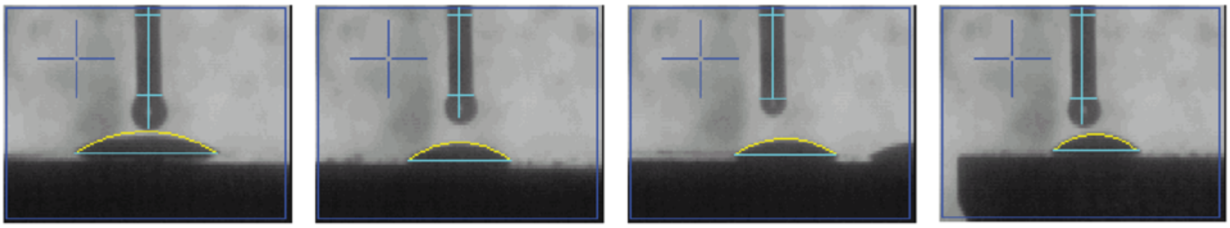

a) (32.93) b) (38.69) c) (36.05) d) (43.69)

Figure 6. Representative figures of contact angle measurements of (a) P0 (b) P3 (c) P5 and (d) P10 with methylene iodide as liquid. Corresponding contact angles are given in parenthesis

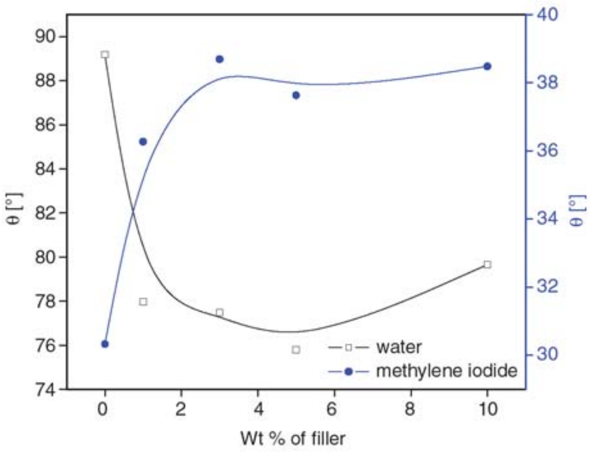

Figure 7. Variation of contact angle of water and methylene iodide with respect to filler loading

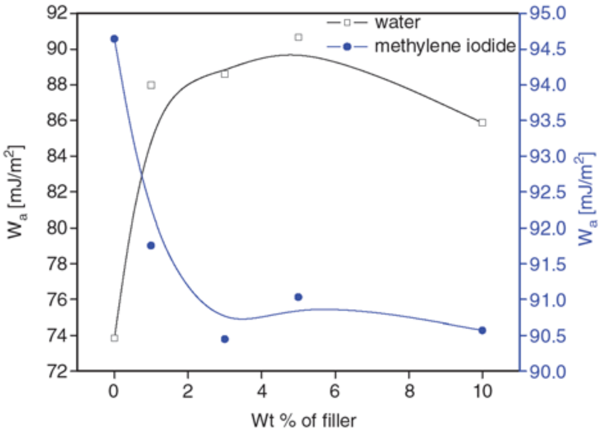

Figure 8. Variation of work of adhesion of water and methylene iodide with respect to filler loading

phate incorporation into the matrix decreases the contact angle. This means that the hydrophilicity is increased for polystyrene. The surface of the composites contains some of the nanofillers added and this eventually decreased the hydrophobic nature. But the amount of fillers has not much effect on the contact angle. For all the composites the contact angles remains almost constant around 78°. In the case of methylene iodide also the hydrophilic nature of the matrix increases. For the neat polymer surface the contact angle is around 30°. On the addition of nanofillers it increased to around 38° for all compositions. Both these results complement each other.

The work of adhesion, W_A, for the nanocomposites for both liquids is shown in Figure 8. W_A is actually the work required to separate the solid and liquid depends solely on the contact angle and the surface tension of the liquid. Thus the W_A for water increases and for methylene iodide shows the reverse trend. The magnitude of difference between the neat polymer and the nanocomposites are much higher for water compared to methylene iodide. Generally the work of adhesion can be correlated to the filler matrix interaction of filler with a liquid comparable with the matrix polymer. Here we try to correlate the work of adhesion of the nanocomposites with the filler matrix interaction even though the liquids selected do not mimic the virgin polymer completely. The TEM figures showed the efficient dispersion of nano fillers up to 5 % and agglomeration for 10% loading (Figure 5(a–d)). Thus the effective dispersion of nanofillers into the matrix might have caused increase in the work of adhesion which is the work required to separate the liquid from the solid surface.

Figure 9 shows the variation in total solid surface free energy, γ_s, with respect to the filler loading. When we increase the filler loading the total solid surface free energy increases which means that the wetting of liquids is high compared to the neat specimens. Also the dispersive and polar components were calculated by solving the harmonic mean equations given earlier. For neat PS the γ_s value was 46.3 and it increased up to 48.6 for the 5% filled composites. This means that the nature of the forces acting on the surface of the composites is different. From Table 3, we can see that the γ_s^d values decreased compared to the neat polymer for all

Table 3. Surface free energy and Girifalco-Good's interaction parameter of the nanocomposites

Composites	γ_s^d	γ_s^p	γ_s	ϕ_w	ϕ_m
P0	41.7	4.5	46.3	0.63	0.97
P1	38.9	9.2	48.1	0.74	0.93
P3	37.9	9.6	47.5	0.75	0.92
P5	38.3	10.2	48.6	0.76	0.91
P10	38.0	8.6	46.7	0.73	0.93

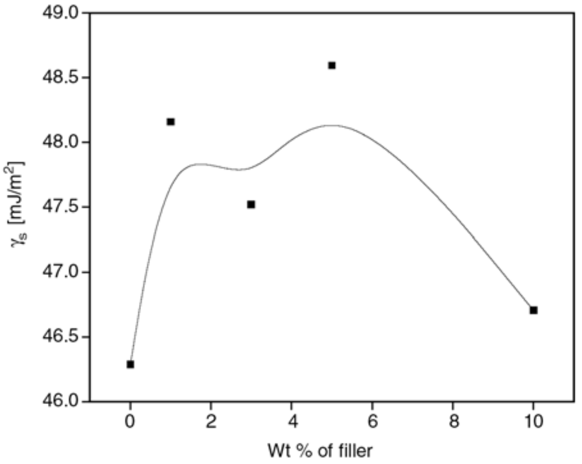

Figure 9. Variation of total solid surface free energy with respect to filler loading

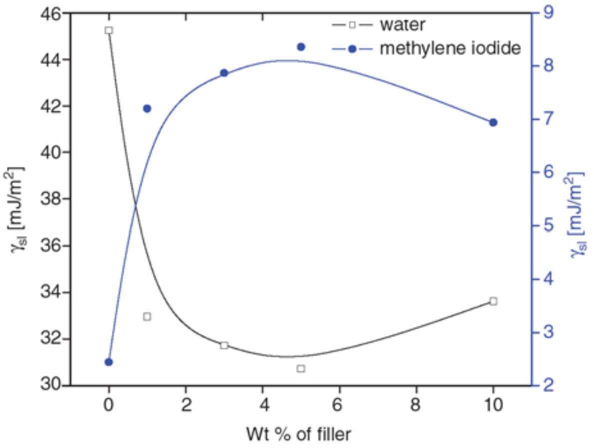

Figure 10. Variation of interfacial free energy of water and methylene iodide with respect to filler loading

compositions while γ_s^p values show much difference from neat matrix. The polar forces acting on the surface of the composites increased compared to the neat polymer and thus the total solid surface free energy increased. Again for the 10% filled systems the γ_s^p value is slightly lower compared to other filled compositions, which accounted for the decrease in the total solid surface free energy. The filler dispersion in the polymer matrix may also have affected the surface properties. Here the initial loadings have good dispersion behaviour while particle agglomeration occurred in the higher loading. This might have caused the decrement in γ_s^p values for the 10% loading. So the hydrophilic nature of the composites became more prominent with the nanofiller addition. On the whole, the γ_s values show not much difference for all the compositions.

The interfacial free energy between the polymer surface and the test liquids, water and methylene iodide, were calculated and the curves are shown in Figure 10. The behaviour of the curves is just opposite to each other as one is polar and the other is non-polar. For water, γ_{sw}, decreases with respect to the filler loading and shows a minimum for 5% filled system. For methylene iodide, γ_{sm}, increase from the neat sample, reaches a maximum for 5% filled systems and decrease for the higher filled systems.

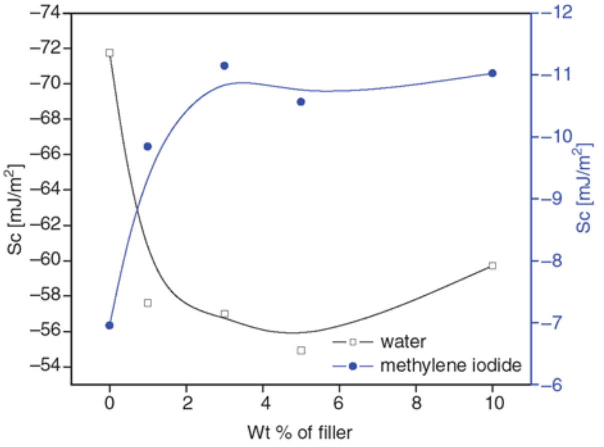

Figure 11. Variation of spreading coefficient of water and methylene iodide with respect to filler loading

In Figure 11 the spreading coefficient of the liquids; according to Equation (7); with respect to the filler loading is given. If the value is positive, the implication is that the liquid will spontaneously wet and spread on a solid surface and if it is negative the lack of wetting and spreading can be ascertained. This means the existence of a finite contact angle ($\theta>0$). From Figure 11, we can deduce that as we increase the filler content the spreading coefficient values for water become less negative and for methylene iodide the reverse is true. Thus, the wetting increased for water with the addition of fillers indicating more hydrophilic nature. In the case of methylene iodide spreading coefficient became more negative and wetting will be difficult on the surface. Comparing water and methylene iodide, the less negative value is given by methylene iodide, which means that it is a better wetting agent for the current composites.

In order to understand the degree of interaction between the test liquid and polymer surface, Girifalco-Good's interaction parameter was calculated using the Equation (8) and the values are given in Table 3. Generally a higher value indicates greater interaction and vice versa. ϕ_w and ϕ_m are the Girifalco-Good's interaction parameters due to water and methylene iodide, respectively. From the values one can see that the interaction between methylene iodide and polymer surface is more compared to water and the surface. For water as we increase the filler loading the parameter show increase and for methylene iodide the interaction parameter show a slight decrease. Thus, for the polar liquid the interaction between the polymer surface and liquid increase while the opposite is shown for the non-polar liquid. This is can be evidenced also from Figure 10 showing the behaviour of interfacial free energy of the composites for both the liquids.

The variation of the contact angle of water with time on the surface of the neat PS and nanocomposites were analysed. The curves are shown in Figure 12. All curves show similar behaviour. In the initial region we can see a sharp decrease in contact angle. Thereafter the contact angles regularly decrease and after a long time it levels off. The surface of the specimens and the liquid have some interaction over a time of period and after reaching a saturation point the value becomes constant. The surface free energy of polymers and polymer composites decays due to the conformational alterations and surface restructuring as the contact time of the liquid increases [38, 39]. Lavielle and Schultz [38] have noted in acrylic grafted polyethylene samples undergo surface free energy changes when it is in long-time contact with water. In this case γ_s^d initially increased and then decreased, γ_s^d whereas decreased continuously with the contact time. In this context, the filler addition in PS may also bring about some surface restructuring. In addition to this the presence of carbon dioxide in the atmosphere may also affect the lowering of contact angles. Also the presence of filler particles on the surface may lower the contact angle over a period of time.

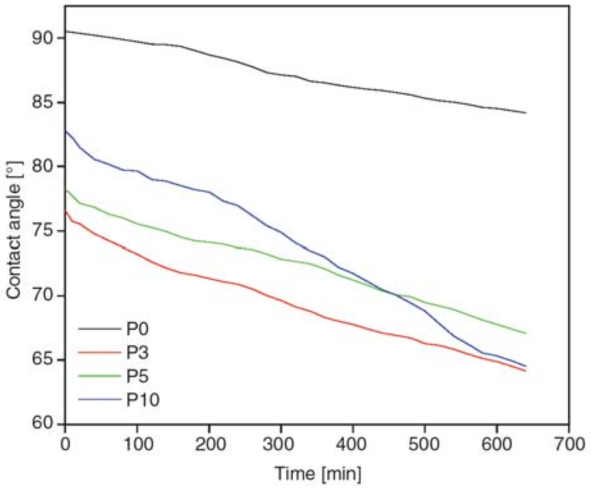

Figure 12. Variation contact angle of water with respect to time

4. Conclusions

Polymer induced crystallization technique is employed to prepare nanoparticles of calcium phosphate with spherical morphology. The particles were incorporated in polystyrene by the melt blending technique. The transmission electron microscopic studies of the composites revealed good dispersion upto 5% of the filler loading. Contact angle measurements of polystyrene/calcium phosphate nanocomposites with water and methylene iodide were studied to know surface properties of the composites. The contact angles for water got decreased while the reverse trend was shown by methylene iodide. The hydrophilic nature of the composites increased with the addition of nanofillers due to presence of fillers on the surface. The solid surface free energy of the composites decreased and thereby increases the work of adhesion. The interaction between the liquid and solid surface became high compared to the neat polymer. With respect to time the contact angle of water decreased for sometime and leveled off which indicated some interaction between the surface and water. Methylene iodide showed less negative value for the spreading coefficient than water and it is a good wetting agent than water. Finally the particle dispersion in the matrix affected the various parameters analysed as each one of them changed according to the filler loading. Other physical and chemical properties will be undertaken to evaluate the viscoelastic and thermal behaviour of composites.

References

[1] Rozenberg B. A., Tenne R.: Polymer-assisted fabrication of nanoparticles and nanocomposites. Progress in Polymer Science, **33**, 40–112 (2008).

[2] Wu Y-P., Zhang L-Q., Wang Y-Q., Liang Y., Yu D-S.: Structure of carboxylated acrylonitrile-butadiene rubber (CNBR): Clay nanocomposites by co-coagulating rubber latex and clay aqueous suspension. Journal of Applied Polymer Science, **82**, 2842–2848 (2001).

[3] Krishnamoorti R., Vaia R. A., Giannelis E. P.: Structure and dynamics of polymer-layered silicate nanocomposites. Chemistry of Materials, **8**, 1728–1734 (1996).

[4] Zanetti M., Lomakin S., Camino G.: Polymer layered silicate nanocomposites. Macromolecular Materials and Engineering, **279**, 1–9 (2000).

[5] Vaia R. A., Giannellis E. P.: Lattice model of polymer melt intercalation in organically-modified layered silicates. Macromolecules, **30**, 7990–7999 (1997).

[6] Liu L. M., Qi Z. N., Zhu X. G.: Studies on nylon 6/clay nanocomposites by melt-intercalation process. Journal of Applied Polymer Science, **71**, 1133–1138 (1999).

[7] Kato M., Usuki A., Okada A.: Synthesis of polypropylene oligomer- clay intercalation compounds. Journal of Applied Polymer Science, **66**, 1781–1785 (1997).

[8] Kwok D. Y., Lin R., Mui A. W., Neumann A. W.: Low-rate dynamic and static contact angles and the determination of solid surface tensions. Colloids and Surfaces, A: Physicochemical and Engineering Aspects, **116**, 63–67 (1996).

[9] Kwok D. Y., Neumann A. W.: Contact angle interpretation in terms of solid surface tension. Colloids and Surfaces, A: Physicochemical and Engineering Aspects, **161**, 31–38 (2000).

[10] Grundke K., Bogumil T., Gietzelt T., Jacobasch H-J., Kwok D. Y., Neumann A. W.: Wetting measurements on smooth, rough and porous solid surfaces. Progress in Colloid and Polymer Science, **101**, 58–67 (1996).

[11] Kamusewitz H., Possart W.: Wetting and scanning force microscopy on rough polymer surfaces: Wenzel's roughness factor and the thermodynamic contact angle. Applied Physics, A: Materials Science and Processing, **76**, 899–904 (2003).

[12] Vaia R., Ishii H., Giannelis E. P.: Synthesis and properties of two-dimensional nanostructures by direct intercalation of polymer melts in layered silicates. Chemistry of Materials, **5**, 1694–1696 (1993).

[13] Manias E., Chen H., Krishnamoorti R., Genzer J., Kramer E. J., Giannelis E. P.: Intercalation kinetics of long polymers in 2 nm confinements. Macromolecules, **33**, 7955–7966 (2000).

[14] Park S-J., Jin J-S.: Effect of silane coupling agent on interphase and performance of glass fibers/unsaturated polyester composites. Journal of Colloid and Interface Science, **242**, 174–179 (2001).

[15] Saihi D., El-Achari A., Ghenaim A., Caze C.: Wettability of grafted poly(ethylene terephthalate) fibers. Polymer Testing, **21**, 615–618 (2002).

[16] Yeh J-M., Chen C-L., Huang C-C., Chang F-C., Chen S-C., Su P-L., Kuo C-C., Hsu J-T., Chen B., Yu Y-H.: Effect of organoclay on the thermal stability, mechanical strength, and surface wettability of injection-molded ABS-clay nanocomposite materials prepared by melt intercalation. Journal of Applied Polymer Science, **99**, 1576–1582 (2006).

[17] Rogers K., Takacs E., Thompson M. R.: Contact angle measurement of select compatibilizers for polymer-silicate layer nanocomposites. Polymer Testing, **24**, 423–427 (2005).

[18] Rahimi A., Gharazi S., Ershad-Langroudi A., Ghasemi D.: Synthesis and characterization of hydrophilic nanocomposite coating on glass substrate. Journal of Applied Polymer Science, **102**, 5322–5329 (2006).

[19] Chen X., You B., Zhou S., Wu L.: Surface and interface characterization of polyester-based polyurethane/nano-silica composites. Surface and Interface Analysis, **35**, 369–374 (2003).

[20] Robinette E. J., Palmese G. R.: Synthesis of polymer-polymer nanocomposites using radiation grafting techniques. Nuclear Instruments and Methods in Physics Research, Section B: Beam Interactions with Materials and Atoms, **236**, 216–222 (2005).

[21] Wu T-M., Wu C-W.: Surface characterization and properties of plasma-modified cyclic olefin copolymer/layered silicate nanocomposites. Journal of Polymer Science, Part B: Polymer Physics, **43**, 2745–2753 (2005).

[22] Park S. J.: Interfacial forces and fields: Theory and applications. Marcel Dekker, New York (1999).

[23] Israelachvili J.: Intermolecular and surface forces. Academic Press, London (1992).

[24] Young T.: An essay on the cohesion of fluids. Philosophical Transactions of the Royal Society of London, **95**, 65–87 (1805).

[25] Fox H. W., Zisman W. A.: The spreading of liquids on low-energy surfaces. III. Hydrocarbon surfaces. Journal of Colloid Science, **7**, 428–442 (1952).

[26] Fowkes F. M.: Additivity of intermolecular forces at interfaces. I. Determination of the contribution to surface and interfacial tensions of dispersion forces in various liquids. The Journal of Physical Chemistry, **67**, 2538–2541 (1963).

[27] Owens D. K., Wendt R. C.: Estimation of the surface free energy of polymers. Journal of Applied Polymer Science, **13**, 1741–1747 (1969).

[28] Kaelble D. H.: Dispersion-polar surface tension properties of organic solids. The Journal of Adhesion, **2**, 66–81 (1970).

[29] Wu S.: Polymer interface and adhesion. CRC Press, Boca Raton (1973).

[30] Ko Y. C., Ratner B. D., Hoffman A. S.: Characterization of hydrophilic-hydrophobic polymeric surfaces by contact angle measurements. Journal of Colloid and Interface Science, **82**, 25–37 (1981).

[31] Lin J. W-P., Dudek L. P., Majumdar D.: Wetting properties of homopolymers and copolymers of pentafluorostyrene and methylacrylate and homopolymer blends. Journal of Applied Polymer Science, **33**, 657–667 (1987).

[32] El-shimi A., Goddard E. D.: Wettability of some low energy surfaces. I. Air/liquid/solid interface. Journal of Colloid and Interface Science, **48,** 242–248 (1974).

[33] Pyter R. A., Zografi G., Mukherjee P.: Wetting of solids by surface-active agents: The effects of unequal adsorption to vapor-liquid and solid-liquid interfaces. Journal of Colloid and Interface Science, **89**, 144–153 (1982).

[34] King R. N., Andrade J. D., Ma S. M., Gregnois D. E., Brostrom L. R.: Interfacial tensions at acrylic hydrogel-water interfaces. Journal of Colloid and Interface Science, **103**, 62–75 (1985).

[35] Dupré A.: Theorie mechanique de la chaleur. Gauthier-Villars, Paris (1869).

[36] Girifalco L. A., Good R. J.: A theory for the estimation of surface and interfacial energies. I. Derivation and application to interfacial tension. Journal of Physical Chemistry, **61**, 904–909 (1957).

[37] Jordan J., Jacob K. I., Tannenbaum R., Sharaf M. A., Jasiuk I.: Experimental trends in polymer nanocomposites-A review. Materials Science and Engineering, A, **393**, 1–11 (2005).

[38] Lavielle L., Schultz J.: Surface properties of graft polyethylene in contact with water: I. Orientation phenomena. Journal of Colloid and Interface Science, **106**, 438–445 (1985).

[39] Ruckenstein E., Lee S. H.: Estimation of the equilibrium surface free energy components of restructuring solid surfaces. Journal of Colloid and Interface Science, **120**, 153–161 (1987).